



UNIVERSITÀ DEGLI STUDI DI TRIESTE

DIPARTIMENTO DI FISICA

Corso di Laurea Magistrale in Fisica

MONITOR DI RADIAZIONE CON SENSORI AL DIAMANTE PER L'ESPERIMENTO BELLE II A SUPERKEKB

Laureando:
Giovanni Bassi

Relatore:
Prof. Lorenzo Vitale

Correlatori:
Prof. Livio Lanceri
Dott.ssa Chiara La Licata

ANNO ACCADEMICO 2017–2018



UNIVERSITÀ DEGLI STUDI DI TRIESTE

DIPARTIMENTO DI FISICA

Corso di Laurea Magistrale in Fisica

RADIATION MONITOR WITH DIAMOND SENSORS FOR THE BELLE II EXPERIMENT AT SUPERKEKB

Laureando:
Giovanni Bassi

Relatore:
Prof. Lorenzo Vitale

Correlatori:
Prof. Livio Lanceri
Dott.ssa Chiara La Licata

ANNO ACCADEMICO 2017–2018

Sommario

La tesi verte sullo sviluppo di un sistema di monitor di radiazione basato su rivelatori al diamante sintetico per l'esperimento di fisica delle particelle Belle II. Lo scopo principale è proteggere il rivelatore di vertice al silicio da dosi eccessive di radiazione, associate agli intensi fasci di elettroni e positroni che collidono al suo interno. Il lavoro si articola in due parti: una prima parte è dedicata alla caratterizzazione dei rivelatori in laboratorio tramite misure di rumore e irraggiamento con sorgenti radioattive, confrontate anche con una simulazione dedicata. La seconda parte, svolta presso i laboratori KEK in Giappone durante il commissioning dell'acceleratore e dell'esperimento, tratta l'installazione dei rivelatori in Belle II e l'analisi dei primi risultati da collisioni. La tesi dimostra che il sistema di monitoring è di fondamentale importanza per lo studio dei fondi macchina e per la loro riduzione.

Abstract

The thesis focuses on the development of a radiation monitor system based on synthetic diamond detectors for the Belle II particle-physics experiment. The system is intended to protect the silicon vertex detector from high radiation doses associated with the intense electron and positron beams that collide inside it. The work is organized into two parts: the first part is devoted to detector characterization with noise and irradiation measurements using radioactive sources and comparing the results with simulations. I conducted the second part at the KEK laboratories in Japan to install the detectors in Belle II and collect the first diamond data during the collision commissioning of the accelerator and detector. My work establishes that the radiation monitor system is essential for beam-background studies and background reduction.

Contents

Introduction	1
1 Flavor physics in the standard model	3
1.1 Status of particle physics	3
1.2 Overview of the standard model	4
1.3 Charge-parity violation and CKM matrix	6
1.4 Flavor physics at the inception of Belle II	8
2 Belle II experiment	10
2.1 Beauty factories	10
2.2 SuperKEKB accelerator	12
2.2.1 Nano-beam scheme	13
2.2.2 Interaction region	15
2.2.3 Damping ring and RF system	15
2.3 Belle II detector overview	16
2.4 Vertex detector	20
2.4.1 Pixel detector	20
2.4.2 Silicon vertex detector	21
2.4.3 Magnet	21
2.4.4 Radiation monitor system	22
2.5 Central drift chamber	22
2.6 Detectors for particle identification	23
2.6.1 Time of propagation	23
2.6.2 Aerogel ring-imaging Cherenkov counter	24
2.7 Electromagnetic calorimeter	25
2.8 K_L^0 and muon system	25
2.9 Trigger	25
3 Beam backgrounds and monitoring	27
3.1 Accelerator backgrounds	27
3.2 Radiation damage to silicon detectors	30
3.2.1 Radiation-induced defects	30
3.2.2 Effects on detector properties	31
3.3 Diamond sensors for radiation monitoring	32
3.3.1 Chemical vapor deposition	33
3.3.2 Detection of charged particles	33
3.3.3 Response to neutral particles	34

4	Characterization of diamond detectors	36
4.1	Assembly and first tests of diamond detectors	36
4.2	Calibration sources	39
4.3	Characterization with α source	40
4.3.1	Transient current technique	40
4.3.2	Simulation	41
4.3.3	Experimental setup	43
4.3.4	Data collection	44
4.3.5	Analysis of carrier mobilities	45
4.3.6	Analysis of charge-collection efficiency	48
4.4	Characterization with β source	51
4.4.1	Stability measurement	52
4.4.2	I-V characteristic	53
4.4.3	Calibration	55
4.4.3.1	Solid angle calculation	57
4.4.3.2	Generic simulation	58
4.4.3.3	Detailed simulation	61
4.4.3.4	Data fit and comparison with the simulation	62
4.4.3.5	Current dose-rate conversion	64
4.5	Characterization results	65
4.6	Cover mounting and final tests	65
5	Diamonds at work in SuperKEKB collision operations	66
5.1	Commissioning overview	66
5.2	Diamond system goals	67
5.3	Diamond setup and readout	68
5.3.1	Readout electronics	69
5.3.2	External circuit	71
5.4	Readout installation and test	73
5.5	Abort system test	74
5.6	First diamond signals	76
5.7	Diamond parameter adjustments	77
5.8	QCS quench protection	78
5.9	Analysis of first diamond data	78
5.9.1	Radiation doses	78
5.9.2	Abort examples	80
5.10	Background studies	81
5.10.1	Scraping background	85
5.11	Summary of collision commissioning	86
6	Summary	88
A	Environmental monitoring	91
A.1	Temperature and humidity systems	91
A.2	Interlock system and tests	92
B	Phase 3 diamond detector installation	93
	Bibliography	95

List of Figures

1.1	Scheme of SM particles (left panel) and interactions (right panel).	5
1.2	Unitarity triangle.	7
2.1	Hadronic production cross section for e^+e^- collisions at $\Upsilon(4S)$.	11
2.2	Scheme of the SuperKEKB accelerator facility.	13
2.3	Two-dimensional sketch of the nano-beam mechanism.	14
2.4	Sketch of the KEKB and SuperKEKB luminous region.	15
2.5	Schematic layout of the magnets and beam line near the interaction point.	16
2.6	Top view of Belle II experiment.	19
2.7	Schematic view of the PXD sensors.	20
2.8	Schematic view of a half of the SVD detector.	21
2.9	Diamond-detector geometry for the Belle II final setup.	22
2.10	Cosmic ray reconstruction in the CDC.	23
2.11	Representation of a TOP counter.	24
2.12	Scheme of the ARICH detector.	24
3.1	Leading-order Feynman diagrams for the radiative Bhabha process.	29
3.2	Leading-order Feynman diagram for the two-photon process.	29
3.3	Schematic layout of a diamond sensor.	34
4.1	Picture of an uncovered diamond sensor.	36
4.2	Current-voltage characteristic of a coaxial cable insulator.	37
4.3	Diamond sensor current-voltage characteristics with both polarizations.	38
4.4	Electron energy spectrum for the ^{90}Sr β -decay.	39
4.5	Representation of the sensor contact layers.	41
4.6	Results of the simulation with α -particles.	42
4.7	Experimental setup for detector characterization with the α source.	43
4.9	α -particle induced signal at +300 V and -300 V.	44
4.10	Time evolution of the charge-carriers signal as a function of biasing polarity.	45
4.11	Example of a signal spikes during transition edges.	46
4.12	Electron and hole mobilities as functions of the electric.	46
4.13	Electron and hole drift velocities as functions of the electric field.	47
4.14	Hole and electron collected charges as a function of the electric field.	48
4.15	Collected charge as a function of the inverse drift velocity.	49
4.16	Experimental setup for detector characterization with the the β source.	51
4.17	Current time evolution for the DC24 diamond with different polarizations.	52
4.18	Current as a function of time and magnification with fit overlaid.	53
4.19	DC26 IV characteristic.	54
4.20	DC24 IV characteristic.	54

LIST OF FIGURES

4.21	Sketch of the assumption associated with the calibration measurement.	56
4.22	Current as a function of the source-detector distance.	56
4.23	Sketch of the geometrical layout.	57
4.24	Comparison between the two fit functions used for the detector calibrations.	59
4.25	Comparison between the centered and shifted source simulations.	60
4.26	Comparison between point-like and physical source simulations.	60
4.27	Sketch of the experimental setup implemented for the simulation.	61
4.28	Simulated current as a function of detector-source distance.	61
4.29	DC24 calibration data with fit results with functions 4.13 and 4.15 overlaid.	62
4.30	Comparison between data and simulation for the calibration measurements.	63
5.1	Scheme of the SuperKEKB beam-abort system.	68
5.2	Drawing of the diamond detector (in green) positioning on the beam pipe.	69
5.3	Belle II reference system.	69
5.4	Block diagram representing the main DCU functional components.	69
5.5	Block diagram representing the DCU data stream.	70
5.6	Scheme of the external circuit main components in the NIM crate.	72
5.7	Diamond control units used during Phase 2.	73
5.8	BWD channel 2 noise distribution.	73
5.9	FWD dose rates as functions of time during the abort test.	74
5.10	Moving sums of radiation doses measured during the abort test.	75
5.11	First diamond signal during beam injection.	76
5.12	Current range change before a background study.	77
5.13	Correlation of beam currents and diamond dose rates as functions of time.	79
5.14	Correlation between LER beam current and diamond dose rates.	79
5.15	Doses integrated by BWD diamonds between 15 May and 8 July.	80
5.16	Moving sums of radiation doses measured during aborts.	81
5.17	Correlation between diamond responses and accelerator parameter.	82
5.18	Beam-size study with different bunch-filling configurations.	83
5.19	Beam-lifetime evolution during a beam-size study.	84
5.20	Pressure profile near the interaction region.	85
5.21	Beam-size study with different beam currents.	85
5.22	Time evolution of doses and accelerator parameters during a background test.	86
B.1	Picture of SVD supports with diamond detectors mounted.	93
B.2	Picture of a diamond detector mounted on the beam pipe.	94

List of Tables

1.1	Summary of the three forces described by the SM.	4
2.1	Cross sections of the main final states produced in $\Upsilon(4S)$ e^+e^- collisions. . .	12
2.2	Comparison between KEKB and SuperKEKB main parameters.	14
2.3	Summary of the Belle II components and specifications.	18
2.4	Cross sections and trigger rates with $\mathcal{L} = 8 \cdot 10^{35} \text{ cm}^{-2}\text{s}^{-1}$ at $\Upsilon(4S)$	26
3.1	Comparison between diamond and silicon main properties at T=300K.	32
4.1	Energies and branching ratios of the $^{241}_{95}\text{Am}$ α -spectrum.	39
4.2	Measured zero-field mobility μ_0 and saturation drift velocity v_{sat}	47
4.3	Average zero-field mobility μ_0 and saturation drift velocity v_{sat}	48
4.4	Estimated electron-hole creation energies for the analyzed sensors.	50
4.5	Fit results of the current transient a during stability measurement.	53
4.6	Sensor gains obtained by comparing calibration data and the simulation.	64
5.1	Summary of the three commissioning phases of SuperKEKB and Belle II.	66
5.2	Summary of the beam abort configurations.	68
5.3	Summary of the ranges and sensitivities for various DCU configurations.	71
5.4	Abort settings related to the radiation doses displayed in Fig. 5.16.	80
5.5	Results of the linear fit in Fig. 5.18.	83

Introduction

In this experimental particle-physics thesis, I worked on the characterization, calibration, installation, and commissioning of artificial diamond detectors for radiation protection of the Belle II silicon vertex detector.

The description of particles and fundamental interactions provided by the standard model of particle physics (SM) has successfully passed all the experimental tests to date. However, the standard model is known to be an incomplete effective theory: for instance, descriptions of gravity, dark matter, or dark energy are lacking.

The quest for extensions of the standard model is the key goal of today's particle physics. At the LHC, putative particles that can extend the standard model are directly searched for by colliding proton beams at $O(10)$ TeV energies.

Such direct approach is limited by the available collision energy. Since direct LHC searches yielded null results so far, and more powerful accelerators are not foreseen in the near future, indirect searches at the precision frontier offer among the best opportunities for extending the standard model in the next decade.

Such approach relies on comparing precise measurements with similarly precise SM predictions to reveal discrepancies, possibly indicative of non-SM dynamics. A large portion of this program focuses on B and D meson, and τ lepton, dynamics, because the multitude of involved processes offers a rich phenomenology, allowing powerful, redundant tests of a broad class of SM extensions.

The Belle II experiment at the SuperKEKB accelerator is one of the leading facilities for precision indirect searches. The SuperKEKB accelerator is a next-generation high-luminosity asymmetric e^+e^- collider that will produce billions of B and D mesons, and τ leptons over the course the next decade. The heart of Belle II is the silicon vertex detector, which finely samples the trajectories of charged particles. This is essential for a successful program, since charged particles are the most common final states in B , D , and τ decays.

High beam intensities are needed to maximize particle-production rates and therefore reach high precision. However, high intensities generate high radiation backgrounds in which the detector has to operate. As the detector accumulates radiation doses, its performances degrade, jeopardizing the successful completion of the scientific program.

In order to protect the Belle II silicon detector from high radiation doses, we designed a system based on single-crystal artificial-diamond detectors. The system is intended to monitor the radiation doses near the interaction region, triggering protective actions when needed.

I investigated the properties of 1/4 of the diamond detectors of our system determining their optimal operating conditions. I contributed to each step of the detector construction, starting from the diamond crystal to the complete integration of the system into Belle II. I performed the full detector characterization, measuring its response to irradiation and comparing the outcomes with dedicated simulations. As the Belle II and SuperKEKB

collision commissioning started, I calibrated and operated the radiation monitoring system on site at KEK. After testing the entire system, I contributed to several background studies, completing the first analysis of diamond data.

This thesis is organized as follows. Chapter 1 offers an overview of flavor dynamics in the standard model and how Belle II will investigate it. Chapter 2 presents the main Belle II characteristics and performances, with emphasis on the vertexing detectors and radiation-monitoring system that protects them. Chapter 3 introduces the main sources of beam-induced backgrounds, the associated radiation damage of silicon detectors, and the motivation for the choice of diamond sensors. Chapter 4 shows all the procedures I performed to achieve working and fully characterized diamond detectors. Chapter 5 presents the results I obtained during the Belle II commissioning period at KEK.

Chapter 1

Flavor physics in the standard model

This chapter presents an overview of the flavor physics in the standard model, highlighting the key experimental probes in searching for non SM physics and how Belle II will investigate them.

1.1 Status of particle physics

The standard model of particle physics is a quantum field theory that describes three of the four known fundamental interactions between particles. The theoretical formulation is grounded onto three main concepts: gauge symmetry, a representation of particles and interactions under that symmetry, and the presence of a mechanism for spontaneously breaking the symmetry. Particle interactions are represented within a Lagrangian formalism.

The standard model was completed in the seventies, and it has been tested with high precision since, establishing itself as a great success of the reductionist paradigm in describing natural phenomena [1]. However, observations and theoretical aspects at the subatomic and cosmological scales suggest that the standard model is incomplete. Examples include the differences between fermion masses (*hierarchy problem*), the lack of an explanation for dynamically generated asymmetry between matter and antimatter observed in the universe (*baryon asymmetry*), as well as phenomena like *dark matter* and *dark energy*, introduced to explain cosmological observations.

A deeper comprehension of these and other questions may come from the extension of the theory at higher energy scales. The quest for extensions of the standard model is the key goal of today's particle physics. Present research aims at revealing phenomena that can support such extensions with two complementary approaches. The energy-frontier approach relies on revealing directly, typically in high-energy collisions, new particles or interactions not included in the SM. By increasing the energy available in the center of mass, collisions may be energetic enough to produce new heavy particles. This approach is constrained by the maximum collision energy. Intensity-frontier research looks for deviations between precise experimental results and equally precise theoretical predictions that may reveal non-SM dynamics. The key is measuring with high precision potentially small contributions from unknown particles to known processes. Intensity research is centered on the quark weak-interaction sector because the multitude of involved processes offers a rich phenomenology, allowing powerful redundancy tests of a broad class of SM extensions. One of the leading experiments that pursues this goal is Belle II at KEK laboratories in Japan.

1.2 Overview of the standard model

In the standard model, matter particles are represented as excitations of spin- $\frac{1}{2}$ fields while interactions are mediated by spin-1 gauge bosons. Particles and part of the gauge bosons acquire their mass via the interaction with a spin-0 field called Higgs field, mediated by the Higgs boson. There are three interactions described by the theory,

- the strong interaction, which is mediated by massless bosons called gluons (g) and, as described in quantum chromodynamics (QCD), is characterized by a charge named *color* that exists in three different kinds; gluons themselves carry color charge with eight different color states;
- the electromagnetic interaction, which is mediated by massless bosons called photons (γ); the electromagnetic charge exists in only one kind and photons do not carry it;
- the weak interaction, which is mediated by three massive bosons, namely W^\pm and Z^0 ; their masses are of the order of 100 GeV and two of them are electrically charged.

The main characteristics of the three forces described by the SM are summarized in Table 1.1.

Interaction	Charge	Strength	Range	Gauge bosons
Strong	Color charge	1	10^{-15} m	Gluons
Electromagnetic	Electric charge	1/137	∞	Photon
Weak	Weak charge	10^{-6}	10^{-18} m	$W^\pm Z^0$

Table 1.1: Summary of the three forces described by the SM. The strength is obtained comparing the forces at the proton mass scale.

The standard model is a gauge theory with symmetry group

$$SU(3)_C \otimes SU(2)_L \otimes U(1)_Y .$$

$SU(3)_C$ is the group of QCD, where C stands for color; the product $SU(2)_L \otimes U(1)_Y$ describes the electroweak interaction, where L is for left and Y for hypercharge; $SU(2)_L$ has three generators, named $W_{1,2,3}$. The generator for $U(1)_Y$ is called B . The physical particles W^\pm , Z^0 and γ are linear combinations of the generators $W_{1,2,3}$ and B ,

$$W^\pm = \frac{1}{\sqrt{2}}(W_1 \mp iW_2) ,$$

$$\begin{pmatrix} \gamma \\ Z^0 \end{pmatrix} = \begin{pmatrix} \cos(\theta_W) & \sin(\theta_W) \\ -\sin(\theta_W) & \cos(\theta_W) \end{pmatrix} \begin{pmatrix} B \\ W_3 \end{pmatrix} ,$$

where θ_W is known as weak angle.

Generator mixing is caused by the spontaneous symmetry breaking. Such mechanism is related to the Higgs field, which has a non vanishing vacuum expectation value. The symmetry of $SU(2)_L \otimes U(1)_Y$ is broken. Only the electromagnetic symmetry group $U(1)_{EM}$ is unaffected by the mechanism. The weak bosons acquire masses via the spontaneous symmetry breaking while the photon remain massless. An explicit mass term, quadratic in the fields, cannot be added directly to the SM Lagrangian as it would break gauge symmetry.

The Higgs mechanism generates particle masses. The coupling between fermion fields and the Higgs field is expressed by the so-called "Yukawa term" of the Lagrangian. Fermion masses are free parameters of the model. The W boson mass M_W is a function of the Z boson mass M_Z through the cosine of the weak angle.

Fermions are divided in two categories, quarks and leptons, each organized in three families of doublets:

- Quarks couple to all interactions. Each family doublet comprises an up-type quark with electric charge $2e/3$ and a down-type quark with electric charge $e/3$. The three doublets are

$$\begin{pmatrix} u \\ d \end{pmatrix} \begin{pmatrix} c \\ s \end{pmatrix} \begin{pmatrix} t \\ b \end{pmatrix}.$$

Each quark possesses a quantum number called *flavor*. Flavor is conserved in the strong and electromagnetic interactions but not in weak transitions. Each quark has a corresponding antiparticle called *anti-quark*. The color confinement principle [2] of QCD prevents quark from being observed individually. Observable states include bound states of a quark and an anti-quark, called *mesons* and states composed of three quarks, called *baryons*. Quark masses [3] range from the mass of the up quark $m_u \simeq 2.3 \text{ MeV}/c^2$ to the mass of the top quark $m_t \simeq 173 \text{ GeV}/c^2$.

- Leptons couple only to the electroweak interaction. Each family comprises a massive and negatively charged lepton and a massless and neutral neutrino. The three doublets are

$$\begin{pmatrix} e \\ \nu_e \end{pmatrix} \begin{pmatrix} \mu \\ \nu_\mu \end{pmatrix} \begin{pmatrix} \tau \\ \nu_\tau \end{pmatrix}.$$

Each lepton has a quantum number called *lepton family number*. The sum of all these quantum numbers in a lepton system, the total lepton number, is conserved in the SM. Similarly to quarks, each lepton have its antiparticle. Lepton masses range from the electron mass $m_e \simeq 0.5 \text{ MeV}/c^2$ to the tau-lepton mass $m_\tau \simeq 1.8 \text{ GeV}/c^2$.

Figure 1.1 shows a summary of the particles and interactions described by the standard model.

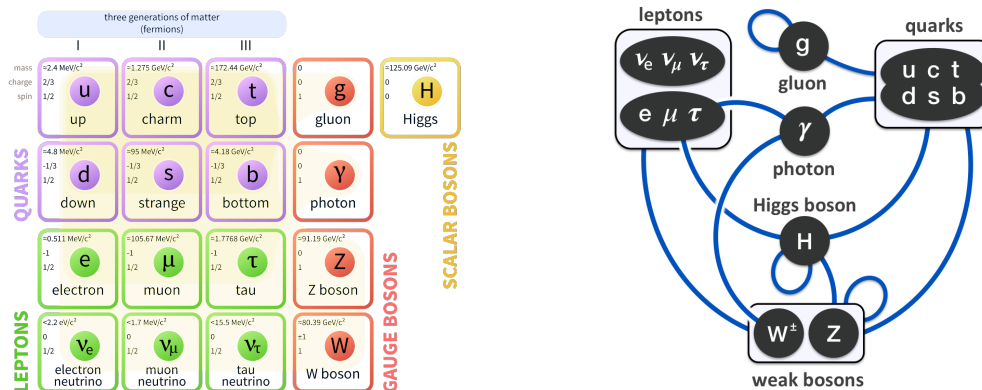


Figure 1.1: Scheme of SM particles (left panel) and interactions (right panel).

1.3 Charge-parity violation and CKM matrix

Gauge symmetry [4] is one of the chief concepts subtending the SM structure. In addition to this continuous symmetry, discrete symmetries are also relevant in determining the SM phenomenology.

Parity (\mathcal{P}) reverses the spatial coordinates, charge conjugation (\mathcal{C}) inverts all the internal quantum numbers of a particle transforming it into its antiparticle, and time reversal (\mathcal{T}) inverts the direction of time. While the combination of these three symmetries is conserved in the SM they are not conserved singularly. In addition, the combined \mathcal{CP} symmetry is broken by the weak interaction [5–7].

\mathcal{CP} violation was first observed in 1964 [8] and then introduced in the SM by Kobayashi and Maskawa (KM) in 1972 [9]. They extended an idea of Cabibbo [10], who solved the issue of seemingly different weak couplings measured in different processes. Cabibbo hypothesized a mass eigenstate (d) for down-like quarks, which differs from the weak eigenstate (d') as seen by W^\pm bosons. Kobayashi and Maskawa generalized the Cabibbo matrix from a four-quark to a six-quark model to explain the observation of \mathcal{CP} violation. \mathcal{CP} violation might be a key ingredient to explain phenomena also at the cosmological such as the dynamical origin for the baryon asymmetry currently observed in the universe.

The complex, unitary mixing matrix that "rotates" mass eigenstates into weak eigenstates is known as *Cabibbo-Kobayashi-Maskawa* matrix or V_{CKM} .

By assuming N generations of quarks, V_{CKM} has $(N - 1)^2$ parameters [11]. If $N = 2$ there is only one parameter that is called *Cabibbo angle* θ_C . With three generations, the free parameters are four; three Euler angles, θ_{12} , θ_{23} , and θ_{13} and a complex phase δ . This phase allows for the presence of \mathcal{CP} violation. In matrix format we have

$$\begin{pmatrix} d' \\ s' \\ b' \end{pmatrix} = \begin{pmatrix} V_{ud} & V_{us} & V_{ub} \\ V_{cd} & V_{cs} & V_{cb} \\ V_{td} & V_{ts} & V_{tb} \end{pmatrix} \begin{pmatrix} d \\ s \\ b \end{pmatrix} .$$

The i' index represents the interaction state for the i -quark while the i index stays for the mass state. The V_{ij} matrix elements represent the coupling between a i -quark (up-like quark) and j -quark (down-like quark).

It is convenient to use the *Wolfenstein* parametrization, which is an expansion in the small parameter λ (the sine of the Cabibbo angle $\sin(\theta_C) \simeq 0.23$) and renders evident the observed hierarchy between CKM elements

$$V_{CKM} = \begin{pmatrix} 1 - \lambda^2/2 & \lambda & A\lambda^3(\rho - i\eta) \\ -\lambda & 1 - \lambda^2/2 & A\lambda^2 \\ A\lambda^3(1 - \rho - i\eta) & -A\lambda^2 & 1 \end{pmatrix} + \mathcal{O}(\lambda^4) ,$$

where

$$\lambda = \frac{V_{us}}{\sqrt{V_{ud}^2 + V_{us}^2}} \quad A\lambda^2 = \lambda \frac{V_{cb}}{V_{us}} \quad A\lambda^3(\rho + i\eta) = V_{ub}^* .$$

The parameter λ represents the mixing of quarks between different quark generations; η is the complex phase representing \mathcal{CP} violation, and A and ρ are real parameters.

Within the Kobayashi and Maskawa scheme, the conditions needed to introduce \mathcal{CP} violation are the following:

- there must exist at least three generations of quarks;

- there must be a coupling between all the families;
- the quarks must have different masses to avoid phase-canceling rotations.

All conditions have been proved experimentally. A graphical representation of the V_{CKM} matrix, known as Unitarity Triangles, is also useful.

This relies on the unitary condition $V_{CKM}V_{CKM}^\dagger = \mathbb{1}$, which imposes nine unitarity relations,

$$\begin{aligned} |V_{ud}|^2 + |V_{cd}|^2 + |V_{td}|^2 = 1 & \quad V_{us}^*V_{ud} + V_{cs}^*V_{cd} + V_{ts}^*V_{td} = 0 & \quad V_{ud}V_{cd}^* + V_{us}V_{cs}^* + V_{ub}V_{cb}^* = 0, \\ |V_{us}|^2 + |V_{cs}|^2 + |V_{ts}|^2 = 1 & \quad V_{ub}^*V_{ud} + V_{cb}^*V_{cd} + V_{tb}^*V_{td} = 0 & \quad V_{ud}V_{td}^* + V_{us}V_{ts}^* + V_{ub}V_{tb}^* = 0, \\ |V_{ub}|^2 + |V_{cb}|^2 + |V_{tb}|^2 = 1 & \quad V_{ub}^*V_{us} + V_{cb}^*V_{cs} + V_{tb}^*V_{ts} = 0 & \quad V_{cd}V_{td}^* + V_{cs}V_{ts}^* + V_{cb}V_{tb}^* = 0. \end{aligned}$$

The relations in the middle and right columns can be interpreted as triangles in the complex plane. A \mathcal{CP} conserving theory would have brought to one-dimensional (squashed) triangles. Among the six triangles, the ones between lines/columns one and three have side

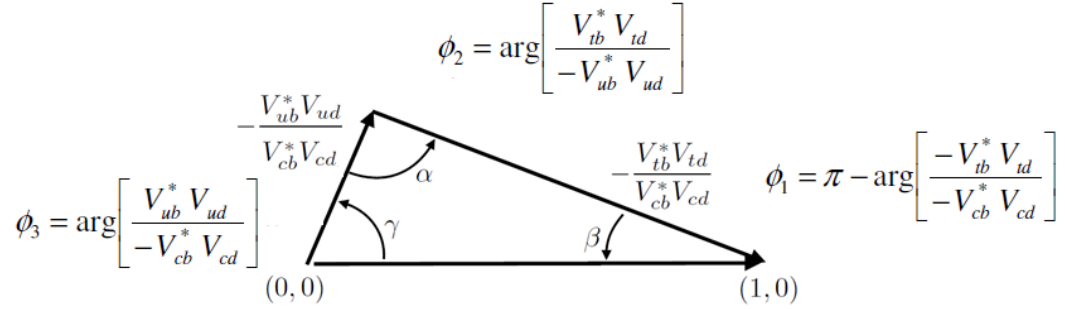


Figure 1.2: Unitarity triangle.

sizes of similar length. Usually we refer to as "Unitarity Triangle" the triangle corresponding to the central equation above. Figure 1.2 shows the Unitarity Triangle: the sides are normalized to the length of the base and the angles are expressed according to common conventions, α or ϕ_2 , β or ϕ_1 , and γ or ϕ_3 .

Since \mathcal{CP} violation is associated to a complex phase, it needs interference to be observed. Hence two or more amplitudes (a_1 and a_2) that carry different weak (ϕ_i) and strong (δ_i) phases need to contribute to an observable process.

Weak phases come from complex parameters in the Lagrangian that contribute to the total amplitude A describing the process ($A = |A_i|e^{i\sum_i\phi_i}$). Since they arise only in the coupling with the W^\pm bosons, they are called weak. Strong phases come from intermediate on-shell states. They may come from either time evolution or complicated strong-interaction rescattering [12].

By considering decay phenomena and particle-antiparticle oscillations, which occur among neutral flavored mesons whose mass and flavor eigenstate do not coincide, three classes of \mathcal{CP} violating phenomenologies exist,

- \mathcal{CP} violation in decay (direct \mathcal{CP} violation) occurs if decay rates for a process and its \mathcal{CP} conjugate differ, ($\Gamma(X \rightarrow f) \neq \Gamma(\bar{X} \rightarrow \bar{f})$), where X is a hadron containing the flavored quark and \bar{X} is the corresponding antihadron. The observable used typically is the partial-width asymmetry

$$\mathcal{A}_f = \frac{\Gamma(X \rightarrow f) - \Gamma(\bar{X} \rightarrow \bar{f})}{\Gamma(X \rightarrow f) + \Gamma(\bar{X} \rightarrow \bar{f})}. \quad (1.1)$$

\mathcal{CP} violation in decay occurs in neutral and charged mesons, and baryons, because it is independent of flavor mixing;

- \mathcal{CP} violation in mixing (indirect \mathcal{CP} violation) occurs if probabilities of neutral meson mixing from a state to its \mathcal{CP} conjugate and viceversa differ, ($P(X^0 \rightarrow \bar{X}^0) \neq P(\bar{X}^0 \rightarrow X^0)$). The observable used is typically

$$\mathcal{A}_{SL} = \frac{d\Gamma(X^0(t) \rightarrow \bar{f})/dt - d\Gamma(\bar{X}^0(t) \rightarrow f)/dt}{d\Gamma(X(t) \rightarrow \bar{f})/dt + d\Gamma(\bar{X}^0(t) \rightarrow f)/dt}. \quad (1.2)$$

Experimentally one selects a final state \bar{f} in which particle X^0 cannot decay directly, while its antiparticle does;

- \mathcal{CP} violation in interference between a direct decay and a decay following mixing occurs when both particle and antiparticle can decay into the same state. Hence, the final state can be reached both via direct decay or via intermediate mixing to the antiparticle that subsequently decays. This type of \mathcal{CP} violation is possible even if, individually, \mathcal{CP} is conserved in decay and mixing. The observable that is usually measured is

$$\mathcal{A}_{f_{CP}} = \frac{d\Gamma(X^0(t) \rightarrow f_{CP})/dt - d\Gamma(\bar{X}^0(t) \rightarrow f_{CP})/dt}{d\Gamma(X^0(t) \rightarrow f_{CP})/dt + d\Gamma(\bar{X}^0(t) \rightarrow f_{CP})/dt}. \quad (1.3)$$

1.4 Flavor physics at the inception of Belle II

Nowadays flavor physics is seen as one of the most promising opportunities to seek the first indirect signs of non-SM dynamics. The great variety of quarks interactions allows for several tests of a reduced set of observables through different physics processes. Redundancy is key to achieve a complete understanding of the dynamical picture, allowing for robust comparison between experimental results and SM predictions in search for discrepancies [13].

The two main probes in searching for non SM physics using flavor dynamics are flavor-changing-neutral-currents and \mathcal{CP} -violating processes.

- *Flavor changing neutral currents (FCNC)* are quark transitions that change quark flavor but not charge. FCNC are suppressed within the SM, which allows them only within loop processes. This makes FCNC amplitudes both suppressed, which enhances the possible contributions from non-SM processes, and sensitive to a broad class of SM extensions. Non-SM massive particles could in fact alter FCNC amplitudes, possibly causing a discrepancy between predictions and measurements [14].

Examples of recently relevant FCNC decays include the semileptonic $b \rightarrow sll$ transition, in which a bottom quark within a B meson decays into a strange quark and two leptons. The branching fraction is measured as a function of the squared four-momentum transferred to the two leptons and then compared to theoretical predictions. In order to sharpen the discriminating power, the ratio R_K between branching fractions such as $R_K = \mathcal{B}(B^+ \rightarrow K^+ \mu^+ \mu^-) / \mathcal{B}(B^+ \rightarrow K^+ e^+ e^-)$ is typically used. This ratio is precisely predicted and expected to be unity in the SM, given the universal coupling of electrons and muons. These decays recently attracted attention because a 2.6σ discrepancy from the prediction was recently observed [15].

- \mathcal{CP} violation measurements allow for probing the consistency of phase measurements with the predictions [16]. In fact, many non-SM physics models may introduce unobservable modifications to the rates of suppressed processes but large biases in their \mathcal{CP} -violating phases. Hence, \mathcal{CP} violation measurements offer a complementary window on non-SM dynamics with respect to FCNC measurements.

The two main experiments that will investigate quark-flavor physics in the next decade are Belle II and LHCb.

LHCb is a forward spectrometer that operates at the Large Hadron Collider. It studies proton-proton collisions at $O(10)$ TeV with 10^3 to 10^4 higher $b\bar{b}$ and $c\bar{c}$ rates than Belle II. The production rate advantage over Belle II allows for low-statistical-uncertainty measurements. High-energy collisions, in addition, allow to investigate a larger variety of processes than at Belle II, including the production of all kinds of b -hadrons. The main LHCb challenge is to achieve an efficient online selection of interesting processes, starting from $10^2 \div 10^3$ particles per event, without knowing the exact interaction energy of composite-particle collisions. Strict requirements on kinematical and dynamical quantities are applied to decouple background from interesting processes, partially reducing the high production-rate advantage over Belle II and biasing in a hard-to-simulate way some key distributions used in offline analysis.

Belle II e^+e^- collisions produce a low-background environment that, along with the more stringent cinematic constraints on the initial states due to the point-like nature of the colliding particles, lead to a more efficient particle reconstruction. The lower-background environment along with better spatial resolution of neutral particle detectors allow Belle II to overcome LHCb on measurements involving flavor tagging [17, 18] or more than one neutral particle.

Belle II will investigate a plethora of observables to test for non-SM physics. The main topics where Belle II is anticipated to offer unique, or very competitive, insight are the following [19]:

- Improved determination of the unitarity angle α , which is currently among the least well determined CKM parameters with an uncertainty of roughly seven degrees. The combination of $B \rightarrow \pi\pi$ and $B \rightarrow \rho\rho$ decays offer the most precise way to determine the α angle and involve many final states with neutral particles.
- Improved determination of the unitarity angle γ , which is one of the few measurements of the unitarity triangle that can be improved significantly by only experimental enhancements. The combination of $B \rightarrow DK$ and $B \rightarrow D\pi$ decays and the need for a complicated Dalitz-plot analysis will benefit from the low-background Belle II environment.
- Measurements of FCNC decays involving either neutrinos, photons, or π^0 in the final states.
- Measurements involving τ lepton decays.

Chapter 2

Belle II experiment

This chapter outlines the main features of the Belle II experiment at the SuperKEKB accelerator, where I conducted my thesis work.

2.1 Beauty factories

Beauty factories (b factories, in short) are high-energy particle-physics experiments designed to produce large numbers of B mesons with low background. Their center-of-mass energy is tuned to the $\Upsilon(4S)$ resonance, which is just above the threshold to decay into a $B\bar{B}$ pair.

In the 1980's the idea of testing the KM model of \mathcal{CP} violation by studying neutral B mesons was proposed. However, the small values of the relevant branching fractions [20] and technological challenges in achieving the required high luminosities prevented realistic experiment designs until the 1990's.

At that time, a number of phenomenological, experimental, and technological conditions were met, which allowed the realization of B factory experiments [21, 22]:

- The observation of a long B meson lifetime from experiments at SLAC, and the discovery of a substantial rate for $B^0 - \bar{B}^0$ mixing by the ARGUS experiment at DESY, indicated that the CKM-matrix parameters are in the range that makes accessible to the test the KM idea using B decays.
- The phenomenological demonstration that a measurement of \mathcal{CP} violation in neutral B meson decays to \mathcal{CP} eigenstates could be unambiguously interpreted without theoretical uncertainties, provided that large B meson data samples could be collected [23].
- Improvements in performance of e^+e^- storage rings, that allowed increasing production rates from 30 to one million meson pairs a day in roughly 30 years.
- The development of silicon tracking detectors with $O(10)$ μm spatial resolutions, which allowed to resolve $O(100)$ μm decay distances, typical of the relevant decay lengths.
- The introduction of the "asymmetric-energy" collider concept, discussed in more detail below.
- The measurement of a non zero value for $|V_{ub}|$ performed by CLEO in 1990, which proved a coupling between the first and the third family thus enabling \mathcal{CP} violation in b quark dynamics.

In B factories e^+ and e^- beams are brought to collision. The production of B -meson pairs occurs via the $e^+e^- \rightarrow \Upsilon(4S) \rightarrow B\bar{B}$ process at the $\Upsilon(4S)$ resonance energy. The $\Upsilon(4S)$ decays into $B\bar{B}$ states with a branching ratio greater than 96%, almost equally distributed into charged and neutral B -meson pairs. Figure 2.1 shows the hadronic production cross section

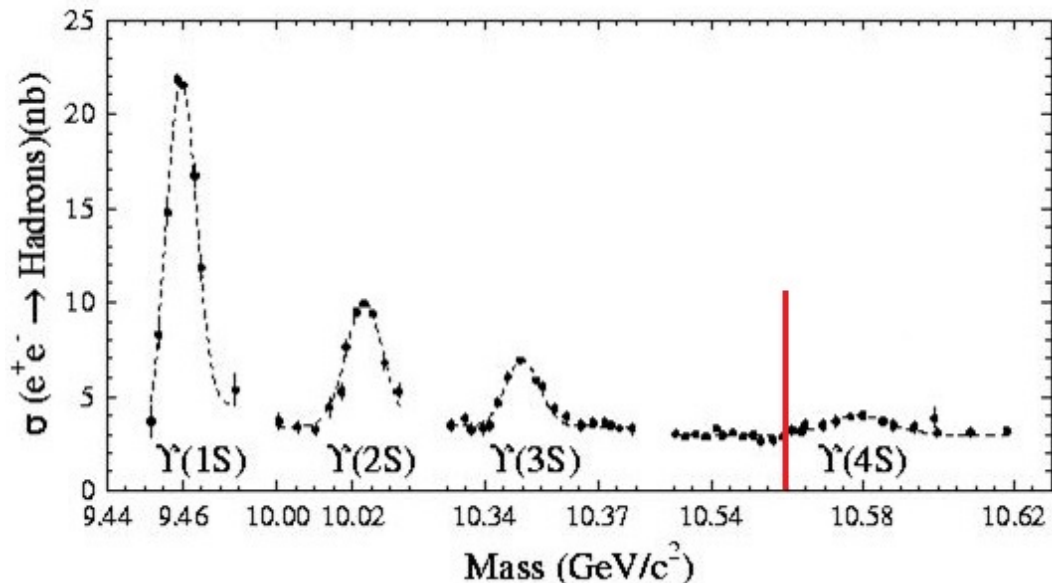


Figure 2.1: Hadronic production cross section for e^+e^- collisions as a function of final-state mass. $\Upsilon(b\bar{b})$ resonances are visible. The red line indicates the mass threshold for $B\bar{B}$ production.

section from e^+e^- collisions as a function of final-state mass. The enhancements represent the Υ resonances, made of $b\bar{b}$ quarks.

After the $\Upsilon(4S)$ decay, the two B mesons evolve coherently, preserving the flavor anti-correlation. As the $\Upsilon(4S)$ is a $J^{PC} = 1^{--}$ state, $B\bar{B}$ pairs are produced in the $L=1$ state. Independent oscillation of the B mesons, would lead to a state made up of two identical mesons. However, since the $L=1$ state is antisymmetric and identical bosons can only exist in symmetric configurations, the system has to preserve the flavor anti-correlation. \mathcal{CP} violation measurements are mainly based on determining asymmetries of partial decay rates into common final states as functions of delay time.

Assuming that at time $t = t_1$ one of the two B decays in a flavor eigenstate, for example via the semileptonic process $B^0 \rightarrow D^- l^+ \nu_l$ where l indicates a lepton, at the same time t_1 the other meson must be into the opposite flavor eigenstate. Then it evolves until $t = t_2$, when also the second B meson decays, for example via the process $B^0 \rightarrow J/\Psi K_S^0$. The measurement consists in determining the decay rate of mesons of known flavor at t_1 into \mathcal{CP} eigenstate as function of $t = t_2 - t_1$. Three main quantities are measured [24, 25]:

- the flavor at the time t_1 . This is done by inferring the flavor of the other meson at its decay by restricting the sample to flavor-specific decays;
- the common decay mode in which the signal meson decays. This is done through exclusive B -meson reconstruction;
- the time between the two decays, which is inferred by the determination of the signal meson decay-length and momentum.

As shown in Fig. 2.1, the difference in mass between the $\Upsilon(4S)$ resonance and the $B\bar{B}$ system is $\Delta m = (10580 - 2 \times 5280) \text{ MeV} = 20 \text{ MeV}$. Consequently B mesons are almost at rest in the $\Upsilon(4S)$ reference frame, making the time measurement practically impossible if the $\Upsilon(4S)$ is at rest. Boosting the $\Upsilon(4S)$ by using energy-asymmetric beams allows instead for measuring the time difference, which becomes sufficiently larger than the spacial resolutions. The SuperKEKB boost is $\beta\gamma = (E_{e^-} - E_{e^+}) / (2\sqrt{E_{e^-}E_{e^+}}) = 0.28$.

B-factories require

- High luminosity, since a large $B\bar{B}$ yield must be produced to have sufficiently large decay samples, given the branching ratios.
- Boosted $B\bar{B}$ pairs, so that they travel enough in the detector for the delay time to be measured.
- Low-material inner detectors, since particles have low momenta, and the material of the detector produces multiple scattering.

Various final states are produced in e^+e^- colliders at the $\Upsilon(4S)$ mass (Table 2.1).

Process	Cross section (nb)
$\Upsilon(4S)$	1.05
$u\bar{u}(\gamma)$	1.61
$d\bar{d}(\gamma)$	0.40
$s\bar{s}(\gamma)$	0.38
$c\bar{c}(\gamma)$	1.30
$e^+e^-(\gamma)$	300
$\gamma\gamma(\gamma)$	4.99
$\mu^+\mu^-(\gamma)$	1.148
$\tau^+\tau^-(\gamma)$	0.919
$\nu\bar{\nu}(\gamma)$	0.25×10^{-3}

Table 2.1: Cross sections of the main final states produced in e^+e^- collisions at the $\Upsilon(4S)$ center-of-mass energy [26].

2.2 SuperKEKB accelerator

SuperKEKB is an asymmetry-energy collider [27]. Two beams circulate in separate rings: a 7 GeV electron beam (high energy ring, HER) and a 4 GeV positron beam (low energy ring, LER). The center of mass energy is

$$E_{CM} = \sqrt{s} = [(E_{e^-} + E_{e^+})^2 - (\mathbf{p}_{e^-} + \mathbf{p}_{e^+})^2]^{\frac{1}{2}} \simeq (4E_{e^-}E_{e^+})^{\frac{1}{2}} = 10.58 \text{ GeV} , \quad (2.1)$$

where E_{e^\pm} and \mathbf{p}_{e^\pm} are the energies and momenta of positrons (+) and electrons (-) and the electron mass is neglected.

The SuperKEKB accelerator is an upgrade of the previous KEKB accelerator. It was built in the same enclosures used for its predecessor and partly reuses its magnets. Figure 2.2 shows a schematic representation of SuperKEKB.

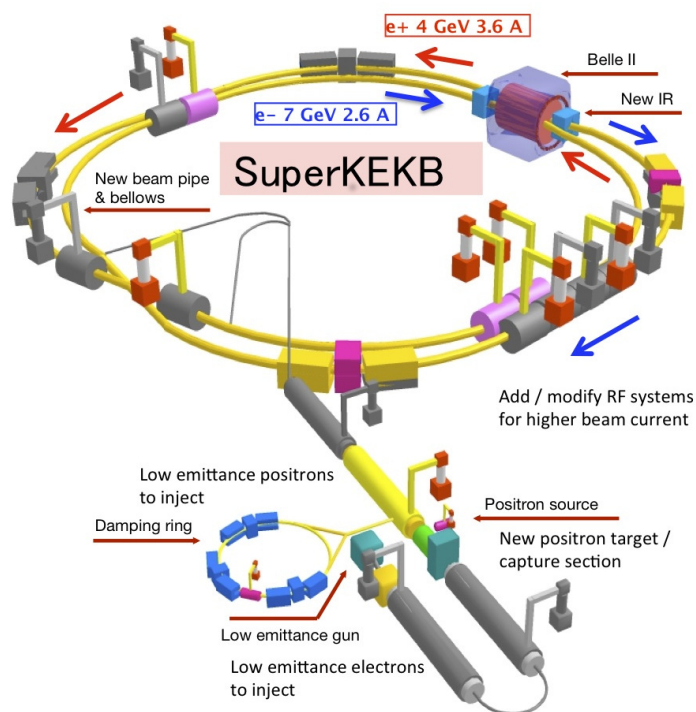


Figure 2.2: Scheme of the SuperKEKB accelerator facility.

The electrons are produced via photoelectric effect in a pre-injector by a pulsed laser directed on a cold cathode target. They are accelerated by a linear accelerator (Linac) to 7 GeV and injected in the HER. The positrons are produced by colliding electrons on tungsten. They are injected in a damping ring to reduce their spread in the position and momentum (emittance), then accelerated to 4 GeV in the Linac and injected in the LER.

The number of physics events N produced in a time t , given the cross section (σ) of a specific process, is related to the luminosity L by $N = \int_0^t L \sigma dt$. The main purpose of the accelerator upgrade is to achieve a 40 times higher luminosity with respect to its predecessor KEKB. This will lead to larger data samples, allowing precision measurements.

2.2.1 Nano-beam scheme

One of the keys of the upgrade is the “nano-beam” scheme [28]. The transverse beam size $\sigma(s)$ calculated as a function of the position s along the nominal beam trajectory is given by

$$\sigma(s) = \sqrt{\epsilon\beta(s)}, \quad (2.2)$$

where ϵ is the emittance and $\beta(s)$ is the so called betatron function, that describes dispersion effects as a function of the position around the accelerator circumference.

The idea is to squeeze the vertical betatron function at the interaction point (IP) by minimizing the overlap-region longitudinal size of the two beams at the IP. Given the quadratic dependence on s of the betatron function near the IP, and Eq. (2.2), the beam size grows linearly with the distance from the IP. This is especially important when the betatron function at the interaction point (β^*) approaches the bunch length. In this case not all particles collide at the minimum of the transverse beam size. This phenomenon is called *hourglass effect* and can reduce the luminosity [29]. Usually the relation $\beta_y^* > d$ is preserved during the accelerator tuning. Figure 2.3 shows a two-dimensional representation

of the nano-beam scheme.

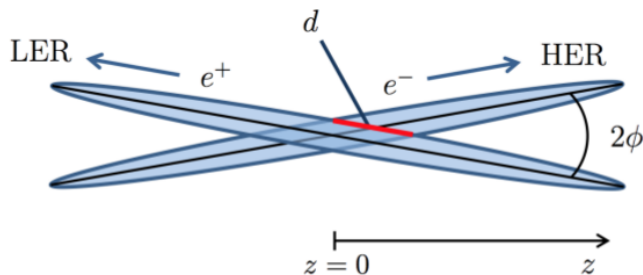


Figure 2.3: Two-dimensional sketch of the nano-beam mechanism. d is the overlap of the two beams while 2ϕ is the crossing angle.

The size of the overlap region d is considered to be the effective bunch-length for the nano-beam scheme and is smaller than the bunch length (σ_z). The length d is determined by the horizontal half crossing angle (ϕ) between the two beams and the horizontal beam size at the IP (σ_x) as $d \simeq \sigma_x / \phi$. The length d is shortened by a relatively large horizontal crossing angle and extremely small horizontal emittances and horizontal betatron functions at the IP.

A smaller betatron function increases the instantaneous luminosity,

$$\mathcal{L} = \frac{N_- N_+ n_b f_0}{2\pi \sqrt{(\sigma_{x-}^{*2} + \sigma_{x+}^{*2})(\sigma_{y-}^{*2} + \sigma_{y+}^{*2})}}, \quad (2.3)$$

where N , n_b and f_0 are the number of particles per bunch, the number of bunches, and the revolution frequency, respectively. σ_x^* and σ_y^* are the beam horizontal and vertical dimensions at the interaction point. The suffix \pm labels quantities specific of the positron (+) or the electron (-) beams. Therefore, given Eq. (2.2), the luminosity is inversely proportional to the square root of the vertical betatron function at the IP (β_y^*). Table 2.2 shows the values of these parameters, comparing SuperKEKB and KEKB.

	KEKB (LER / HER)	SuperKEKB (LER / HER)
E (GeV)	3.5 / 8.0	4.0 / 7.0
crossing angle 2ϕ	22 mrad (1.3°)	83 mrad (4.8°)
n_b	1584	2500
β_y^* (mm)	5.9 / 5.9	0.27 / 0.30
I (A)	1.64 / 1.19	3.60 / 2.62
σ_x^* (μm)	80 / 80	7.75 / 10.20
σ_y^* (nm)	1900 / 940	59 / 59
\mathcal{L} ($10^{35} \text{ cm}^{-2} \text{ s}^{-1}$)	0.211	8

Table 2.2: Comparison between KEKB and SuperKEKB main parameters.

The vertical betatron functions at the IP for SuperKEKB are smaller by almost a factor of 20 than those of the KEKB. Assuming these parameters, doubled beam currents

are sufficient to achieve the 40-fold increase in luminosity. Figure 2.4 shows a three-dimensional sketch of the bunch-crossing geometry at the interaction point for KEKB and SuperKEKB. The figure highlights the larger crossing angle and the smaller vertical size, obtained through the accelerator upgrade.

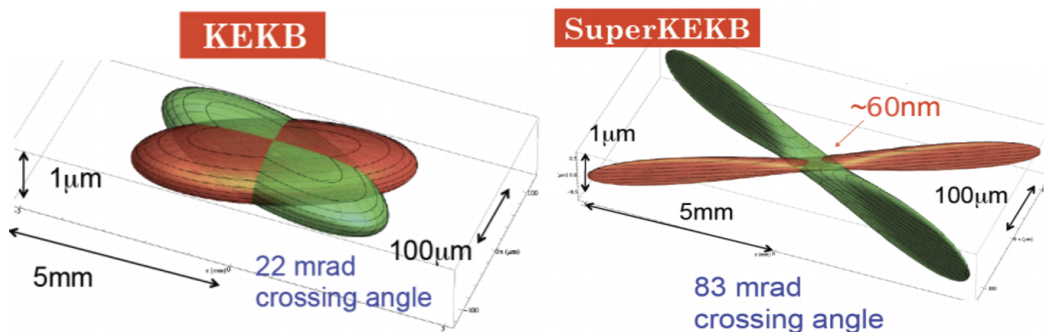


Figure 2.4: Three-dimensional sketch of the bunch crossing geometry at the interaction point for KEKB and SuperKEKB.

2.2.2 Interaction region

The horizontal crossing angle $\phi = 41.5$ mrad is about four times larger than that of the KEKB. The choice of the angle contributes to decrease the effective bunch length d .

Other factors determine the crossing angle such as the optics of the interaction region (IR), the magnet design, and the detector background. With a large crossing angle, the final-focus quadrupole magnets can be made independent for the two beams. This reduces the detector background due to synchrotron radiation. These magnets can be moved closer to the IP to achieve small betatron functions.

The interaction-region optics has been changed with respect to KEKB. A new final focus (FF) section strongly squeezes the colliding beams in both the horizontal and vertical planes at the IP. Figure 2.5 shows a scheme of the final focusing system in the interaction region.

The nominal values for the betatron functions at the IP are 32 mm in the horizontal plane and 270 μm in the vertical plane for the LER, 25 mm in the horizontal plane and 300 μm in the vertical plane for the HER, respectively. To squeeze the betatron functions, doublets of vertical focusing quadrupole magnets (QC1s) and horizontal focusing quadrupole magnets (QC2s) are used. Dedicated solenoids compensate the solenoid field of Belle II on each side of the IP.

2.2.3 Damping ring and RF system

After production, the positron emittance is larger than required for injection in the nano-beam scheme. A new damping ring (DR) accepts the beam with large energy spread and transverse emittance and reduces the emittance by a factor of 130.

After production, electrons and positrons are accelerated by the Linac to 7 GeV and 4 GeV respectively. To maintain circulating beams, radio-frequency (RF) devices are used. The KEKB RF system is upgraded to deal with doubled beam currents. To reduce the power consumption of the RF cavities, the HER energy is lowered from 8 GeV to 7 GeV resulting in a smaller boost with respect to KEKB.

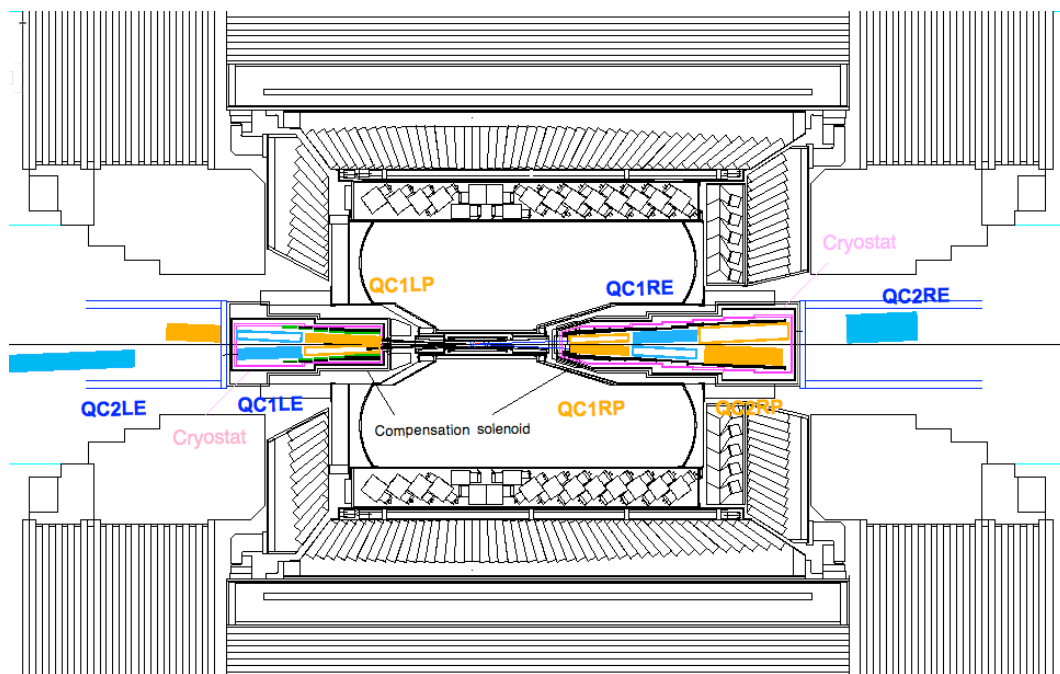


Figure 2.5: Schematic layout of the magnets and beam line near the interaction point [30].

2.3 Belle II detector overview

The Belle II detector shares with its predecessor, Belle, the location and the overall design. Given the more ambitious physics goals, its subsystems are either new or considerably upgraded.

Due to the increased luminosity Belle II operates at 40 times higher event rates. A fast, efficient online event-selection (trigger) is required as well as reinforced data acquisition capabilities. By increasing luminosity, backgrounds rates, detector occupancies, and radiation damage are expected to be higher, as well as pile-up noise in the electromagnetic calorimeter and neutron induced hits in the muon detection system.

To complete its program Belle II should provide an excellent vertex resolution (about $20 \mu\text{m}$), high reconstruction efficiencies and good momentum resolution from few tens of MeV/c to $8 \text{ GeV}/c$. An efficient particle-identification system is required to separate pions from kaons and to identify electrons and muons.

Moving from the innermost to the outermost radii, the main Belle II subdetectors are

- **Pixel detector - PXD:** two layers of silicon pixel sensors provide two dimensional position information for charged particles. The PXD is used to increase vertex resolution. The first layer is closer to the beam pipe than the Belle innermost silicon layers.
- **Silicon vertex detector - SVD:** four layers of double-sided silicon strip detectors provide two-dimensional position information for charged particles. SVD is used for vertexing and tracking. Its readout is faster than the Belle predecessor. SVD and PXD form the vertex detector (VXD).
- **Central drift chamber - CDC:** wire drift chamber used to sample the trajectories of charged particles at large radii and also for trigger, tracking and particle ID.

- **Charged particle identification systems - TOP and ARICH:** Cherenkov light is used to identify particles in the barrel region (time of propagation, TOP) and in the endcaps regions (aerogel ring imaging Cherenkov, ARICH). These systems are new.
- **Electromagnetic calorimeter - ECL:** homogeneous calorimeter that is reused from Belle to measure the energy of photons, electrons and kaons, for trigger tasks and for luminosity measurements.
- **Superconducting coil:** NbTi/Cu coil that provides a homogeneous magnetic field of 1.5 T parallel to the beam direction in the inner volume. It has new power and cooling systems, while the Belle iron structure is reused.
- **K_L^0 and muon system - KLM:** alternating layers of resistive plate chambers and iron plates in the barrel regions and scintillator strips in the endcaps. It is used to detect muons and K_L^0 that escape from the internal region. Its iron structure is used as return yoke for the magnetic field.

Table 2.3 summarizes the principal specifications of each subdetector. Figure 2.6 shows a top view of Belle II.

Purpose	Name	Component	Configuration	Readout channels	θ coverage
Beam pipe	Beryllium		Cylindrical, inner radius 10 mm, 10 μm Au, 0.6 mm Be, 1 mm paraffin, 0.4 mm Be		
Tracking	PXD	Silicon pixel (DEPFET)	Sensor size: $15 \times (L1 \ 136, L2 \ 170)$ mm ² , Pixel size: $50 \times (L1a \ 50, L1b \ 60, L2a \ 75, L2b \ 85)$ μm^2 ; two layers at radii: 14, 22 mm	10M	[17°;150°]
	SVD	Silicon strip	Rectangular and trapezoidal, strip pitch: $50(p)/160(n) - 75(p)/240(n)$ μm , with one floating intermediate strip; four layers at radii: 38, 80, 115, 140 mm	245k	[17°;150°]
	CDC	Drift chamber with He-C ₂ H ₆ gas	14336 wires in 56 layers, inner radius of 160mm outer radius of 1130 mm	14k	[17°;150°]
Particle ID	TOP	RICH with quartz radiator	16 segments in ϕ at $r \sim 120$ cm, 275 cm long, 2cm thick quartz bars with 4×4 channel MCP PMTs	8k	[31°;128°]
	ARICH	RICH with aerogel radiator	2×2 cm thick focusing radiators with different n , HAPD photodetectors	78k	[14°;30°]
Calorimetry	ECL	CsI(Tl)	Barrel: $r = 125 - 162\text{cm}$, end-cap: $z = -102 - +196\text{cm}$	6624 (Barrel), 1152 (FWD), 960 (BWD)	[12.4°;31.4°], [32.2°;128.7°], [130.7°;155.1°]
Muon ID	KLM	barrel:RPCs and scintillator strips	2 layers with scintillator strips and 12 layers with 2 RPCs	θ 16k, ϕ 16k	[40°;129°]
	KLM	end-cap: scintillator strips	12 layers of (7-10) \times 40 mm ² strips	17k	[25°;40°], [129°;155°]

Table 2.3: Summary of the Belle II components and specifications.

2.4 Vertex detector

The vertex detector (VXD) is designed to sample the trajectories of charged particles in the vicinity of the IP and therefore infer the decay position of long-lived particles.

Due to the small distance from the IP, the vertex detector has to withstand high backgrounds. Hence, the two innermost layers of the VXD are realized with pixel sensors rather than with silicon strip sensors. This choice lowers the expected fraction of channels hit in each triggered event (occupancy) below 3%.

2.4.1 Pixel detector

The PXD primary goal is to reconstruct charged particle trajectories while sustaining high hit rates.

PXD is based on the DEPFET (depleted field effect transistor) technology: a p-channel MOSFET is integrated onto a silicon substrate, which is fully depleted applying a suitable voltage. Incident particles generate electron-hole pairs within the fully depleted bulk. During readout the holes drift to the back contact, while electrons modulate the channel current through the MOSFET.

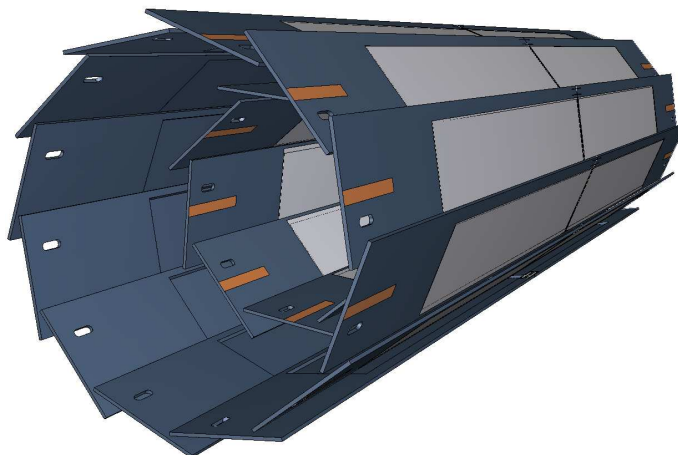


Figure 2.7: Schematic view of the PXD sensors. The light grey surfaces are the sensitive DEPFET pixels [30].

Belle II has adopted a $75\ \mu\text{m}$ -thick pixel detector, allowing to have part of the electronics integrated with the sensors and to move the remaining readout electronics, which needs cooling, away from the interaction region. DEPFET sensors also show good radiation hardness properties.

The PXD consists of two layers of sensors, with radii at 14 mm and 22 mm for a total of around 8 million pixels (Fig. 2.7). The full length of the outer modules is 174 mm. The pixel dimensions vary from $50 \times (50 - 55)\ \mu\text{m}^2$ (inner layer) to $50 \times (70 - 85)\ \mu\text{m}^2$ (outer layer). The polar acceptance ranges from 17° to 150° .

The spatial resolution is $20\ \mu\text{m}$. To reach that, the position of the traversing charged particle is obtained by weighting the different amounts of charge measured in neighboring pixels. The smaller separation between B vertices in an event due to the smaller Belle II boost with respect to Belle is compensated by a reduced radius of the first detector layer. Large backgrounds associate with high data rate, about 20 Gbit/s for 3% of occupancy. Data is reduced using information from other detectors, especially SVD. The distinction between physics and background hits relies on the extrapolation of tracks reconstructed in

the SVD and propagated back to the PXD. Around each intersection point of a track with the PXD, a region of interest is defined. If a fired PXD pixel lies inside the region, it is kept; otherwise, it is discarded.

2.4.2 Silicon vertex detector

The SVD primary goal is to reconstruct interaction vertices and low momentum charged-particle tracks efficiently and with high resolution.

SVD is based on double-sided silicon strip technology: each SVD sensor works as a reverse-biased p-n junction. The bulk of the silicon layer is n-doped and on one side of the silicon layer a highly doped p-implant is realized. By applying a bias voltage the depletion region is increased on the p-n junction. Inside the depleted region, the intrinsic carriers are removed so the e-h pairs produced by charged particles are detected. They drift, following the electric field, to the edge of the depleted region where charge collection electrodes are located.

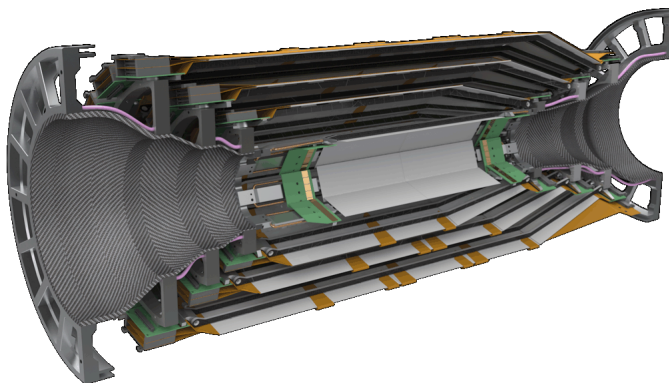


Figure 2.8: Schematic view of a half of the SVD. The readout electronics and the mechanical support are also shown [30].

SVD is made of four layers at 39 mm, 80 mm, 104 mm, and 135 mm from the beam. These layers are composed respectively of 7, 10, 12, and 16 modules (ladders) (Fig. 2.8). The space between consecutive strips (strip pitch, d_{pitch}) ranges across sensors and sides from 50 μm to 240 μm . All the sensors are 300 μm thick. The polar angular acceptance ranges from 17° to 150°. It is asymmetric to account for the forward boost of the center-of-mass frame.

The SVD spatial resolution is a function of the polar angle, but is expected to range around 20 μm , typically. SVD is segmented and has a reduced readout latency to deal with the high hit rate. The material is kept as low as possible to interfere the least with low momentum particles.

The two-dimensional position reconstruction has resolution of $d_{pitch}/\sqrt{12}$. However usually the charge is not collected on a single strip but it is distributed over several strips allowing an improved position resolution by interpolation.

2.4.3 Magnet

The solenoidal magnet primary goal is to curve charged-particle trajectories allowing momentum measurements.

A 1.5 T magnetic field is provided by a superconducting solenoid within a cylindrical volume 3.4 m in diameter and 4.4 m in length. The iron structure of the Belle II detector

is used as the return path for the magnetic flux. It consists of a fixed barrel part and movable end-cap parts. The solenoid is made of NbTi/Cu and it is powered with 4400 A.

2.4.4 Radiation monitor system

The radiation monitor system is based on artificial single crystal diamond sensors. Its main goal is to protect the silicon vertex detector from high radiation doses that would deteriorate its performances. A critical feature of the radiation monitor system is the generation of beam abort requests to SuperKEKB if the radiation doses near the interaction region are higher than a certain threshold. The other main goal of the diamond system is to constantly

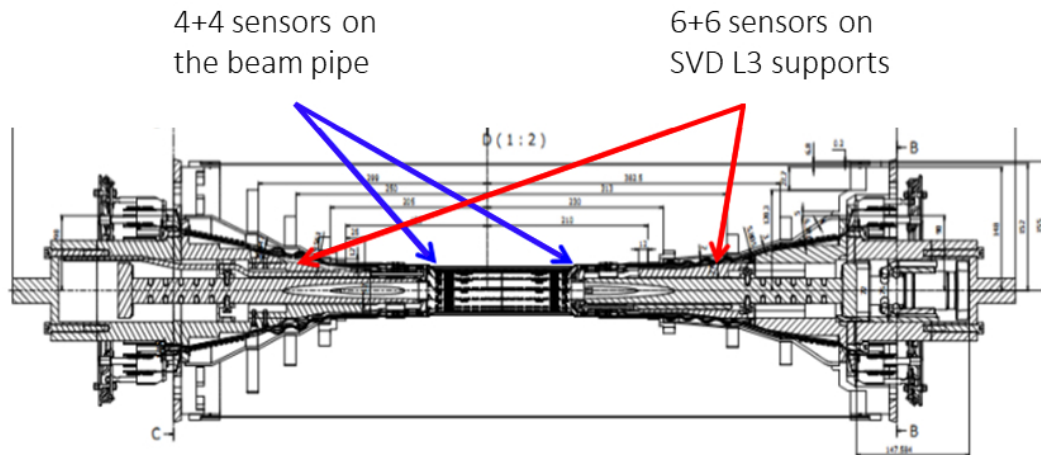


Figure 2.9: Diamond-detector geometry for the Belle II final setup. Eight sensors are mounted on the beam pipe and twelve on the SVD layer 3 supports.

measure the radiation level near the interaction point. These measurements are used to estimate the total dose absorbed by the silicon detector and to monitor the background evolution as the accelerator conditions change.

Figure 2.9 shows the monitor final setup. It consists of eight diamond detectors mounted on the beam pipe. Four are on the forward part and four on the backward. Twelve diamonds are mounted on the SVD layer 3 supports, half of them mounted on the forward part and half on the backward.

The radiation monitor system, on which I have worked characterizing the diamond detectors and operating it during Belle II commissioning, is described in more detail in the next chapters.

2.5 Central drift chamber

The central drift chamber (CDC) plays three important roles: it reconstructs charged particles by sampling their trajectories at large radii; it identifies them by using measurements of specific energy loss; it also provides trigger signals for charged particles.

The CDC working principle is based on charged-particle ionization energy loss in a gaseous medium: as a charged particle crosses the CDC volume, it releases energy that is partially used to create free electrons and positive ions from the gas atoms inside the CDC volume. An external electric field makes the charged carriers drift until they shower near the cathodes. The time between the collision and the CDC signal is then used to infer the particle position.

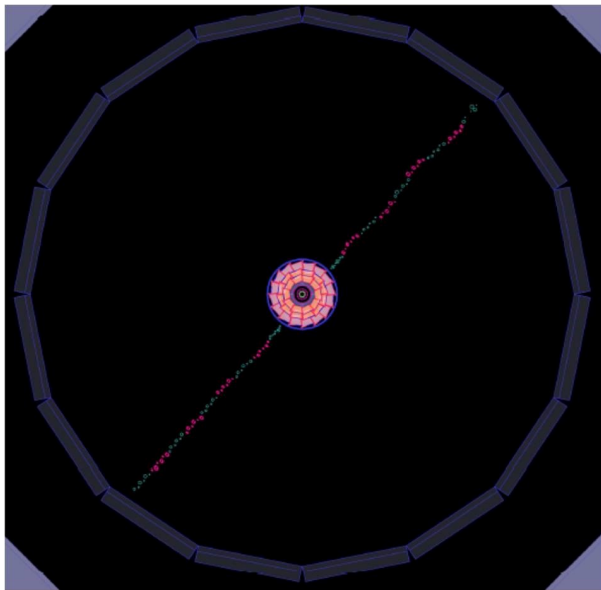


Figure 2.10: Cosmic ray reconstruction in the CDC.

CDC is made of 56 layers of wires within a gas mixture (50% He and 50% C₂H₆). Ethane has low radiation length, good position resolution, good energy loss resolution, low cross section for synchrotron radiation X-rays, and suffers little radiation damage.

The CDC radius ranges from 160 mm to 1130 mm. The azimuthal acceptance ranges from 17° to 180°. More than 10^4 30 μm -diameter tungsten wires collect the charge released by particles. More than 4×10^4 126 μm -diameter aluminum wires shape the drift electric field. Figure 2.10 shows a CDC reconstructed track created by a cosmic ray.

The spatial resolution is about 100 μm . The specific ionization, dE/dx , resolution is 11.9% for an incident angle of 90°.

2.6 Detectors for particle identification

Two main detectors are devoted to particle identification (PID). The time of propagation counter (TOP) in the barrel region and the Aerogel ring imaging Cherenkov counter (ARICH) is in the forward end-cap. Both detectors use Cherenkov light to identify charged particles.

2.6.1 Time of propagation

The TOP measures the time of propagation of the Cherenkov photons produced by charged particles and internally reflected inside a quartz radiator. A three-dimensional image is reconstructed from the x and y coordinates of the photon hits and from the propagation time. A photon originated from a heavy charged particle would, on average, arrive at a later time than one that originated from a light one. This is due to the mass difference and the inverse proportionality between the cosine of the Cherenkov angle and the particle velocity.

The TOP is made of 16 quartz bars mounted on the barrel at 1.2 m from the interaction point. Each bar is a photon radiator and has three main components. A long bar for radiating Cherenkov light and propagating it to the bar end; a spherical mirror mounted on the forward end of the bar for focusing the light; a prism attached to the backward end

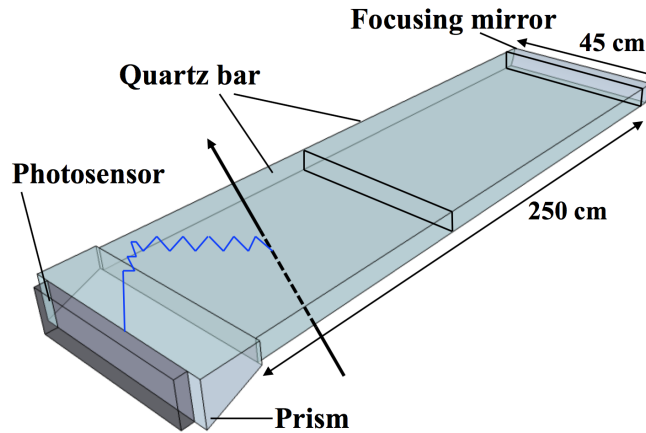


Figure 2.11: Representation of a TOP counter. The figure shows a charged particle that crosses the radiator and emits Cherenkov light. Light is absorbed by a photomultiplier and converted into an electric signal.

of the bar that drives the light to micro-channel plate photomultipliers. The polar angular acceptance ranges from 31° to 128° . Figure 2.11 shows a scheme of a quartz bar.

The time resolution is about 100 ps. TOP is expected to achieve a good separation of pions and kaons from 0.4 GeV/c up to 4 GeV/c.

2.6.2 Aerogel ring-imaging Cherenkov counter

The primary goal of the aerogel ring-imaging Cherenkov counter (ARICH) is to separate kaons from pions over most of their momentum spectrum. It is used also to provide discrimination between pions, muons and electrons below 1 GeV/c.

An aerogel radiator produces Cherenkov photons as a charged particle crosses it. In front of the radiator, an expansion volume allows Cherenkov photons to form rings on the photon detector surface. These photons are then collected by an array of position-sensitive photo-diodes. A photocathode is used to generate photoelectrons that are accelerated using an electric field and multiplied in an avalanche. A readout system provide the photon hit positions.

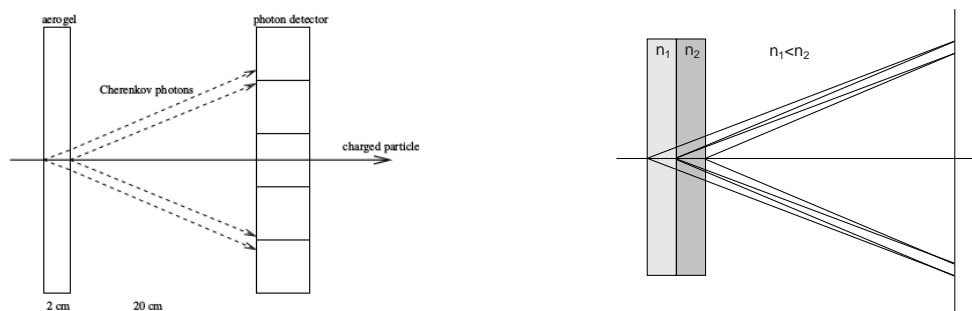


Figure 2.12: Scheme of the ARICH detector (left panel) and the inhomogeneous configuration of the aerogel radiator (right panel).

Figure 2.12 shows the main parts of the ARICH detector. Two consecutive aerogel radiator layers with different refraction indices are used to generate enough photons to maintain sufficient resolution.

The ARICH container consists of two cylinders with inner and outer radii of 410 mm and 1140 mm, respectively. The polar angular acceptance ranges from 14° to 30° .

The expected ARICH performances would enable better than 5σ pion-kaon separation at the kinematic limit of 4 GeV/ c . Pions would be separated by 4σ from electrons up to about 1 GeV/ c .

2.7 Electromagnetic calorimeter

The electromagnetic calorimeter (ECL) primary goals are to measure energy of photons, electrons and pions, measure luminosity and generate a proper trigger signal.

The ECL working principle is based on scintillation: the energy released in particular scintillating materials by an impinging particle is partially converted into light that is collected by photodiodes.

The ECL consists of a 3 m long barrel section with an inner radius of 1.25 m, annular endcaps are at $z = 1.96$ m (forward) and $z = -1.02$ m (backward) from the interaction point. The calorimeter covers the $12.4^\circ < \theta < 155.1^\circ$ polar angle region. The active material for the barrel part is CsI(Tl) (repurposed from the Belle calorimeter). It has been chosen because of its high light output, relatively short radiation length, and good mechanical properties. The endcaps consists of CsI crystals which have a lower scintillation decay time allowing the reduction of background photons due to the high luminosity.

Approximately one third of B decays involve π^0 mesons and neutral particles. These decay products generate photons in a wide energy range (20 MeV - 4 GeV). High resolution and efficiency are therefore fundamental requirements for the ECL.

2.8 K_L^0 and muon system

The K_L^0 and muon detector (KLM) contributes to the identification of muons and detects neutral particles that do not interact with the inner detectors, such as K_L^0 .

The working principle is based on scintillators in the inner layers and glass-electrode resistive-plate chambers in the outer layers. A gas mixture fills the space between the chambers electrodes. After applying an appropriate voltage, the charge produced by a traversing charged particle is collected. Charged particles can be produced by K_L^0 mesons through hadronic showers interacting with the iron plates.

The KLM is made of alternating pattern of 4.7-cm thick iron plates and active detector elements. The iron plates serve as the magnetic flux return for the solenoid and they also provide 3.9 interaction lengths in which K_L^0 mesons can shower hadronically. The barrel section of the detector covers 45° to 125° in polar angle. The endcaps cover 20° to 45° and 125° to 155° .

The muon and K_L^0 reconstruction efficiencies are higher than 80% if the momentum is larger than 1 GeV/ c and 3 GeV/ c respectively. Muons are identified by extrapolating outwards the particle track and calculating a predicted range. If the predicted and actual ranges agree the particle is identified as a muon.

2.9 Trigger

The trigger primary goal is to identify and record the events of interest during data taking.

The trigger system must be efficient for hadronic events from $\Upsilon(4S) \rightarrow B\bar{B}$ and from the continuum. It must have a maximum accept rate of 30 kHz due to data acquisition

restrictions. Some events like hadronic processes are straightforward to select due to their distinctive high-track multiplicity. Other events like leptonic τ decays and those related to dark-matter searches have only few tracks in the final state.

The rates of different processes are calculated based on the goal luminosity ($8 \times 10^{35} \text{cm}^{-2}\text{s}^{-1}$) and the total cross sections (Table 2.4 shows some examples).

Physics process	Cross section (nb)	Rate (Hz)
$\Upsilon(4S) \rightarrow B\bar{B}$	1.2	960
Hadron production from continuum	2.8	2200
$\mu^+\mu^-$	0.8	640
$\tau^+\tau^-$	0.8	640
Bhabha ($\theta_{\text{lab}} \geq 17^\circ$)	44	350 ^(a)
$\gamma\gamma$ ($\theta_{\text{lab}} \geq 17^\circ$)	2.4	19 ^(a)
2γ processes ($\theta_{\text{lab}} \geq 17^\circ, p_t \geq 0.1 \text{ GeV}$)	$\simeq 80$	$\simeq 15000$
Total	$\simeq 130$	$\simeq 20000$

^(a) rate is pre-scaled by a factor 1/100

Table 2.4: Total cross sections and trigger rates with $\mathcal{L} = 8 \cdot 10^{35} \text{cm}^{-2}\text{s}^{-1}$ for various physics processes at $\Upsilon(4S)$.

The Belle II trigger system is composed by a hardware level 1 trigger (L1) and a high level trigger (HLT) based on software.

The L1 trigger is based on several sub-trigger signals that are combined to obtain the final trigger decision. The sub-trigger composition is done by a global reconstruction logic that feeds the global decision logic. The global decision logic sends out the final trigger signal based on all the input information that it receives.

The main subdetectors that contribute to the trigger are the CDC and the ECL. Also the TOP and KLM signals are used inside the L1 trigger logic. One of the main tasks of the L1 trigger is to reject background events, reducing the data rate. This is done by reconstructing the longitudinal position (z) of the interaction vertex: if the vertex is away from the IP the event is rejected.

The HLT is based on a complete software reconstruction of the event. It uses the charged particle tracks from the CDC and the electromagnetic showers in ECL. It performs an event selection based on track multiplicity, vertex position and total energy deposition. With the HLT a 12.5% event rate reduction is expected, without efficiency loss.

Chapter 3

Beam backgrounds and monitoring

In this chapter the main sources of accelerator beam losses and backgrounds are discussed, highlighting their dependencies on the accelerator conditions. Possible damage to the silicon vertex detector associated with such backgrounds is also described.

Finally this chapter presents the main features and capabilities of diamond sensors used as radiation monitors.

3.1 Accelerator backgrounds

While beams are circulating, various processes may perturb the motion of the beam particles. These processes often generate backgrounds that need to be understood and controlled in order to safely operate the machine and the detector [31].

- **Touschek scattering** is a single electromagnetic scattering between two particles of the same bunch. The momentum transferred in the collision may deviate one or both particles outside the momentum acceptance [32], resulting in their loss. Touschek collisions are possible because, due to the momentum and energy spread of particles within the same bunch, particles undergo betatron and synchrotron oscillations during their motion. Given the Touschek scattering probability [33], the total scattering rate (r_T) is proportional to the number of filled bunches (n_b), the square of the bunch current (I_b), the inverse of the horizontal and vertical bunch sizes (σ_x and σ_y), the inverse of the bunch length (σ_z), and the inverse third power of accelerated-particle energy (E),

$$r_T \propto \frac{n_b I_b^2}{\sigma_x \sigma_y \sigma_z E^3} . \quad (3.1)$$

Higher beam currents along with a smaller beam size imply a large increase of Touschek scattering in SuperKEKB with respect to its predecessor KEKB.

Particles lost due to Touschek scattering hit the beam-pipe inner wall, producing electromagnetic showers. If this occurs near the interaction point, the shower products can reach the detector, generating signals not related to collisions.

Movable metallic blocks mounted inside the beam pipe (collimators) are used to mitigate the effects of Touschek scattering. These devices stop off-trajectory particles, not allowing them to reach the interaction region. During the accelerator design it has been decided to increase the LER energy to 4 GeV: this choice reduces the Touschek LER background.

- **Beam-gas scattering** is a scattering of beam particles with residual gas molecules in the beam pipe. The particle-molecule interaction may occur through two different processes: Coulomb scattering, which changes the direction of the beam particle; and bremsstrahlung scattering, which also reduces the energy of the beam particle, through photon emission. Beam-gas scattered particles are lost by hitting the beam pipe inner wall while they propagate around the ring.

The beam-gas scattering rate (r_{BG}) is proportional to the beam current (I) and to the pressure (P) inside the beam pipe.

$$r_{BG} \propto IP = p_0I + p_1I^2 \quad (3.2)$$

Two components contribute to the pressure, a pressure without beams (p_0), and a dynamical component that depends on the total beam current (p_1). This second term is related to desorption effects: previously absorbed gas molecules can be re-emitted by the beam pipe walls. An improvement of the vacuum quality is usually achieved by *baking* and *vacuum-scrubbing*. During *baking*, sections of the beam pipe are heated up and the released gas molecules are extracted using vacuum pumps. *Vacuum-scrubbing* consists in letting the beams circulate without collisions to stimulate the re-emission of molecules absorbed by the beam-pipe walls and their extraction by vacuum pumps.

The beam-gas background is reduced by tuning the collimator positions.

- **Synchrotron radiation** (SR) is the emission of photons by accelerated charged particles. The power emitted (W_S) is proportional to the beam energy (E) squared, the magnetic field strength (B) squared, the inverse fourth power of the mass (m), and the inverse square of the curvature radius (ρ).

$$W_S \propto \frac{E^2 B^2}{m^4 \rho^2} \quad (3.3)$$

Given the proportionality to the beam energy squared, the HER beam is the main source of this background. Since the sources of SR background are the accelerated particles, the photon emission rate is proportional to the beam current.

The energy spectrum of SR photons ranges from a few keV to tens of keV. In order to protect the vertex detector from SR-induced damage, the shape of the beam pipe in the interaction region is designed to avoid direct SR hits at the detector and its inner surface is coated with a gold layer to absorb SR photons. However, during the accelerator commissioning we observed a SR-component in the particle energy spectrum detected by dedicated sensors placed around the IP. Beam-pipe materials irradiated by SR were found to emit fluorescence photons that interact with surrounding detectors.

- **Radiative Bhabha process** is an electron-positron scattering process where a photon is present in the final state, in addition to the initial particles, $e^+e^- \rightarrow e^+e^-\gamma$ (Fig. 3.1). Radiative Bhabha photons can interact with the iron of the accelerator magnets, producing low-energy gamma rays and neutrons. Low-energy gamma rays contribute to the background for the CDC and for the barrel particle identification systems. Neutrons are the main background source for the outermost detectors like KLM. Neutron shielding is used in the accelerator tunnel to reduce their flux.

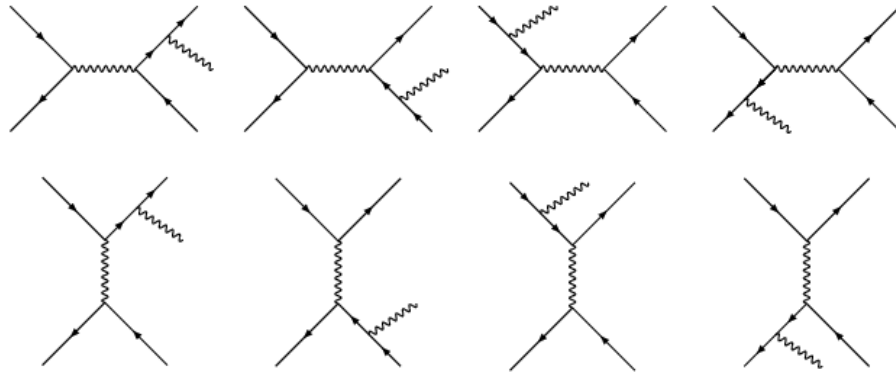


Figure 3.1: Leading-order Feynman diagrams that contribute to the radiative Bhabha process.

By emitting a photon, electrons and positrons lose energy and may then hit the beam pipe walls, producing electromagnetic showers in turn.

Bhabha scattering is also important for luminosity measurements. The Bhabha cross section is large and dominated by electromagnetic interactions. Therefore it is possible to use perturbative QED and predict the cross section with high accuracy. Luminosity is calculated starting from the known cross section by determining the Bhabha rate in a region of known acceptance.

- **Two photon process** is the QED process $e^+e^- \rightarrow e^+e^-e^+e^-$. Low momentum electron-positron pairs can spiral around the magnetic field lines of the Belle II solenoid leaving multiple hits in the inner Belle II detectors. The primary particles that lose a large amount of energy or scatter at large angles can be lost inside the detector, as with radiative Bhabha. As the background particles interact with the inner detector, they increase the hit multiplicity, making tracking more difficult.

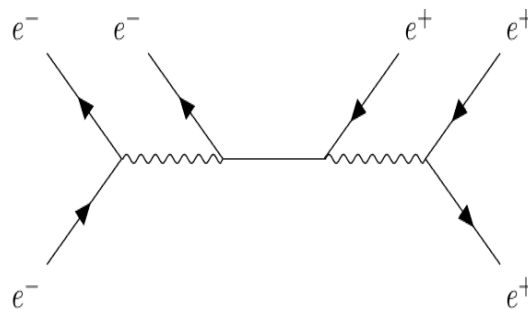


Figure 3.2: Leading-order Feynman diagram for the two-photon process.

- **Injection background** is caused by charge injection in a circulating beam bunch. The main difference between the stored particles and injected particles is the oscillation amplitude around the bunch center. Injected particles oscillate with larger amplitudes and they can be lost in Belle II detector. After each injection the bunch is perturbed and a higher background rate is observed in the detector for few milliseconds after the injection. A veto signal is applied to PXD detector to prevent the detector readout during each injection.

All these backgrounds strongly depend on the beam optics. According to preliminary estimates, the PXD total integrated dose may range from about 150 to about 180 kGy (15 to 18 Mrad) during the projected lifetime of Belle II at the design integrated luminosity (50 ab^{-1}). For the inner and less exposed layers of the SVD approximately 4.5 Mrad are expected to be integrated during the same Belle II activity period [34].

We used these estimates to approximately determine the radiation dose-rate thresholds for beam abort requests, needed to prevent the vertex detector from integrating radiation doses significantly higher than the design values.

3.2 Radiation damage to silicon detectors

All background sources described in Section 3.1 can damage the VXD sensors, deteriorating its tracking performances as the absorbed dose increases. For proper charged particle pattern recognition the signal-to-noise ratio of the silicon vertex detector has to remain in excess of 10 during the whole duration of Belle II data taking. In order to protect the inner detectors, whose tracking capabilities are essential for the Belle II physics program, a radiation monitoring and interlock system has to be mounted near the IR.

In this section the main sources of damage related to radiation in semiconductor devices are presented. Changes in the macroscopic behavior are traced back to microscopical lattice structure changes [35].

3.2.1 Radiation-induced defects

Depending on radiation type and energy, the interaction may involve the electrons of the silicon crystal or the Si nuclei in the lattice. Typically, the interaction with the electrons is a transient effect and it is used for detecting particles. On the other hand, the interaction with the nuclei may lead to permanent damage. Lattice atom displacement generates interstitials (atoms between regular lattice sites) and vacancies (empty lattice sites). These defects are unstable, they can mitigate, partially anneal or combine with other defects to form more stable defects, which may change the electrical properties of the semiconductor.

Displaced lattice atoms with enough energy can cause secondary cascade processes. An impinging particle has to transfer at least 15 eV to a silicon atom to displace it from its lattice site. For recoil energies below 2 keV, isolated defects are created. At higher energies defect clusters can also be generated, where a cluster is a dense agglomeration of point defects that appear at the end of a recoil silicon-atom track. The type and energy of the impinging radiation determine the probability of forming a primary knock-on atom, which is a silicon atom displaced from its original lattice position.

The so-called "non-ionizing energy-loss" is used to measure and compare radiation damage from different sources [36] since ionizing energy-loss does not produce crystal defects.

On a microscopic scale, defects have several consequences. They act as recombination-generation centers as they can capture and emit electrons and holes; they are also trapping centers, where electrons and holes are captured and re-emitted with some time delay; they can also be charged, affecting the space charged density in the depletion region.

Beside displaced silicon atoms, radiation can also affect the dielectric layers present in silicon devices and the interfaces between them and the silicon. The main effects are a charge build up in the oxide and an increase in the interface trap density.

3.2.2 Effects on detector properties

The microscopic lattice defects induce several changes in the properties and operating parameters of a detector.

- **Operating voltage:** radiation damage may change the space charge density in the silicon depletion region. As a consequence, the bias voltage necessary to deplete the bulk changes. Radiation-originated defects can interact with dopants such as phosphorus present in n-type substrates used for the SVD sensors, changing their charge state and preventing them from fulfilling their role as donors (donor removal). In addition they act as effective acceptors. The effective doping decreases as the impinging particle fluence (number of particles that intersect a unit area of the detector) increases until an intrinsic-like condition is achieved. Increasing furthermore the fluence brings to a type inversion of the n-type silicon substrate.

During Belle II data taking, the SVD sensors are expected to suffer from donor removal, as the absorbed dose increases. Hence the applied voltage will be changed to obtain the best detector performances.

- **Reverse-bias current:** defects can emit electrons and holes, causing the generation of a reverse-bias current in the depleted volume. The major contributions to this current come from defects whose energy levels are near the band-gap center. Since the defect generation is proportional to the impinging-particle fluence, a linear relation between the leakage current increase and the fluence exists.

Bulk defects and interface traps increase the reverse-bias current in depleted volume and surface respectively.

The reverse-bias current increases the detector noise level, deteriorating the tracking performances.

- **Trapping of signal charge:** the trapping probability for charge carriers per unit time is approximately proportional to the trap concentration, which is increased by radiation-induced damage.

Unlike reverse-bias current, where only energy levels close to midgap contribute significantly, all the defects are able to trap charge carriers. Trapped charge carriers are released after some time and only if they are released early enough they can fall in the time window needed for charge collection. Otherwise, trapping decreases the charge collection efficiency (CCE) of the detector, defined as the ratio between the collected and the created charge due to an impinging particle.

Like reverse-bias current, charge trapping also lowers the detector SNR, this time by reducing the signal.

The damage sources described so far depend on the particle fluence accumulated over time on the detector. However spike-like intense and rapid energy releases may also produce additional damage. During short, intense irradiation, a very high density of carriers can be created. The silicon then behaves more like an electrical conductor, causing the applied voltage to drop across the dielectric layer of the AC coupling capacitors integrated in the SVD sensors. High voltage difference across the oxide can lead to dielectric breakdown, thus shorting the AC capacitors.

Radiation damage not only affects sensors, but also their readout electronics which is located in the same volume. However, the use of thin high-quality gate oxides in CMOS technology has reduced the effects of radiation damage [37] on readout circuits, which makes these effects less relevant for sensors.

3.3 Diamond sensors for radiation monitoring

An efficient vertex detector tracking is fundamental to achieve the Belle II flavor physics goals and the construction of a new vertex detector takes up to three or four years, with significant effort and cost. An efficient and reliable protection system is therefore needed to keep the vertex detector safe from high radiation doses and prolong its operating life as much as possible.

As the protection system measures radiation levels, the same system is also essential for monitoring beam losses, correlating them with SuperKEKB parameters. The radiation system has to operate smoothly and without severe performance degradation for the entire Belle II operation: as the SuperKEKB parameters will be optimized to achieve high luminosities, the radiation system measurements will continue to be fundamental.

Several options have been developed for radiation monitoring and beam loss detection at accelerator facilities over the years.

Gas ionization chambers are the most widely used instrument whenever enough space is available without interference with the experimental apparatus, for example along the accelerator ring.

Closer to the interaction region, where limited space is available, and the amount of material should be minimized, silicon PiN diodes have been frequently used [38–40]. These sensors have however some serious drawbacks: their reverse-bias current, that measures the instantaneous radiation dose rate, strongly depends on temperature. The dark leakage current, with no radiation present, strongly increases as the radiation damage accumulates with the integrated dose. As a result, they require frequent re-calibrations and the subtraction of a dominant dark leakage current term, that introduce large systematic errors.

Belle II chose diamond sensors as radiation monitors due to their superior performances over concurrent technologies, such as silicon PiN diodes mentioned above. Table 3.1 shows a comparison between diamond and silicon main characteristics: high-purity diamond crystals can be considered as a "wide-gap intrinsic semiconductor" with interesting properties as compared to silicon.

Property	Diamond	Silicon
Atomic number Z	6	12
Number of atoms N [10^{22}cm^{-3}]	17.7	5.0
Mass density ρ [$g\text{ cm}^{-3}$]	3.53	2.33
Band gap E_g [eV]	5.47	1.12
Resistivity ρ_c [$\Omega\text{ cm}$]	$> 10^{12}$	2.3×10^5
Electron mobility μ_e [$\text{cm}^2\text{V}^{-1}\text{s}^{-1}$]	1800	1350
Hole mobility μ_h [$\text{cm}^2\text{V}^{-1}\text{s}^{-1}$]	1200	480
Electron saturation velocity v_e^s [10^6 cm s^{-1}]	26	10
Hole saturation velocity v_h^s [10^6 cm s^{-1}]	16	7
Thermal conductivity k [$\text{W cm}^{-1}\text{K}^{-1}$]	21.9	1.5
Energy to create e-h pair E_{eh} [eV]	13	3.6
Displacement energy E_d [eV/atom]	42	15

Table 3.1: Comparison between diamond and silicon main properties at T=300K.

The high displacement energy and extreme thermal conductivity guarantee radiation resistance and a negligible temperature dependence of diamond sensors [41]. These properties

are particularly suited for operations in high radiation environments. The wide band gap allows to operate with low leakage current. The high thermal conductivity makes the diamond an interesting material for applications where active detector cooling is impractical such as in the restricted volumes around collider experiment interaction-regions. The high charge carrier mobility enables fast signal collection.

Despite these very interesting properties, a wide use of diamond for large-area applications in tracking devices has been limited by the difficulty of producing high-quality crystals and by the availability of a mature detector technology based on silicon wafers with microstrip or pixel electrodes [42,43]. The ratio between cost and sensor area is much higher in diamond detectors than in silicon. Also the diamond wafer size is limited to few cm^2 , restricting the range of applications.

One of the most effective techniques developed to grow detector-quality diamond crystals is the chemical vapor deposition (CVD) that is also used to grow diamonds used for Belle II [44].

3.3.1 Chemical vapor deposition

Diamond crystals are formed by heating carbon under extreme pressure. This process forms the basis of the traditionally used high-pressure high-temperature growth technique that emulates the growing process of natural diamonds.

More recently the possibility to grow diamond crystals at much lower pressures was developed and represented a fundamental technological breakthrough. The chemical vapor deposition (CVD) technique consists in adding carbon atoms one-at-a-time to an initial lattice template. The thermal decomposition of carbon-containing gases (precursor gases) under reduced pressure is used to grow diamond on pre-heated substrates. At room temperature and pressure, graphite is the thermodynamically stable allotrope of carbon. The growth of diamond (rather than graphite) requires that the precursor gas (usually CH_4) is diluted in excess of hydrogen, in a typical mixing ratio of 1% vol. The temperature of the substrate is usually greater than 700°C to ensure the formation of diamond rather than amorphous carbon. The process gases diffuse toward the substrate surface, passing through an activation region (e.g., a hot filament or electric discharge), which provides energy to the gaseous species. This activation is used to create reactive radicals and atoms that interact with the substrate surface to form diamond crystals.

Atomic hydrogen is the most critical component in the gas phase mixture. It etches graphite-like sp^2 carbon bonds many times faster than diamond-like sp^3 carbon bonds. The growth rate depends on the crystal area and on the used technique but its typical value is around 10 to 100 $\mu\text{m}/\text{h}$. For more details see Ref. [45].

3.3.2 Detection of charged particles

The mechanism of charged-particle detection by diamond sensors is outlined in Fig. 3.3. The energy released in the diamond bulk by an impinging charged particle produces pairs of charge carriers, electrons (e) and holes (h), through ionization.

The same mechanism is present in semiconductor materials, where an electron is promoted from the valence band to the conduction band after absorbing enough energy. This transition generates two oppositely charge carriers, an electron in the conduction band and a hole in the valence band [46]. The energy needed for the promotion from a lower to a higher band depends on the forbidden energy gap that separates the two bands and on the fraction of transferred energy that excites other degrees of freedom.

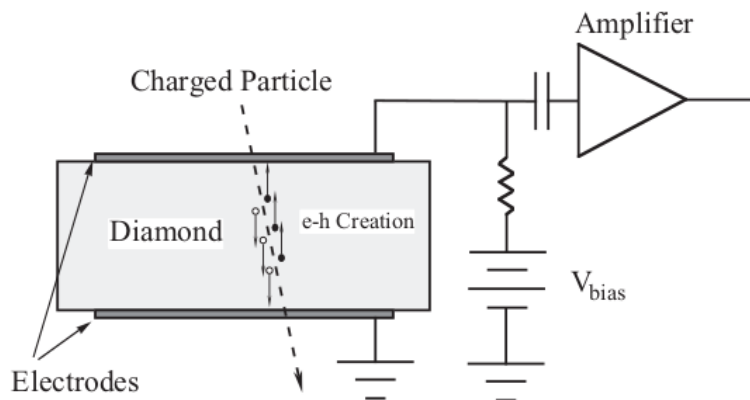


Figure 3.3: Schematic layout of a diamond sensor. The charge carriers produced by an impinging particle are collected by applying an external electric field via a bias voltage V_{bias} . The AC component of the signal is then amplified and read by an external readout system.

Electrons and holes are collected by applying an external electric field in which the charge carriers drift in opposite directions. The electric field in the diamond bulk is generated by applying to the metallic contacts a bias voltage V_{bias} of a few hundred volts. The time-dependent component of the collected signal is decoupled from the constant bias voltage with a decoupling circuit with careful impedance matching and is then amplified and recorded by an external readout system.

The measured time-dependent current is determined by several factors: the initial space distribution of charge carriers, the electric field and the resulting drift velocities. A specific case will be discussed in Section 4.3.

3.3.3 Response to neutral particles

The capability of diamond sensors to measure backgrounds depends on the efficiency in detecting the different types of particles that constitute these backgrounds.

Photons

Photon backgrounds are associated with several sources (Section 3.1). They produce primary and secondary particles that may reach the vertex detector.

The physical process subtending photon detection in diamond sensors depends on the photon energy. Photons with energies $E_\gamma < 1$ MeV can be absorbed by shell electrons via photoelectric effect. Intermediate-energy photons ($0.1 < E_\gamma < 10$ MeV) can be indirectly detected by Compton scattering, that transfers part of their energy to an electron; the charged electron is in turn detected via the usual ionization and generation of electron-hole pairs. High energy γ rays can interact with carbon nuclei producing e^+e^- pairs [47]. The probability of this process is small, due to the small amount of material in the diamond sensor. These photons are detected with higher probability if they initiate an electromagnetic shower, with charged electrons and positrons, in the material surrounding the diamond sensor.

Neutrons

Among the most harmful sources of damage for the vertex detector are neutrons. Neutrons can be produced by high-energy beam particles hitting the surrounding material and exciting nuclei.

Even if diamond has the highest atomic density of any material, contributing to the detection efficiency per unit volume [48], the interaction probability with the tiny diamond volume is very small. Furthermore Belle II diamond detectors cannot distinguish between neutron and charged-particle interactions in an effective way.

In the next chapter I discuss all the construction and characterization steps that allowed me to obtain CVD artificial single-crystal diamond detectors designed for the Belle II radiation monitor.

Chapter 4

Characterization of diamond detectors

The radiation monitoring and beam abort system of Belle II is based on diamond detectors, and will have a crucial role in protecting the vertex detector and keeping beam losses under control during the experiment life time. For this reason, accurate tests and calibrations of all individual detectors are needed, prior to their installation.

This chapter describes the steps performed to obtain working and fully characterized diamond detectors.

4.1 Assembly and first tests of diamond detectors

The Belle II diamond sensors are $(4.5 \times 4.5 \times 0.5)$ mm³ artificial single-crystals obtained by chemical vapor deposition (sCVD). Metallic electrodes are deposited on the top and bottom sides. These two electrodes, polarized by a high-voltage bias, establish the electric field that separates and makes the charge carrier drift as described in Sec. 3.3.2 [44]. Figure 4.1 shows a diamond detector used for Belle II radiation monitoring.

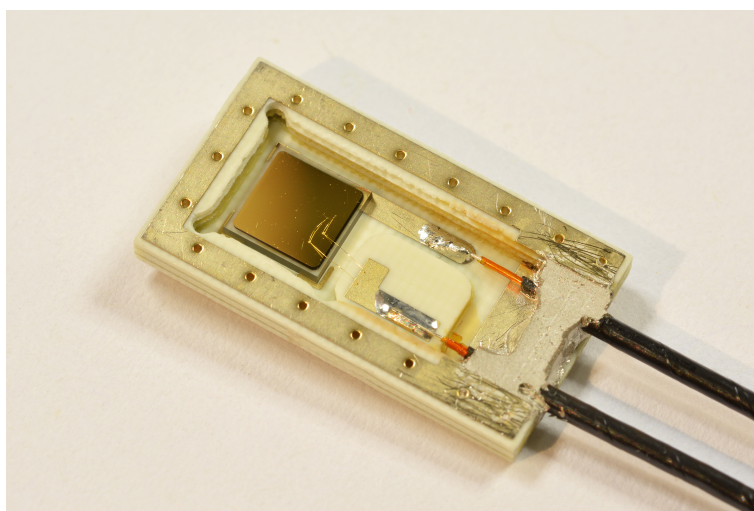


Figure 4.1: Picture of an uncovered Belle II diamond detector package.

Electrodes are (4.0×4.0) mm² (Ti + Pt + Au) layers with thicknesses of $(100 + 120 + 250)$ nm, respectively. The electrodes are radiation-resistant, and temperature-resistant up

to 400°C. The external gold layer on the electrodes facilitates wire-bonded connections to the electronics.

Several steps are needed to assemble the complete detector. The construction and test chain starts with the assembly of two SMA connectors to a 5-m-long coaxial cable. The cable is used to bias the diamond sensor and to carry the output signal. The cable is tested by applying up to 800 V between the central conductor and the surrounding shield, measuring the current, and ensuring that there is no contact between the two. The insulator resistance is obtained from the current-voltage characteristic. Typical values range between 80 TΩ and 100 TΩ. Figure 4.2 shows a linear trend in the I-V characteristic typical of an ohmic behavior. The measured resistance is about 90 TΩ in this case. The leakage

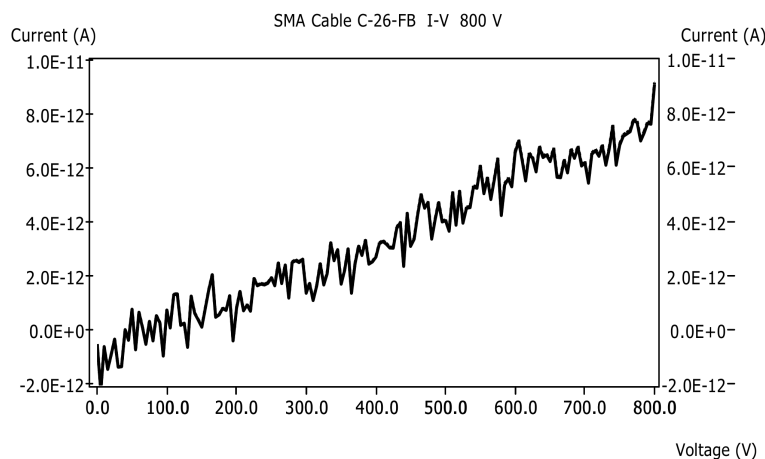


Figure 4.2: Typical current-voltage characteristic from which I obtain the insulator resistance of a coaxial cable.

current between the inner and outer conductors of the coaxial cable is typically within the pA range at 100 V of sensor operation voltage.

The tested cable is cut in two equal parts, each with one SMA connector. The central conductors of the two halves are soldered to the left and right metallic pads (Fig. 4.1). The outer conductors of the two wires are glued to the external aluminum surface of the package with conductive glue. The metalized ceramic-like package envelops the whole sensor, protecting the diamond crystal and the wire-bonds, and providing an electrical shield, connected to the outer conductor of the two coaxial cables.

After testing the electrical connections inside the package, the diamond is mounted on the central pad with conductive epoxy glue, cured by heating it up to 80° C. A preprinted path on the package establishes the connection between the lower diamond electrode and one of the two wires. The electrical connection between the top diamond electrode and the other pad is made by ball bonding with a 25 μm diameter gold wire. The connections allow to apply a bias voltage across the diamond sensor, while measuring the output current.

All electrical connections are then tested. Even if diamonds show a small sensitivity to visible light, the sensors is covered to test it under the final conditions, when an aluminum cover is glued on the package [49].

A current-voltage characteristic of the detector is obtained by applying a potential difference up to 800 V between the two electrodes via the corresponding coaxial cables.

The aim of this test is to measure currents without irradiation (dark currents) and compare them with the currents observed during irradiation, verifying that the signal is distinguishable from the noise.

Both the currents flowing into and from the sensor are read. The test is performed in two ways, providing a positive high voltage bias to the front or the back electrode, with respect to the opposite electrode, in order to detect possible differences in current flow, that can be tracked down to contributions by leakage current through the detector package or stray current through the diamond bulk. Figure 4.3 shows a typical result of this test.

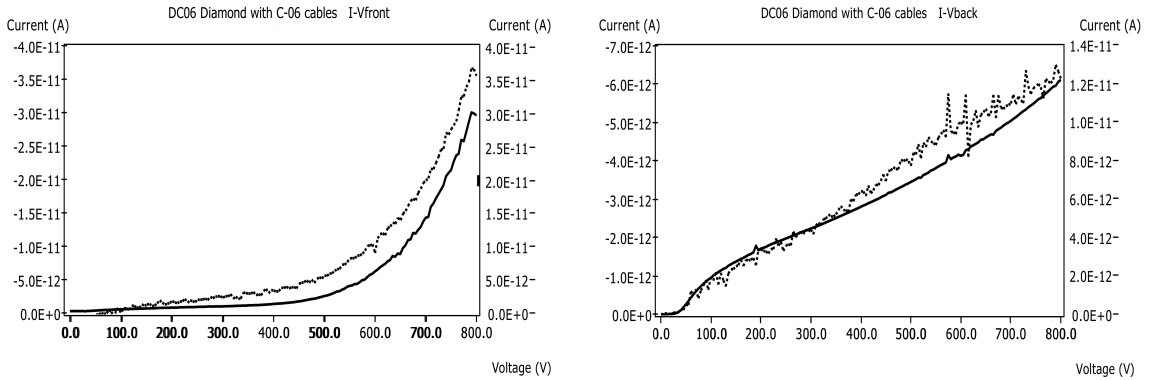


Figure 4.3: Current-voltage characteristics with voltage applied to the front (left panel) and to the back (right panel) diamond contacts. On the left panel the continuous line shows the current read on the back (left axis) while the dotted line shows the current read on the front (right axis). On the right panel front and back currents are swapped.

The dotted line in the left panel of Fig. 4.3, obtained with front polarization, shows the front current I_{front} , whose values are read on the right vertical axis. The left axis refers to the values for the back current I_{back} (continuous line). The two currents have opposite signs because conventionally currents going into the diamond are taken positive while outgoing currents are considered negative.

Typically, at 100 V, dark currents are of the order of 1 pA, while currents during irradiation are of the order of 1 nA. These values vary across sensors and type of irradiation. The three orders of magnitude between dark and irradiation currents enable to identify clearly the signal over the noise and to measure it accurately.

By biasing the front contact, front and back currents differ, I_{front} is higher than I_{back} . The front electrode collects both the current that passes through the diamond (stray current) and the leakage current through the package while the back electrode collects only the current flowing through the diamond. This way both leakage and stray currents can be estimated.

By biasing the front contact, a current between the thin bond wires and the package through the air may be generated, increasing the total output current of the sensor. However, by inverting the polarization, connecting the bond wires to ground, no large current changes are usually seen, suggesting that the bond-wire-generated current is negligible.

Repeating the same test with opposite polarization (right panel Fig. 4.3) shows a peculiar effect: the I-V characteristic is non-symmetric under polarization swap.

Differently from silicon devices, which feature a clear orientation due to different doping types, CVD diamonds are expected to be symmetric, which is not observed in our sensors.

The observed asymmetry may be ascribed to the crystal growth direction, which is the only known effect that breaks the front-back symmetry of the system. The current is higher on the contact to which the voltage is applied, due to the presence of parasite leakage currents.

4.2 Calibration sources

A first set of tests is aimed at the determination of the transport properties of electrons and holes, and of the charge collection efficiency of each diamond sensor. For these measurements a low-activity source of almost mono-energetic α particles is best suited, as the amount of ionization in diamond is well defined and spatially concentrated in a small region, allowing the study of electrical properties of each charge carrier independently.

Other measurements concern the stability of response in high fluxes of charged particles, and the determination of conversion factors between the measured currents from diamond detectors and the corresponding dose rates. For this purpose I use a β source with rather high activity, simulating the Belle II environment.

I use these two sources because of their complementary properties, studying each sensor response as a function of several source-detector parameters.

The properties of the two radioactive sources used for these tests are summarized below.

- The **^{241}Am alpha source** is based on the $^{241}_{95}\text{Am} \rightarrow ^{237}_{93}\text{Np} + \alpha + \gamma$ decay with a 5 kBq activity and a half-life of 432.2 years. The α energy spectrum shows five main peaks:

E_α (MeV)	5.388	5.442	5.485	5.511	5.544
\mathcal{B} (%)	1.6	13	84.5	0.22	0.34

Table 4.1: Energies and branching ratios of the five main components of the $^{241}_{95}\text{Am}$ α -particle spectrum.

The emitted photon comes from the Np nucleus transition from an excited to the fundamental energy state.

- The **^{90}Sr beta source** provides electrons from the chain of two subsequent decays $^{90}_{38}\text{Sr} \rightarrow ^{90}_{39}\text{Y} + e^- + \bar{\nu}_e$, $^{90}_{39}\text{Y} \rightarrow ^{90}_{40}\text{Zr} + e^- + \bar{\nu}_e$ with a 3.2 MBq activity. The first branch of the decay has a half-life of 28.8 years and a decay energy of 546 keV. The second branch 64 hours and 2282 keV. Figure 4.4 shows the electron energy spectrum for the $^{90}_{38}\text{Sr}$ β -decay.

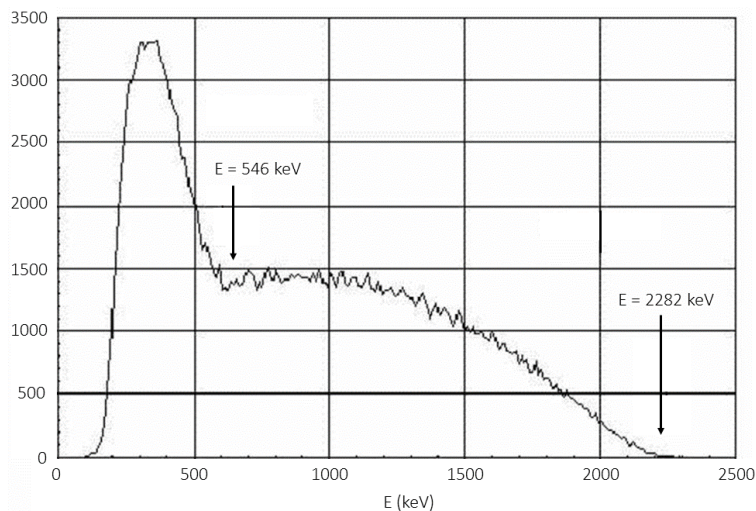


Figure 4.4: Electron energy spectrum for the $^{90}_{38}\text{Sr}$ β -decay.

Two structures are visible, one related to the strontium (Sr) decay into yttrium (Y) at lower energies and one related to yttrium (Y) decay into zirconium (Zr) at higher energies. The extension in energy of these two structures is limited by the available decay energy.

4.3 Characterization with α source

This section illustrates the technique, the simulation, the experimental setup and the results obtained with the diamond-detector α -source characterization. This characterization has the aim of finding eventual discrepancies between the predicted and the observed sensor behavior, tracing them back to charge carrier properties.

4.3.1 Transient current technique

The measurements performed with the α source are known in literature as transient current technique (TCT) [50]. A key feature is the 14 μm range of 5.5 MeV α particles entering the crystal, which is small compared to the 500 μm thickness of the sensor. Charge carriers are therefore created close to the surface of the sensor and only one type of carrier is collected by the front electrode. If the electrode is positively polarized, electrons are immediately collected, otherwise holes are captured. The opposite charge carrier drifts along the entire diamond bulk, inducing an electric signal on the back electrode, which is then amplified and collected.

This allows for studying the properties of electrons and holes separately, since only one carrier drifts along the whole bulk. For each sensor the measurement is repeated for both biasing polarities.

In an ideal crystal the signal shape as a function of time should be rectangular. The rise and fall times should be negligible since charge carriers are expected to be created and absorbed in less than 1 ns. Charge carriers are expected to drift with constant velocity because the electric field should be uniform. Thus, the bulk of the signal should be flat according to the Shockley-Ramo theorem [51], which relates the instantaneous current, induced in the external circuit by the drift of a point-like charge carrier, with the charge carrier velocity.

The main goals of this measurement are

- checking against possible deviations of the collected signal shape from the expected one, that could be correlated with defects or imperfections of the sensor;
- determining the drift velocity and carrier mobilities as functions of the bias voltage applied;
- obtaining parameters like the saturation velocity and low field mobility of the charge carriers;
- estimating the charge collection efficiency (CCE) as the ratio between the collected charge and the charge created inside the diamond bulk;
- estimating the average energy required to create an electron-hole pair.

The last two goals are achieved comparing experimental results with simulations.

4.3.2 Simulation

The almost mono-energetic α -particles from the radioactive source lose part of their energy in the material traversed before entering the active diamond volume. In order to estimate the average energy actually deposited in diamond to generate electron-hole pairs, I wrote a simulation of the source and sensor using Fluka, a particle physics Monte Carlo simulation package [52].

The core of the simulated system is sketched in Fig. 4.5: a 1 mm air layer separates the source from the sensor; I model the sensor with 3 metallic contact layers and the 500 μm thick diamond crystal (see Sec. 4.1); the active part of the source is simulated as a 0.5 mm radius disk. Since the $^{241}_{95}\text{Am}$ α decay is not implemented in Fluka, I approximate the α

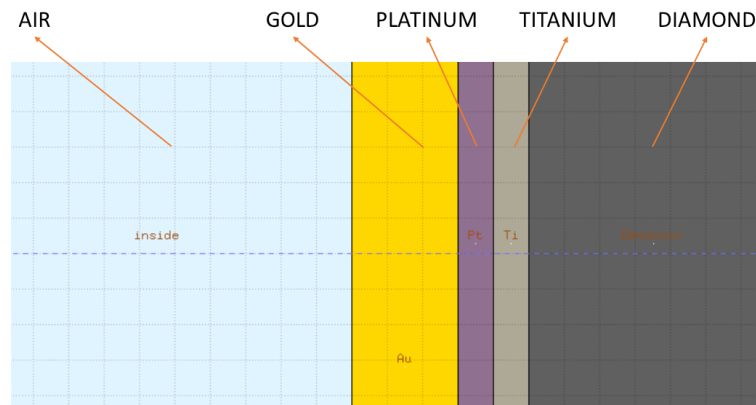


Figure 4.5: Representation of the layers that separate the sensor from the source. Starting from left: 1 mm thick air layer (light blue), 250 nm gold layer (yellow), 120 nm platinum layer (purple), 100 nm titanium layer (grey) and 500 μm diamond layer (brown).

energy spectrum with five narrow peaks centered at the corresponding values in the real spectrum. The reference frame is chosen so that the x, y axes are parallel to the sensor surface and the z axis is perpendicular.

For each of the five energy values in the spectrum, I generate five simulated data samples with 5×10^5 α particles in each run. I divide the detector volume within a depth of 100 μm into $200 \times 200 \times 500$ volumes (bins) along x, y and z respectively. For each bin, the center position and the energy deposited per unit volume is recorded. Figure 4.6 shows the results of the simulation. In the bottom-right panel the typical shape of a Bragg peak is visible.

Starting from the total energy loss of the α -particle, 94.8% is deposited in the diamond, 3.6% in the metallic contacts and 1.6% in the air. The energy deposited in the diamond by the α -particle weighted with the decay branching ratios is $E_{dia} = 5.17$ MeV.

This value is used in the following, in particular to determine the average energy required to generate an electron-hole pair.

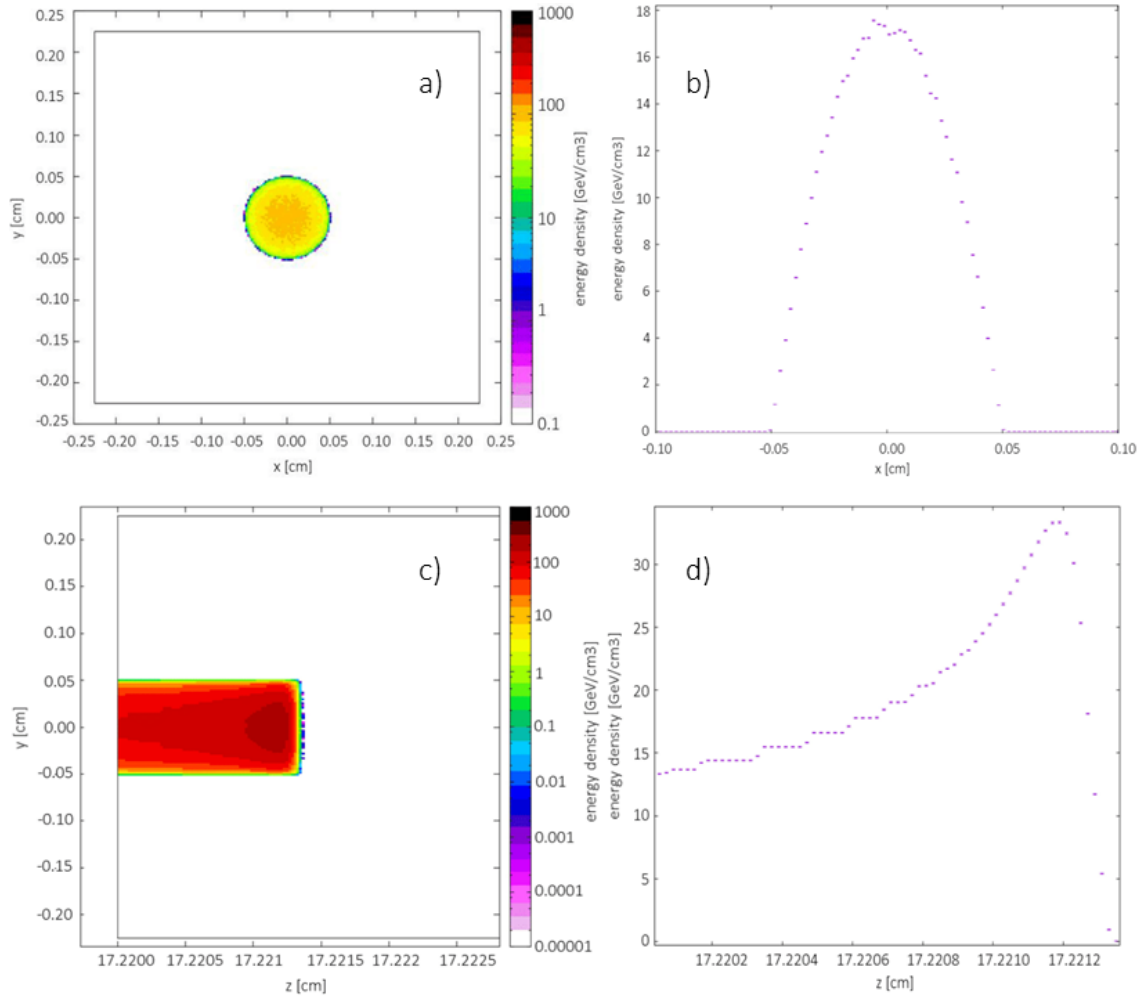


Figure 4.6: Results of the simulation: the initial α -particle energy is 5.485 MeV on average corresponding to the most probable energy value of the decay spectrum. a) Two-dimensional profile of the energy deposited per unit volume (color scale) in the detector on the x-y plane projection: the circular shape of the source is visible. b) One-dimensional profile obtained from the projection along the x axis of the histogram in a). c) Two-dimensional profile of the energy deposited per unit volume (color scale) in the detector on the y-z projection. d) One-dimensional distribution of the deposited energy along the z axis of the histogram in c).

4.3.3 Experimental setup

The detector characterization with the α source can be done with two different connection configurations: in the first one I connect the bias to one electrode and read the output current from the other. Figure 4.7 shows the experimental setup corresponding to this configuration.

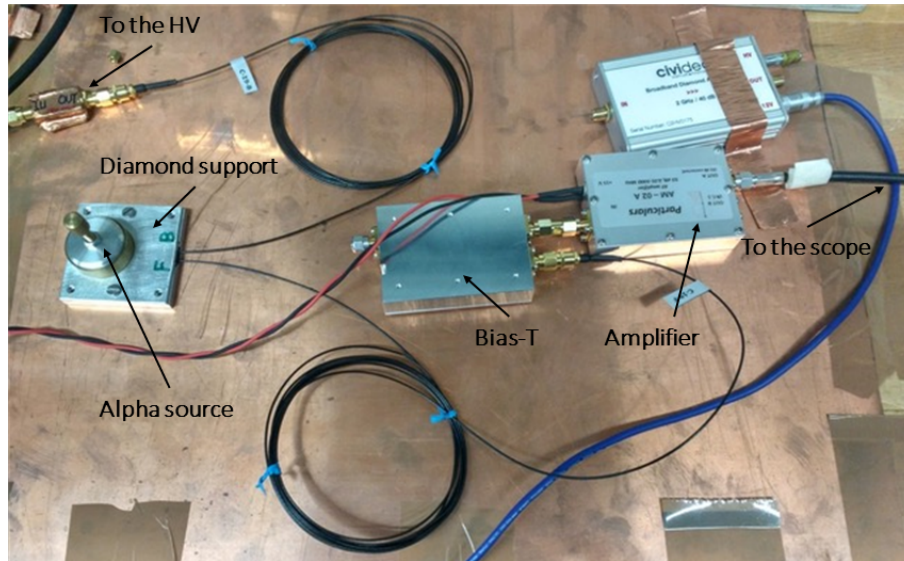


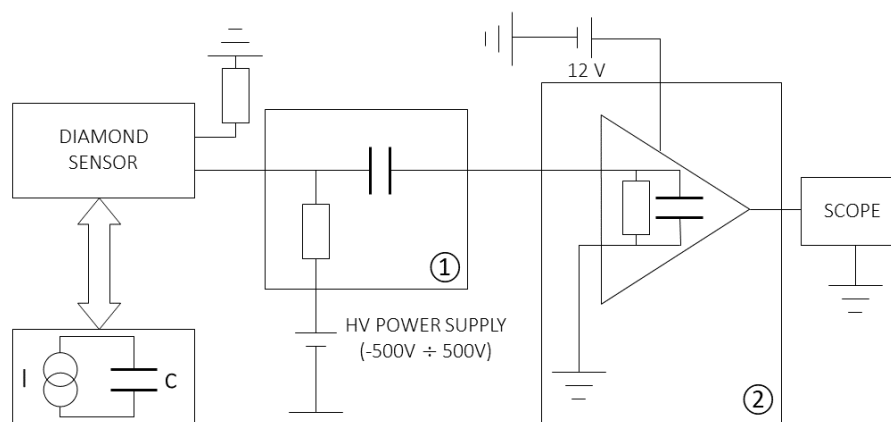
Figure 4.7: Experimental setup for detector characterization with α source.

In the second configuration I bias and read the output current on the same electrode, while terminating the other electrode with a $50\ \Omega$ terminator. Figure 4.8 shows a simplified electronics diagram corresponding to this second configuration. During the characterization with α source I use this second setup configuration that introduce less noise due to reflected signals.

The main components of the circuit, that are the same for the two configurations, are the following:

- the diamond sensor, represented as a capacitance C and a current source I . The charge generation represented by the current source is provided by the ionizing α -particles;
- a power supply [53] that provides voltages ranging from $-500\ \text{V}$ to $+500\ \text{V}$ to one contact of the diamond sensor; the other contact is connected to ground.
- a decoupling circuit [54] (labeled as 1 in Fig. 4.8) that enables the connection of high voltage to the readout side of the detector;
- a current amplifier [55] (labeled as 2 in Fig. 4.8) that amplifies the output current with a 53 dB gain and a bandwidth of 2 GHz.
- a digital oscilloscope [56], with a 3 GHz bandwidth that collects, display and store the electric signal at the output of the current amplifier.

The source and the diamond sensor are installed in an aluminum support that keeps 1 mm distance between them thus minimizing the α energy loss in air.

Figure 4.8: Schematic representation of the circuit used with the α source.

4.3.4 Data collection

For each biasing polarity, I set the trigger of the oscilloscope to a suitable value to select the signal above the noise and record the average taken over 1000 signals. Figure 4.9 shows two typical oscilloscope outputs. The horizontal and vertical divisions are set to 5 ns and 50 mV, respectively. The noise amplitude is usually less than 50 mV peak-to-peak. The measuring setup is very sensitive to other electrical devices powered near it. E.g., the system picks up the 50 Hz noise produced by the power line. The system is isolated to reduce the noise amplitude and the remaining noise is averaged out by taking the average of a thousand signals.

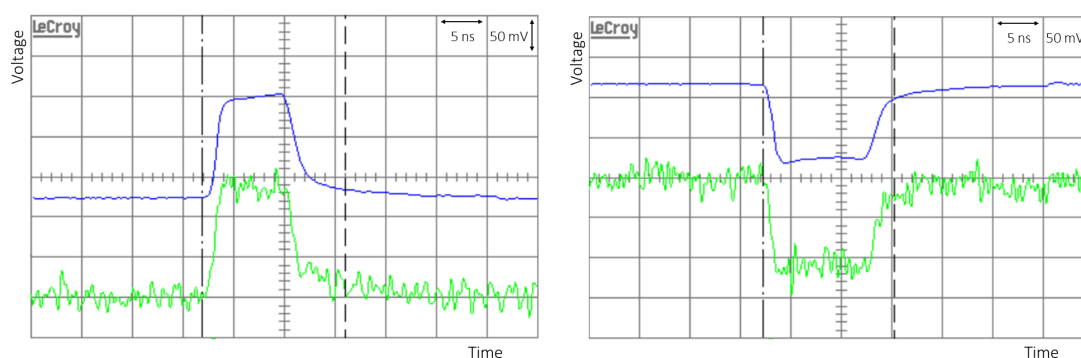


Figure 4.9: Average signals (blue) and single signals (green) taken with +300 V (left panel) and -300 V (right panel) polarizations of the diamond sensor.

Figure 4.10 represents the time development of the collected average signals as a function of the eight choices of biasing polarities applied. Since the back electrode is connected to ground, a positive voltage implies that the holes drift along the bulk while the electrons are immediately collected and vice-versa. The observed signals are not perfectly rectangular. They show finite rise and fall times and a non flat bulk.

The signal rise time is approximately constant for voltages higher than 100 V, suggesting that the rise time is dominated by the electronic time constants of the amplification and readout systems, which is independent from the applied bias.

The falling edge indicates the arrival of the charge carriers at the back electrode. The larger falling time at lower voltages might be related to the increase in diffusion width as the drift time increases. Under higher bias voltages, the electrode collects carriers faster,

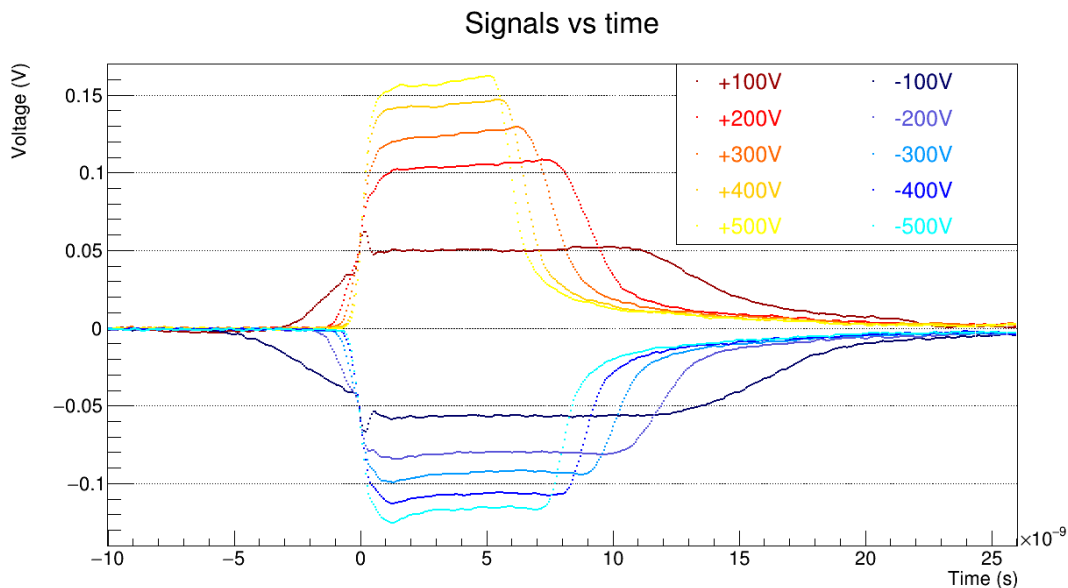


Figure 4.10: Time evolution of the signal induced by charge carriers as a function of the applied biasing polarity, listed in the legend.

limiting their diffusion in the bulk.

The non-flat signal core can be attributed to a charge density inside the diamond bulk. Assuming that this charge is uniformly distributed inside the bulk, it would create an electric field that varies the charge carrier velocity. Since the signals associated with holes show a positive slope, while the electron signal has a negative slope, the charge inside the diamond is positive. Such charge density could be generated inside the diamond bulk during the growth process, when impurities may remain trapped inside.

Figure 4.10 shows that the signal width shrinks as the applied voltage grows. This is due to the smaller time needed to extract the charge carriers from the bulk, resulting from the higher drift velocity as the electric field increases. Since the charge created by the impinging α particle is independent from the applied bias, as the signal width shrinks, its height increases. Assuming similar charge collection efficiency for each bias value, we expect the same amount of charge collected. Hence, the area under the average signals, which is proportional to the time-integral of the current, is expected to be constant, independently from the voltage applied.

In the analyses I exclude the data point corresponding to the bias voltage of $|V| = 100$ V ($E = 0.2$ V/ μm) when the signal is hardly distinguishable from noise.

4.3.5 Analysis of carrier mobilities

The aim of this analysis is to determine the charge-carrier drift properties as a function of the bias voltage applied.

I perform the analysis presented in this section over five diamond sensors, technically identified in Belle II as DC24, DC25, DC26, DC27 and DC28, and corresponding approximately to 1/4 of the final Belle II diamonds. The overall signals mirror the one presented in Fig. 4.10; however, each signal show some peculiarities. Signals occasionally show spikes at the rise edge, at the fall edge or at both edges, like the one in Fig. 4.11. Such spikes could be ascribed to electric field disuniformities, caused by charge accumulation along the surfaces that separate the diamond crystal from the metallic contacts. This is supported

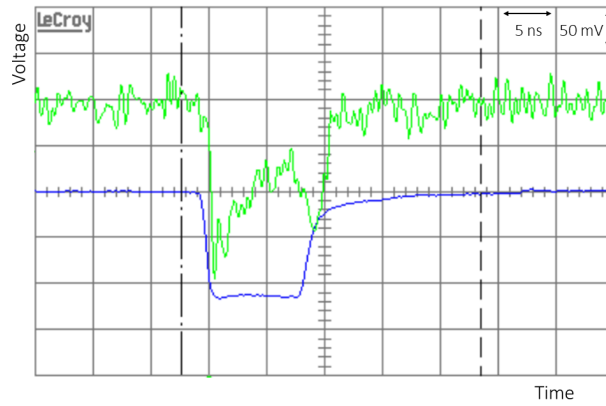


Figure 4.11: Example of a signal spikes during transition edges.

by the fact that spikes are observed only at the rise or at the fall of the signal suggesting that this behavior is related to phenomena occurring at the crystal boundaries.

Starting from the average signals in Fig. 4.10, I calculate the drift times as the FWHM of those signals. Knowing the crystal thickness ($500 \mu\text{m}$), I derive the drift velocity $v_{e,h}$, for electrons and holes separately. Assuming a constant electric field E generated by the external bias voltage, I calculate the charge carriers mobilities $\mu_{e,h}$ as

$$\mu_{e,h} = \frac{v_{e,h}}{E} . \quad (4.1)$$

Figure 4.12 shows the electron and hole mobilities as functions of the electric field. In the

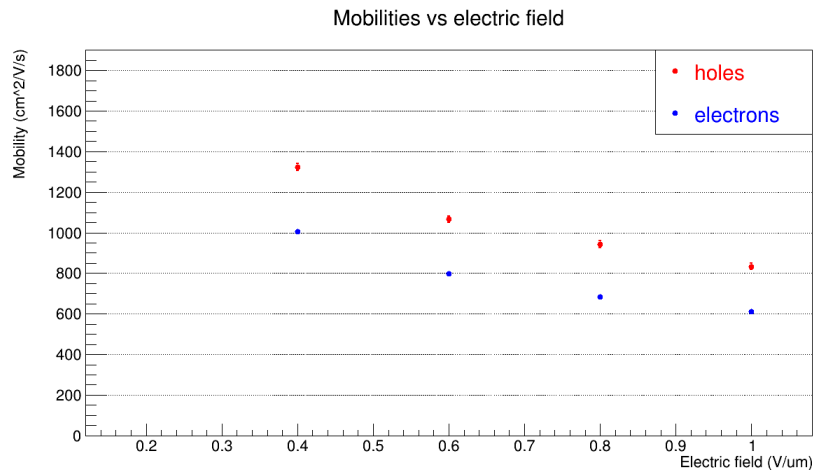


Figure 4.12: Electron and hole mobilities as functions of the electric field in the diamond bulk.

probed range of electric field, hole mobilities are consistently higher than the electron mobilities. See Ref. [57] for more details. Figure 4.12 shows that the mobility depends on the electric field, decreasing as the field strength increases for both electrons and holes. I investigate this dependence by studying the drift velocity as a function of the field (Fig. 4.13). See Ref. [58] for more details.

I fit the carrier drift velocities $v_d(E)$ in Fig. 4.13 using the following empirical expres-

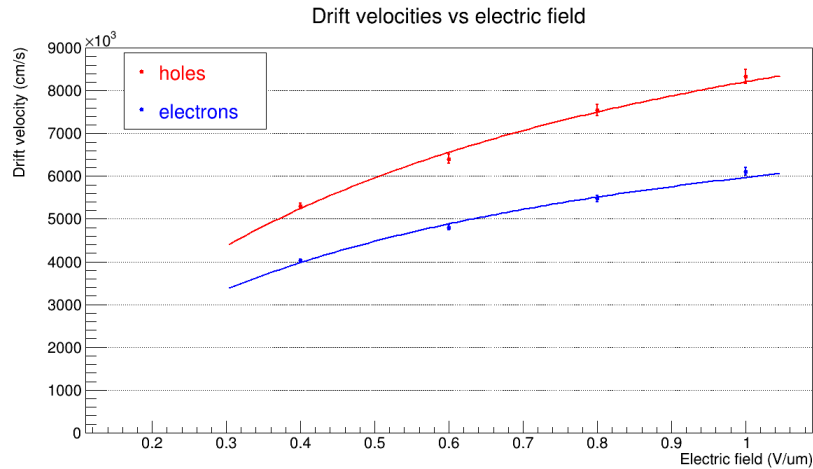


Figure 4.13: Electron and hole drift velocities as functions of the electric field in the diamond bulk with fits based on Eq. (4.2) overlaid.

sion [50], for both electrons and holes

$$v_d(E) = \frac{\mu_0 E}{1 + \frac{\mu_0 E}{v_{sat}}} \quad (4.2)$$

The fit determines the zero-field mobility μ_0 , which is the mobility at low field, when the denominator in Eq. (4.2) can be approximated to one. I also obtain the saturation drift velocity v_{sat} , which is the carrier velocity under intense fields, when the denominator in Eq. (4.2) can be approximated with the second term only. The estimated parameter values for the tested sensors are listed in Table 4.2.

Sensor ID	μ_0^h ($10^3 \text{cm}^2/\text{Vs}$)	μ_0^e ($10^3 \text{cm}^2/\text{Vs}$)	v_{sat}^h (10^7cm/s)	v_{sat}^e (10^6cm/s)
DC24	2.18 ± 0.10	1.80 ± 0.07	1.32 ± 0.06	8.95 ± 0.30
DC25	1.84 ± 0.07	2.69 ± 0.20	1.27 ± 0.06	7.12 ± 0.26
DC26	1.98 ± 0.08	1.67 ± 0.06	1.21 ± 0.05	7.93 ± 0.23
DC27	2.04 ± 0.09	1.80 ± 0.07	1.22 ± 0.05	7.75 ± 0.22
DC28	1.78 ± 0.07	1.72 ± 0.06	1.35 ± 0.07	8.02 ± 0.24

Table 4.2: Zero-field mobility μ_0 and saturation drift velocity v_{sat} parameters obtained by fitting the drift velocities in Fig. 4.13.

Except for DC25, which shows some peculiarities such as a non rectangular signal and unstable output, the hole zero-field mobilities are higher than the electron mobilities. The hole saturation velocities are higher than the electron ones too (Table 4.3).

$\bar{\mu}_0^h$ ($10^3 \text{ cm}^2/\text{Vs}$)	$\bar{\mu}_0^e$ ($10^3 \text{ cm}^2/\text{Vs}$)	\bar{v}_{sat}^h (10^7 cm/s)	\bar{v}_{sat}^e (10^6 cm/s)
2.00 ± 0.17	1.75 ± 0.06	1.27 ± 0.06	7.95 ± 0.66

Table 4.3: Average zero-field mobility μ_0 and saturation drift velocity v_{sat} parameters obtained from the detectors analyzed, excluding DC25 detector.

4.3.6 Analysis of charge-collection efficiency

An efficient charge-collection is an essential requirement for the detector to have the highest possible ratio between output signal and noise.

In order to estimate the charge-collection efficiency I calculate the collected charge from the average signals in Fig. 4.10. Given the area A under the signal, expressed in V·s, the coupling impedance $R = 50 \Omega$ and the amplifier gain $G = 53 \text{ dB}$, the collected charge Q_{coll} is given by

$$Q_{coll} = \frac{A}{R \cdot 10^{G/20}} \cdot \quad (4.3)$$

The collected charges are represented in Fig. 4.14 as functions of the applied electric field for both electrons and holes.

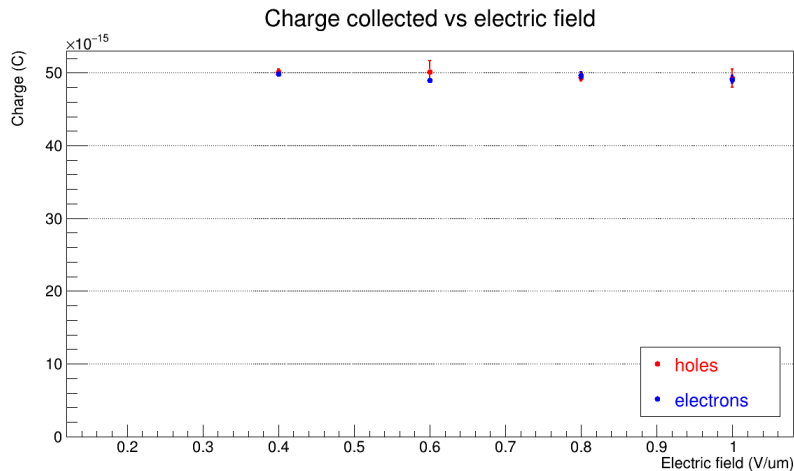


Figure 4.14: Collected charges for hole and electron carriers as functions of the electric field in the diamond bulk. Charge-collection saturation is observed with an electric field greater than $0.4 \text{ V}/\mu\text{m}$.

For applied voltages higher than 200 V , the collected charge saturates to an approximately constant value $Q_{coll} = (50.91 \pm 1.20) \text{ fC}$. The fractional difference between the charge collected evaluated from electrons and holes does not exceed 2.5%. I calculate the collected charge values from a fit with a constant of the charge profile at high voltages applied, where the charge saturates.

Chemical impurities and crystal defects, which can be created during the crystal growth or after intense irradiation, introduce position-localized energy levels inside the band gap. As the charge carriers drift along the diamond bulk, they can be trapped in such levels, decreasing the current readout at the back electrode. I treat charge trapping using the Shockley-Hall-Read model [59], which states that intermediate energy levels inside the band gap act as generation and recombination centers for carriers.

We define $\tau_{e,h}$ as the charge-trapping-lifetime for electrons and holes, that is the mean time for a charge carrier to become trapped. Its inverse $1/\tau_{e,h}$ corresponds to the probability per unit of time for a charge carrier to be trapped. The current read at the back electrode as a function of time can be expressed as

$$i_{e,h}(t) = i_0 \cdot e^{-t/\tau_{e,h}} . \quad (4.4)$$

This current is equal to the generated current modulated by the trapping probability, given by the exponential. I obtain the charge collected $Q_{e,h}$ by integrating the current pulse between the rise (t_r) and fall (t_f) times

$$Q_{e,h}(V) = \int_{t_r}^{t_f} i_{e,h}(V,t) dt , \quad (4.5)$$

where the dependence on the voltage applied is introduced.

Expanding Eq. (4.4) up to the second order and integrating it, the collected charge is expressed as

$$\frac{Q_{e,h}^0 - Q_{e,h}(V)}{Q_{e,h}^0} \approx \frac{d}{2\tau_{e,h} v_{e,h}} , \quad (4.6)$$

where $Q_{e,h}^0$ is the charge in absence of trapping, d the crystal thickness, and $v_{e,h}$ the drift velocity.

Starting from Eq. (4.6) Fig. 4.15 shows the collected charge as a function of the inverse drift velocity. Since saturation is achieved already at 200 V, I cannot fit the data with

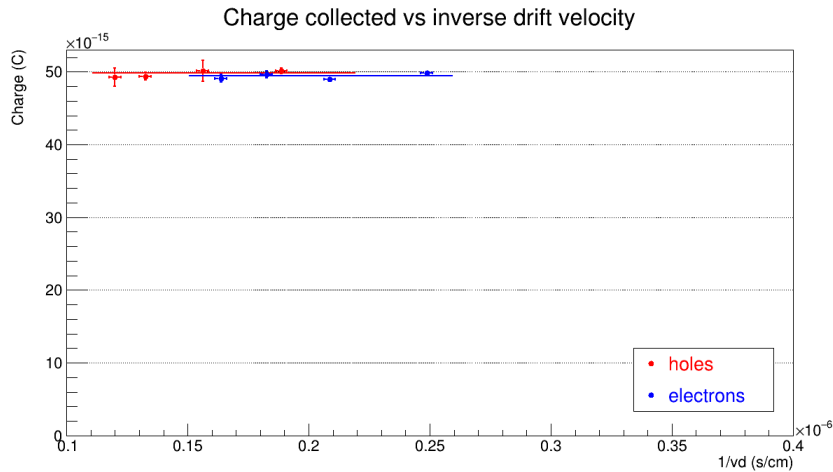


Figure 4.15: Collected charge as a function of the inverse drift velocity. Solid lines are the horizontal fits done separately for electrons and holes.

Eq. (4.6) to obtain the charge generated $Q_{e,h}^0$ and the trapping time $\tau_{e,h}$. Significant noise does not allow to perform measurements at lower voltages, where the collected charge is expected to differ more from the generated charge.

Starting from the collected charge, I calculate the charge collection efficiency (CCE). A charge saturation mechanism at bias voltages higher than 200 V seems a reasonable explanation for the behavior of the collected charge as a function of the applied voltage. This implies that the charge is completely collected from the diamond bulk and so the CCE is approximately 100%.

On the other hand, I calculate the CCE as the ratio between the collected charge and the generated charge. I obtain the charge generated from the energy deposited, calculated through the Fluka simulation and assuming $\epsilon = 13$ eV as the energy needed to create a pair of charge carriers [60]. The assumption on ϵ leads to a CCE smaller than one. However, the observed efficiency saturation suggests to assume 100% CCE.

The values reported in literature for ϵ range from 12 eV to 17 eV. Assuming fully efficient charge extraction from the diamond bulk, and knowing the average energy deposited by α particles, I evaluate the energy needed to create an electron-hole pair (Table 4.4).

Sensor ID	ϵ_h (eV)	ϵ_e (eV)
DC24	16.71 ± 0.10	16.84 ± 0.05
DC25	16.23 ± 0.28	16.51 ± 0.12
DC26	16.45 ± 0.04	16.87 ± 0.07
DC27	15.88 ± 0.05	15.75 ± 0.07
DC28	16.31 ± 0.08	16.09 ± 0.05

Table 4.4: Estimated electron-hole creation energies for the five sensors tested.

The mean ϵ parameters evaluated from electrons or holes are compatible across sensors, as expected. Starting from the ten energy values listed, I derive an average value of

$$\epsilon = (16.36 \pm 0.38) \text{ eV} . \quad (4.7)$$

The discrepancy between the measured ϵ value and the one usually reported in literature can be ascribed both to carrier drift dynamics and readout electronics. In the first case, since the induced signals are basically flat and a charge saturation as a function of the applied bias voltage is achieved, the discrepancy between ϵ values can be related to a partial recombination of electrons and holes. The compact and dense charge cloud created by the impinging α particle facilitates the carrier recombination.

On the other hand such a discrepancy can be due to a non-nominal value of the amplifier gain. The 53 dB value is reported in the amplifier data sheet, however a difference in the amplifier gain would introduce a systematic error in the evaluation of the collected charge, leading to a different value of ϵ .

The above hypotheses are qualitative. A deeper study of the charge-carrier properties and an accurate calibration of the amplifier circuit will help in finding the origin of such a discrepancy.

4.4 Characterization with β source

I perform measurements with the β source as a function of time, bias voltage, and source-detector distance. The β source electrons travel throughout the diamond bulk, releasing energy. This emulates the realistic operation conditions in Belle II, where particles associated with beam losses might travel through the diamond crystal.

- **Stability measurement**, this measurement is intended to verify whether the output current is stable as the radiation flux absorbed by the detector is constant. This procedure consists in irradiating the detector with a constant electron flux, while verifying whether the output current is stable in time. The distance between the source and the sensor is fixed, as is the bias voltage.
- **IV characteristic**, this measurement is intended to verify whether the detector reaches a saturated current value as the voltage increases, as expected from an ideal sensor. The source-detector distance is fixed and the current is measured as the bias voltage is changed.
- **Calibration**, this measurement is intended to find the relation between output current and absorbed dose rate. The source-detector distance is changed, while keeping the bias voltage constant. Changes in the output current are correlated to the electron flux changes, as the distance varies.

Figure 4.16 shows the experimental setup used for the detector characterization with the β source. The detector and the source are placed inside a $(37 \times 22 \times 22)$ cm³ Plexiglas

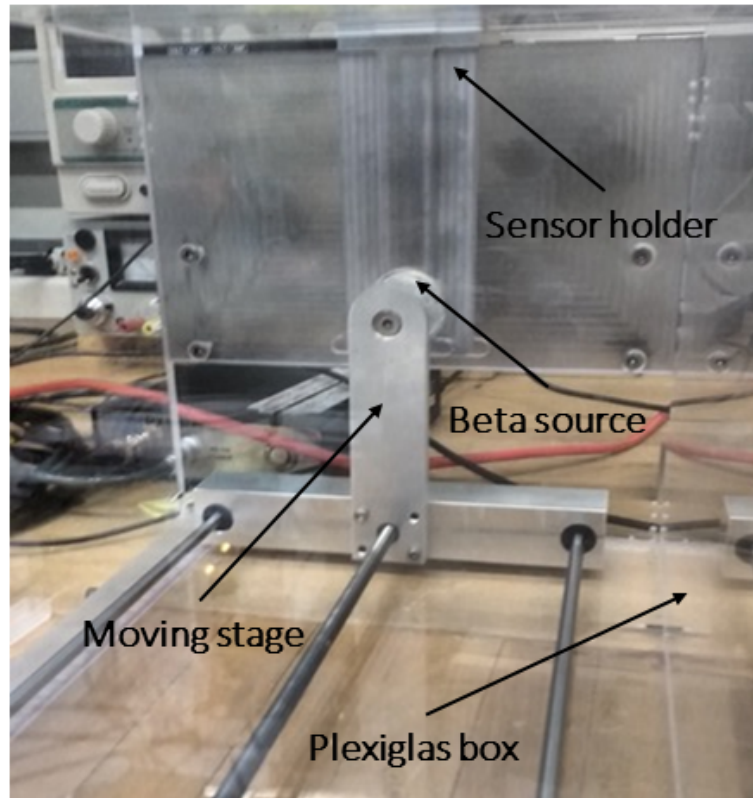


Figure 4.16: Experimental setup for detector characterization with the the β source.

(polymethyl methacrylate) box. 1-cm-thick walls absorb completely the radiation emitted

by the source. The diamond sensor package is constrained to an aluminum support to keep it in the desired position. The source is connected to a slider that can be moved, varying the distance between the source and the detector in an automatized and controlled way.

I apply a bias voltage to the detector using a power supply. The generated current is read via a picoamperometer. The analog signal is converted by the same instrument to a digital 24-bit value stored on a disk.

4.4.1 Stability measurement

Stability in time is a key characteristic for a radiation monitor. When the radiation flux is constant the detector response has to be constant. Otherwise, the dose rates absorbed by the sensor cannot be inferred unambiguously, from the output current.

I place the source at 2.0 mm from the diamond sensor, continuously reading the output current for up to 2-3 days. A current measurement is recorded every 10 seconds, averaging over 13 kHz data samples.

Different biasing polarities result in different output current profiles. Figure 4.17 shows a typical case. With front-side polarization, the DC24 sensor shows a stable response,

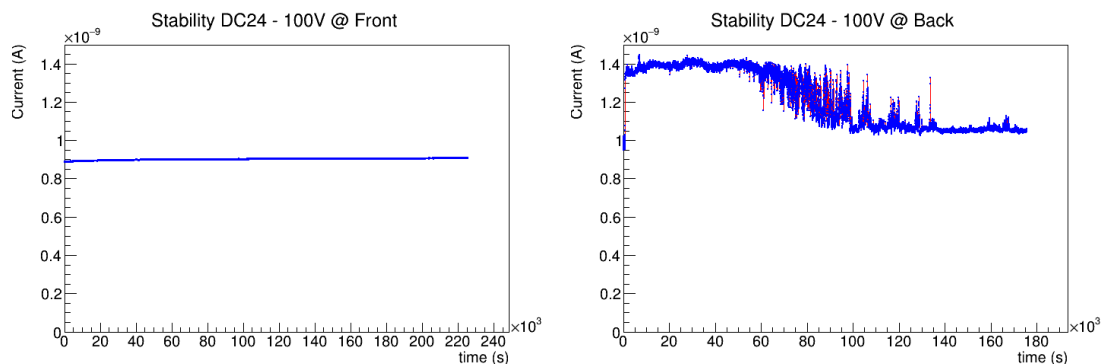


Figure 4.17: Current as a function of time for the DC24 diamond with +100 V applied to the front side (left panel) and back side (right panel).

with current fluctuations within 3%. With back-side polarization, the signal is unstable. After the first 16 hours with output current constant at 1.4 nA, an unstable regime rich in current spikes kicks in. After that a lower baseline current is reached (1.05 nA) but spikes still happen. With back-side polarization, response fluctuations exceed 50%.

Based on these tests I choose the front-side polarization for the DC24 as default configuration for Belle II operation. After analyzing the stability measurements of the other diamond detectors, I decided to use DC25, DC26 and DC28 with back-side bias and DC27, as DC24, with front-side bias.

It is impractical to expose diamond detectors to a constant particle flux for stability measurements within a time interval comparable to Belle II data taking (10 years). Three day tests are intended to select the best polarization side within a limited time range.

By polarizing a sensor on its best side, a flat current profile is expected in an ideal crystal. However, occasionally I observe varying-current transients before the current converges to a stable value. Figure 4.18 shows an example of transient current.

Such current transient is attributed to the presence of trapping centers in the energy gap. As the diamond is irradiated, these energy levels trap electrons and holes, decreasing the output current. As the time passes the traps are filled and the current rises, achieving a stable value.

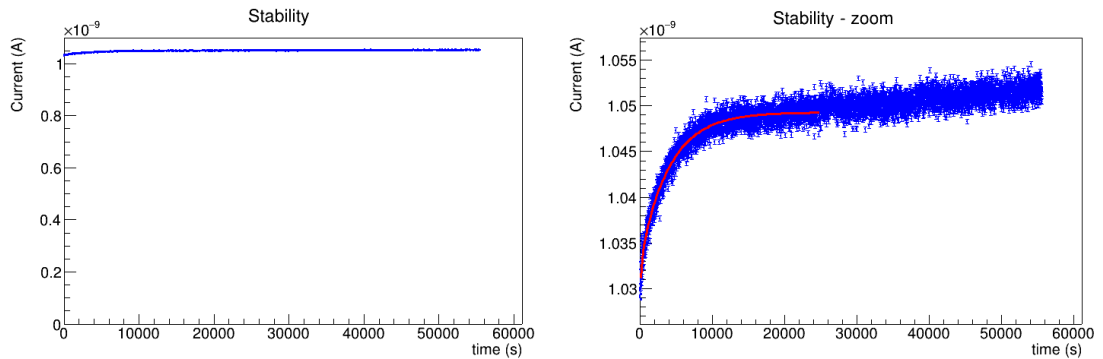


Figure 4.18: Current as a function of time (left panel) for diamond DC08 and magnification of the current transient area with an exponential fit overlaid.

I fit the transient profile to extract information about traps (Fig. 4.18). Assuming a simplified model in which traps can be close to either the band gap edges (shallow) or center (deep), the function used to fit the current profile is

$$I = I_0(1 - w_s e^{-t/\tau_s} - w_d e^{-t/\tau_d}) , \quad (4.8)$$

where I_0 is the asymptotic current value, w_s and w_d are the proportions of shallow and deep traps, respectively, and τ_s and τ_d are the corresponding time constants.

The fit results are in Table 4.5.

Parameter	Value
I_0	1.05 nA
w_s	$(3.10 \pm 0.09) \times 10^{-3}$
τ_s	355 ± 23 s
w_d	$(15.53 \pm 0.06) \times 10^{-3}$
τ_d	4070 ± 20 s

Table 4.5: Fit results of the current transient during a stability measurement on diamond DC08. Where not indicated, uncertainties are negligible.

Stability key results

Stability measurements suggest that typically each sensor has a more stable polarization side that has to be determined to operate the detector in the best way. In addition, current transient profiles offer information about trap properties inside the diamond bulk.

4.4.2 I-V characteristic

I perform I-V measurements to study current-response deviations from the expected behavior of an ideal diamond sensor, where current saturation is achieved and no hysteresis loops are expected.

I measure the current-voltage curve of each sensor with the same instruments used for the stability measurement. The determination of the I-V characteristics consists in irradiating the detector with the β source from a distance of 2.0 mm and read the output

current while varying the bias from 0 to -500 V and from 0 to +500 V in 20 V steps between 0 and 100 V and in 50 V steps up to 500 V. I perform the measurement in a loop, measuring the current at each voltage point twice in order to verify if hysteresis is present. Hysteresis indicates a "memory" phenomenon in which the current measured at a given voltage depends on the previous history of applied voltages.

Two typical IV-outputs are represented in Fig. 4.19 and 4.20.

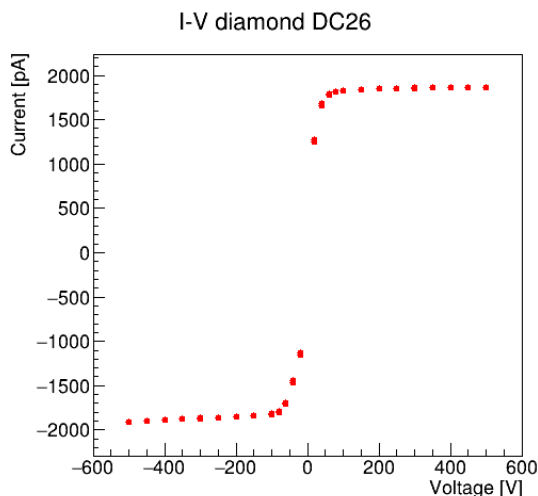


Figure 4.19: DC26 IV characteristic.

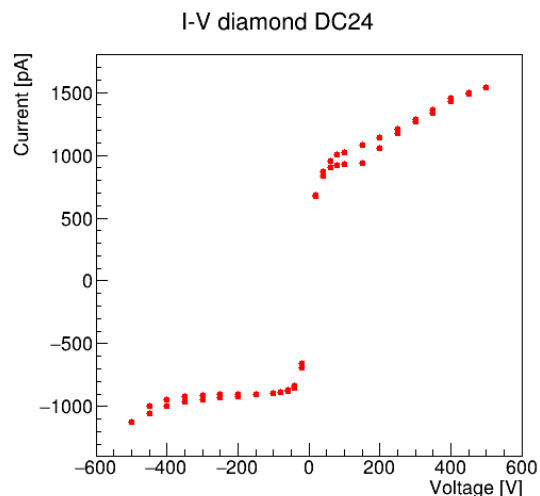


Figure 4.20: DC24 IV characteristic.

Figure 4.19 shows the expected behavior from an ideal sensor: for both negative and positive bias voltages, current saturation is achieved. For voltages higher than a certain threshold (~ 100 V), the full collection of charge generated inside the detector is likely to be reached and higher voltages do not lead to higher currents. No hysteresis is present: the current is a function of the applied voltage only.

Figure 4.20 shows a different current profile. For both positive and negative bias voltages, hysteresis loops are present. Such loops might be due to energy levels in the band gap that act as capture and emission centers, highing or decreasing the output current as they trap or release charge carriers [61].

Another difference between Fig. 4.19 and Fig 4.20 is the lack of current saturation in Fig. 4.20. This effect is most likely due to charge injection from the metallic electrodes to the diamond bulk.

The metallic contacts are deposited on the crystal surfaces to extract the charge inside. These contacts can be either blocking or injecting. In the first case the contacts prevent charge injection in the diamond bulk. This is due to a potential barrier grown between the contact and the bulk. In the second case charge injection occurs. The contact has a smaller impedance compared to the series impedance of the semiconductor bulk. The free carrier density in the vicinity of the contact is higher than that in the bulk of the semiconductor. So the contact may inject carriers in the bulk itself [59].

Considering the diamond bulk being irradiated, we define f as the charge generation rate per unit volume and τ the charge carrier recombination lifetime. From the continuity equation of free electrons in stationary conditions and uniform carrier generation it follows that

$$n = f\tau, \quad (4.9)$$

where n is the electron concentration excess.

The excess of free electrons is given by

$$N = nA\Delta x = fA\Delta x\tau = F\tau , \quad (4.10)$$

where A and Δx are the area of the diamond bulk and its thickness, respectively and $F = fA\Delta x$ is the total generation rate. The photo-current is given by

$$I = \frac{dq}{dt} = neAv_d , \quad (4.11)$$

where the drift velocity is $v_d = \frac{\Delta x}{T_r}$. T_r is the transit time from the cathode to the anode. Consequently the photo-current is written as

$$I = \frac{Ne}{T_r} = Fe\frac{\tau}{T_r} = eFG , \quad (4.12)$$

where the ratio between the recombination time and the transit time is defined as photo-conductive gain G . In blocking contacts, G never exceeds one, while in injecting contacts it can be greater than one.

If the time needed to drift along the entire diamond bulk is less than the charge recombination lifetime, the photo-conductive gain exceeds one. The output current is no longer produced only by the impinging radiation, but contact injection also contributes.

I-V curves enable to quantify the current injected by the non blocking contacts. On the other hand, hysteresis loops indicate trap levels inside the energy band gap. I-V measurements show the impact of these levels on the electric properties of the sensors.

I-V key results

A common finding is that each sensor has its own peculiar properties, involving or not hysteresis loops and current saturation. When reached, the saturation current differs from one sensor to another.

4.4.3 Calibration

In calibration measurements the sensor is biased either on the front or back side at 100 V. The output current is measured as a function of the source distance.

The main goal of the calibration is to investigate the relation between the current read and the dose rate absorbed, which is the quantity that has to be ultimately evaluated in Belle II.

The derivation of this relation depends on several assumptions.

- The solid angle seen by the source on the detector as a function of the distance is written analytically in Eq. (4.14) assuming a point-like source.
- The relation between the solid angle and the flux of β particles hitting detector is linear, assuming isotropic emission.
- The dose rate absorbed by the sensor has a linear dependence on the particle flux. This relation relies on the hypothesis that the energy lost by impinging particles in air is negligible.

Under these conditions, the relation between the current signal and the dose rate absorbed is expected to be linear. Figure 4.21 sketches the logical path and assumptions listed above. Before calibrating a detector, I measure the current offset by placing the source at 55 mm from the detector and covering it with a copper shield. The shielded detector does not

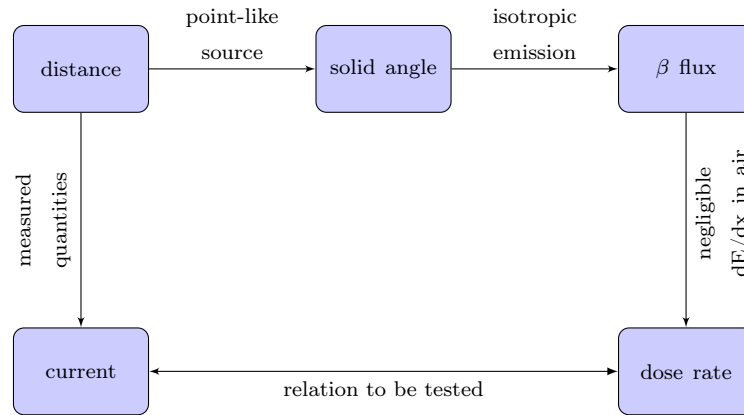


Figure 4.21: Sketch of the assumption associated with the calibration measurement.

receive any β particle. The corresponding current value is an offset I subtract from the subsequent measurement results.

During calibration I measure the output current for detector-source distances between 2 mm and 50 mm. At each distance, the current is measured for two minutes with a sampling frequency of roughly 13 kHz. Each sensor is subjected to four calibration measurements: varying the polarization side (front or back) and the movement direction (from 2 mm to 50 mm or vice-versa).

Figure 4.22 shows a typical calibration output. The output current is displayed as a function of the source distance. I fit the current profile with two functions. The first one

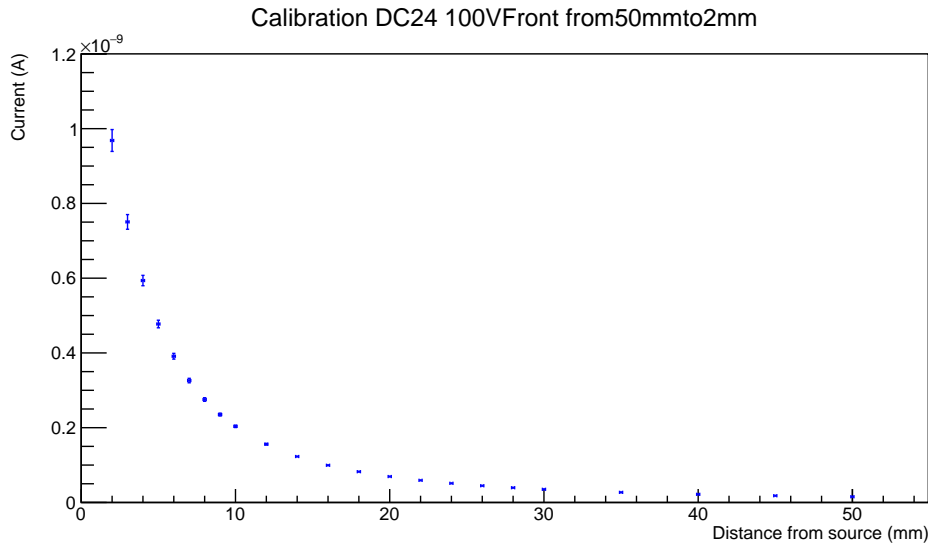


Figure 4.22: Current as a function of the source-detector distance. The DC24 sensor is polarized on the front electrode and the source is moved from 50 mm to 2 mm.

is written in Eq. (4.13), where the current depends on the inverse square distance r ,

$$I = \frac{A}{(r + B)^2} + C \quad (4.13)$$

where A , B and C are the normalization, the position offset, and the current offset respectively. I derive the values of the parameters by fitting the current profile.

I obtain the second function by an analytical calculation of the solid angle subtended by the diamond sensor. Assuming a point-like source and describing the detector as a square of side l , the solid angle Ω as a function of the distance r is given by

$$\Omega = 4 \arctan \left(\frac{l^2}{2r\sqrt{4r^2 + 2l^2}} \right). \quad (4.14)$$

Equation (4.14) is derived in Section 4.4.3.1.

Given the solid angle, the output current is parametrized as

$$I = I_0 + 4G \arctan \left(\frac{l^2}{2(r - r_0)\sqrt{4(r - r_0)^2 + 2l^2}} \right). \quad (4.15)$$

I_0 , G and r_0 are the current offset, the gain and the distance offset respectively.

4.4.3.1 Solid angle calculation

In the previous section, Eq. (4.14) is introduced to fit the current profile as a function of the distance. That formula can be derived as follows.

We consider a point-like source at the origin of a three-dimensional Cartesian reference system. The diamond sensor is approximated as a square of side l , parallel to the xz plane and centered on the y axis at a distance r from the source, as in Fig. 4.23.

We consider an infinitesimal element $dS = dx \cdot dz$ on the sensor surface and the vector

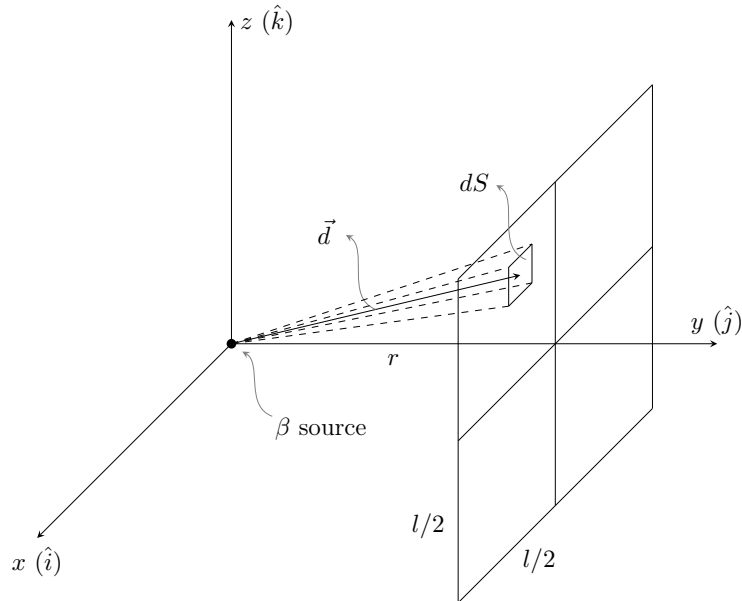


Figure 4.23: Sketch of the geometrical layout.

$\vec{d} = (x_0, r, z_0)$ that originates from the source and points to the center of the surface element.

As a vector, the surface element is expressed as

$$d\vec{S} = dx dz \hat{j}, \quad (4.16)$$

while the versor \hat{d} associated to \vec{d} is

$$\hat{d} = \frac{x_0 \hat{i} + r \hat{j} + z_0 \hat{k}}{\sqrt{x_0^2 + r^2 + z_0^2}}. \quad (4.17)$$

The corresponding infinitesimal solid angle $d\Omega$ seen by the source over the detector and included by the dashed lines in Fig. 4.23 is

$$d\Omega = \frac{\vec{dS} \cdot \hat{d}}{d^2} = \frac{r dx dz}{(x_0^2 + r^2 + z_0^2)^{3/2}}. \quad (4.18)$$

By dividing the sensor surface into four squares of side $l/2$, the total solid angle Ω seen by the source over the detector is given by the integral

$$\Omega = 4 \int_0^{l/2} dz \int_0^{l/2} \frac{r dx}{(x_0^2 + r^2 + z_0^2)^{3/2}}. \quad (4.19)$$

Since

$$\int \frac{dx}{(x^2 + a)^{3/2}} = \frac{x}{a\sqrt{a + x^2}} + C, \quad (4.20)$$

where a and C are constants, the integral is reduced to

$$\Omega = 2rl \int_0^{l/2} \frac{dz}{(r^2 + z^2)\sqrt{(r^2 + z^2) + \frac{l^2}{4}}}. \quad (4.21)$$

The generic integral

$$\int \frac{dx}{(x^2 + a)\sqrt{x^2 + b}} \quad (4.22)$$

with a and b constants is solved using the following substitutions:

- $x = \sqrt{b} \tan u$ that leads to $\int \frac{\cos u du}{(b-a) \sin^2 u + a}$
- $v = \sin u$ that leads to $\int \frac{dv}{(b-a)v^2 + a}$
- $w = \sqrt{\frac{b-a}{a}} v$ that leads to $\int \frac{1}{\sqrt{a(b-a)} w^2 + 1} dw = \frac{1}{\sqrt{a(b-a)}} \arctan \sqrt{\frac{b-a}{a}} \frac{x}{\sqrt{x^2 + b}} + C$

The last step follows from $\sin(\arctan(x)) = \frac{x}{\sqrt{x^2 + 1}}$ and redoing the substitutions in the opposite direction, to obtain a function of x . By inserting back the quantities r and l instead of the generic constants a and b , the solid angle Ω is obtained

$$\Omega = 4 \arctan \left(\frac{l^2}{2r\sqrt{4r^2 + 2l^2}} \right). \quad (4.23)$$

Under the assumptions listed in the previous section, Eq. (4.23) establishes the relation between the source-detector distance and the dose rate absorbed by the diamond sensor. Fitting the current profile as a function of the distance with Eq. (4.23) allows to test the linearity relation between absorbed dose rate and output current.

4.4.3.2 Generic simulation

In order to verify the analytic calculation of the solid angle I realize a Monte Carlo simulation. In addition, the simulation allows to introduce realistic departures from the ideal model of the system, that cannot be treated straightforwardly otherwise.

Figure 4.24 compares the two fitting functions. $r^{-2}(x)$ is proportional to the inverse of the square distance, while $\Omega(x)$ is based on the solid angle integral.

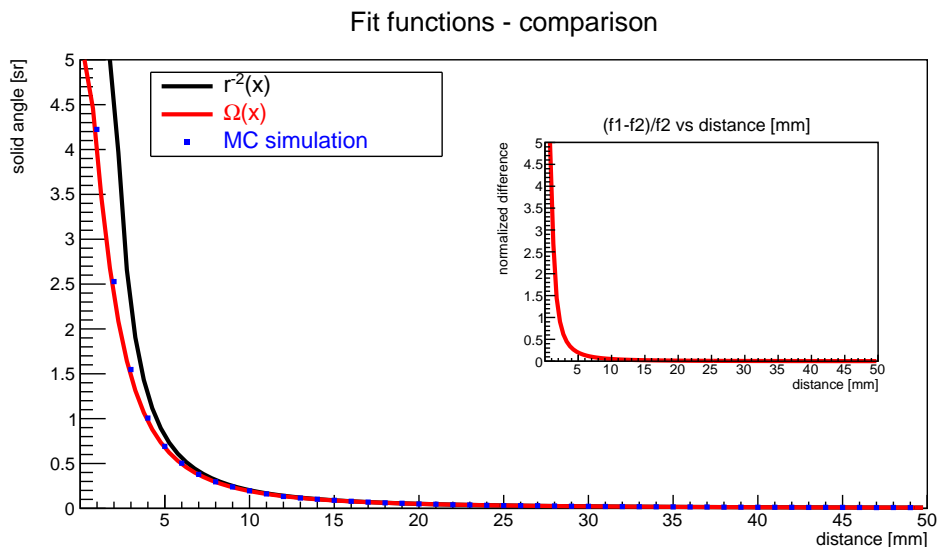


Figure 4.24: Comparison between the two fit functions. The blue points are the result of the simulation for the estimate of the solid angle. The box plot shows the normalized difference between the two fit functions.

The divergence of the first fit function as the distance approaches zero is the main difference between the two expressions. This is highlighted in the inset panel of Fig. 4.24 where the normalized difference between the two is represented. The difference between the two gets larger as the source-detector distance decreases as expected. Figure 4.24 shows also the result of a Monte Carlo simulation (blue points). I perform the simulation by generating particles isotropically at the origin of a three dimensional Cartesian reference frame and counting which fraction cross the detector. I repeat this procedure for the same set of distances measured during calibrations.

The observed fraction is an estimate of the solid angle seen by the source over the detector. The relative accuracy on which the solid angle is determined is $\sigma_{\Omega}/\Omega = 1/\sqrt{N}$, where N is the number of particles that hit the detector. For each distance, 10^6 particles are generated. The solid angle estimate coincides with the analytic integral fit function (Fig. 4.24).

Figure 4.25 presents a comparison between the simulation and other four analogous simulations where an offset in the xy plane, parallel to the detector surface, is added. The detector is not centered with respect to the source anymore. I add positive and negative shifts of 0.1 mm to the xy-detector position. These offsets take into account the possible misalignment of the detector while fixing it in the support before the measurement.

The results of the five simulations are compatible. The inset panels of Fig. 4.25 show that the normalized difference between simulations with and without offset is centered at zero. The increased dispersion along the line centered in zero as the distance increases is due to the smaller number of particles that hit the detector, resulting in a larger statistical uncertainty.

Figure 4.26 shows the comparison between two simulations, where I account for finite physical dimensions of the source. I model the active part of the β source as a 0.5 mm radius sphere. The origin of the decay electron is generated with a uniform distribution inside the sphere.

The comparison between the point-like and the physical source simulation is highlighted

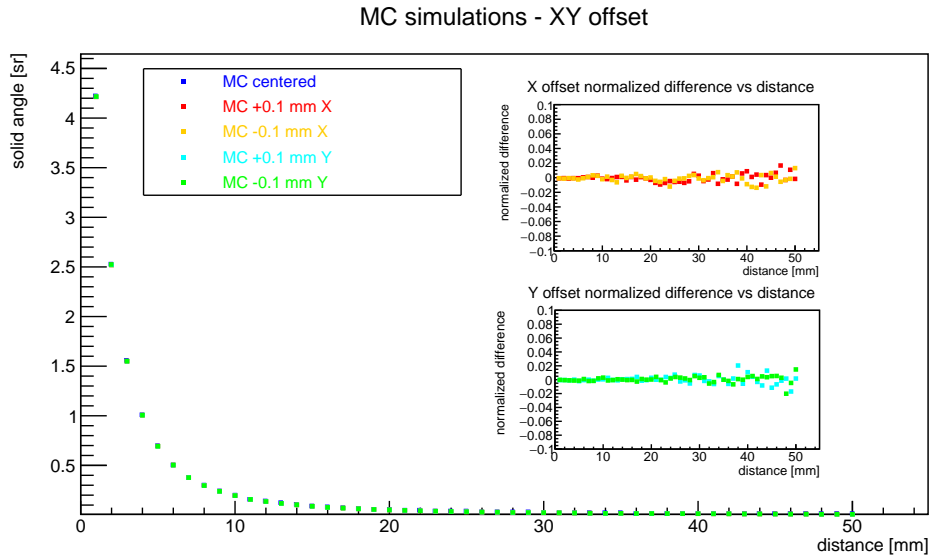


Figure 4.25: Comparison between the centered simulation and four simulations with positive and negative offset along the xy-plane (parallel to detector). The box plots show the normalized difference between the shifted and centered simulations, separately for the x and y offsets.

in the inset. The normalized difference is centered along zero and no substantial systematic deviation is seen between the two source models.

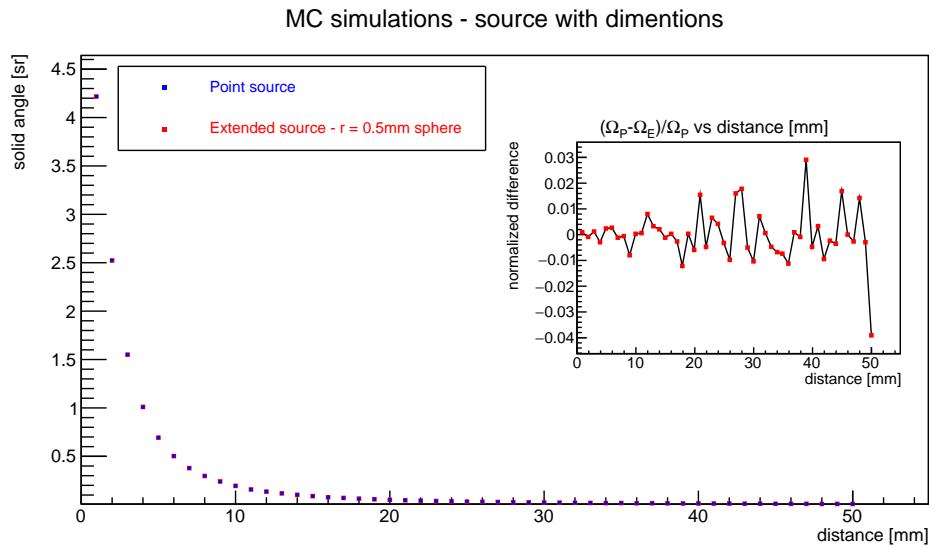


Figure 4.26: Comparison between point-like and physical source simulations. The source is modeled as a 0.5 mm radius sphere. The box plot shows that the normalized difference between the two simulations is centered at zero.

4.4.3.3 Detailed simulation

The simulation results presented in Section 4.4.3.2 (Fig. 4.24, 4.25 and 4.26) account only for the geometrical parameters of the system, like detector position and source dimensions. They neglect physical phenomena related to the emission such as self-absorption and backscattering. I therefore expand my simulation study by using Fluka [52] to model the experimental setup in a more comprehensive way.

Figure 4.27 shows the simulated system: the left panel contains the Plexiglas box in which the source and the detector are placed. The right panel shows a magnified sketch of the detector and source configuration. The active part of the source is modeled as a

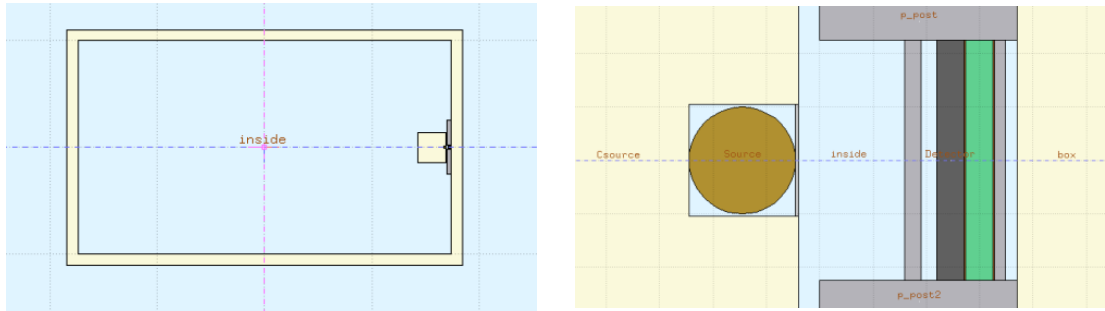


Figure 4.27: Sketch of the experimental setup implemented for the simulation (left panel) and magnified sketch highlighting the source and the detector configuration (right panel).

0.5 mm radius sphere of $^{90}_{38}\text{Sr}$. The strontium β decay is implemented in the Fluka code. It generates an electron energy spectrum as the one described in Fig. 4.4.

The strontium sphere is inserted in a support that, along with a cover, completes the source geometrical description. The detector is drawn as a diamond crystal with the electrodes, the package and the aluminum cover. The detector is inserted in an aluminum support and the whole system is inserted in an air volume.

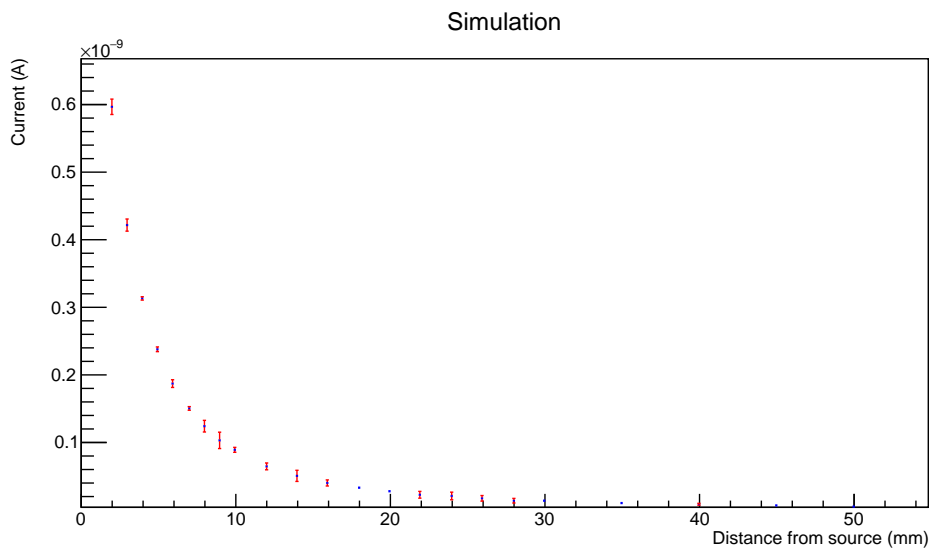


Figure 4.28: Simulated current as a function of detector-source distance.

I repeat the simulation for the set of source-detector distances used in the measurements.

The energy E deposited in the diamond bulk is calculated as output. Given the energy needed to create an electron-hole pair ϵ , derived from the TCT measurements, and the source activity A , the simulated output current I_s is written as

$$I_s = \frac{E_s}{\epsilon} A e , \quad (4.24)$$

where e is the electron charge.

As an output of the simulation, the plot in Fig. 4.28 is produced. The current as a function of the source-detector distance shows an analogous decreasing trend as the one shown by data.

4.4.3.4 Data fit and comparison with the simulation

Given the two functions in Eq. (4.13) and (4.15), I fit the calibration data for all the analyzed diamond detectors and compare the results with simulation to find possible discrepancies and trace them back to sensor properties.

Figure 4.29 presents an example of this fit procedure. Each of the four data sets is fitted with both fit functions. The fit parameters are reported in the top-right boxes in each plot. The two fit functions, overlaid to the data, are indistinguishable: the offset

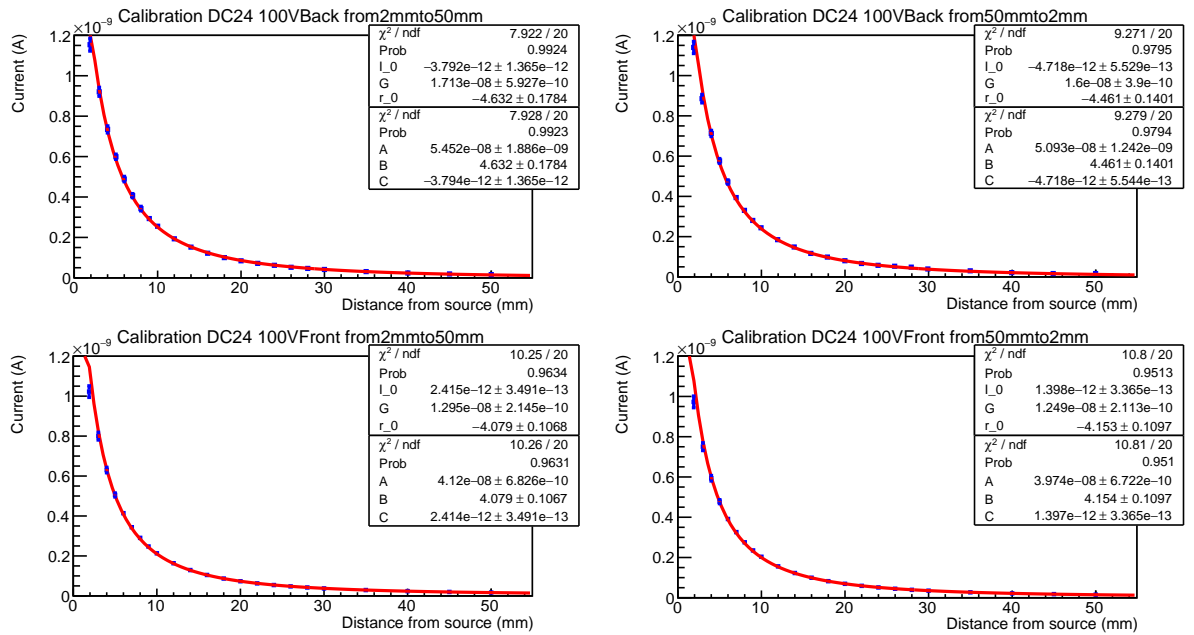


Figure 4.29: DC24 calibration data with fit results with functions 4.13 and 4.15 overlaid.

of about 4.5 mm reduces the range in which the functions diverge one from the other. Therefore the advantage of using a more precise solid-angle value (Eq. 4.23) is limited. The horizontal and vertical offsets of the two fit functions almost coincide for a data set.

Also in calibrations, diamond sensors show different responses with opposite polarizations, as shown by comparing two plots in the same column of Fig. 4.29.

Another common feature is the somehow counterintuitive increase in output current if the source is moved away from the sensor (from 2 mm to 50 mm) than if it is moved closer to it (from 50 mm to 2 mm). This might be explained by the so called *pumping effect*. As the diamond sensor is irradiated, the output current increases because the trapping levels that populate the band gap are filled and made inactive. During the 2mm-to-50mm

movement, the flux absorbed by the detector is higher than the one absorbed during the opposite movement. This behavior is due to the particular movement of the slider on which the detector is mounted and to the measurement of the offset value at the beginning of the calibration. This can explain the difference observed between the plots on the same row in Fig. 4.29.

In order to obtain the conversion factor between the output current and the dose rate absorbed by the diamond sensor, a comparison between data and simulation is needed. The four plots in Fig. 4.30 summarize the comparison.

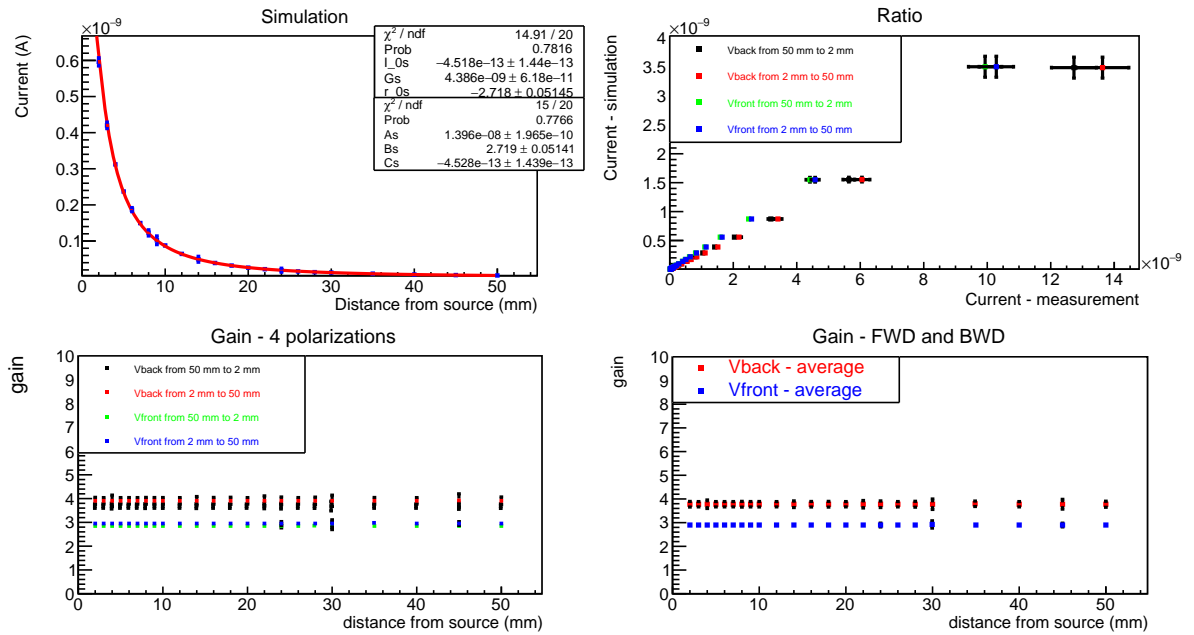


Figure 4.30: Comparison between data and simulation. The top-left panel shows the simulated data and their fit using functions of Eq. (4.13) and (4.15). The top-right panel represents the simulated current as a function of the measured current. The bottom left plot shows the gain between the measured and simulated current for each of the four configurations. An average gain for the front and back polarizations is represented in the bottom-right panel.

The top-left panel in Fig. 4.30 shows the fits done on the simulated current as a function of the distance. As for the experimental data, I fit the simulated current profile with the functions of Eq. (4.13) and (4.15). The resulting parameters, listed in boxes on the plot, show that the results obtained with the two fit functions almost coincide.

The measured current is higher than the simulated one. In order to compare data and simulation, I use the fit functions as a summary of the data points. Since the fit results almost coincide, for this comparison only fit functions expressed in Eq. (4.13) are considered for simplicity. The fit functions are compared by shifting their asymptotes to match them and evaluating the function values at each measured point.

The top-right panel in Fig. 4.30 shows the linear correlation between measured and simulated currents, indicating a constant gain value. The bottom-left panel shows the gains for the four different configurations during data taking, as functions of the distance. These gains are the (inverse) angular coefficients of the lines in the top right panel. Since the gain has to be unique for a given sensor polarization, the bottom right panel shows the

average values for back and front polarizations.

I repeat the same analysis for the whole set of diamond detectors. Table 4.6 lists the gain values obtained.

Sensor ID	Front gain	Back gain
DC24	2.90 ± 0.01 (b)	3.78 ± 0.03
DC25	—	5.86 ± 0.04 (b)
DC26	5.23 ± 0.02	5.25 ± 0.02 (b)
DC27	4.99 ± 0.02 (b)	6.23 ± 0.03

Table 4.6: Sensor gains obtained with the comparison between the calibration data and the simulation. The best side, obtained with stability measurements, is indicated with (b). The DC25 front calibration is not performed due to high instability.

Higher than one gains may be explained by a *photo-conductive gain*. Non-blocking contacts can inject charges into the diamond bulk that are not generated by the impinging radiation. This further injection may lead to a higher output current with respect to the one produced by the radiation contribution itself. This contribution is the only one taken into account by the simulation.

4.4.3.5 Current dose-rate conversion

In order to transform the output current, which is the quantity directly measured, into the dose rate absorbed by the detector, which is the relevant indirect quantity to monitor, I calculate a conversion factor.

First we introduce the *rad*, $1 \text{ rad} = 0.01 \text{ J/kg}$, as a unit of absorbed-radiation dose, D . The measured current I_m is written as

$$I_m = GI_s = G \frac{E}{\epsilon} eA = \frac{GeM}{\epsilon} \frac{dD}{dt}, \quad (4.25)$$

where G is the photo-conductive gain, I_s is the simulated current, E the energy absorbed by the diamond, M the sensor mass, e the elementary charge and ϵ the energy needed to create an e-h pair inside the diamond bulk.

Inverting Eq. (4.25) leads to the dose rate as a function of the read current

$$\frac{dD}{dt} = \frac{F}{G} I_m. \quad (4.26)$$

The conversion factor F is sensor-dependent because it contains the ϵ value. However, for an estimate we consider the average value $\epsilon = 16.36 \text{ eV}$, obtained from the TCT measurements. Starting from $\rho = 3.53 \text{ g/cm}^3$ and $V = (0.45 \times 0.45 \times 0.05) \text{ cm}^3$, the density and volume of the diamond sensor respectively, I calculate the conversion factor as

$$F = \frac{\epsilon[\text{J}]}{e[\text{C}]M[\text{kg}]} = 45.78 \frac{\text{mrad/s}}{\text{nA}}. \quad (4.27)$$

The final sensor-dependent conversion factors are determined by repeating the calibration after cover gluing, with complete detectors.

4.5 Characterization results

After performing the full characterization on several diamond detectors, some common features emerge.

- Each diamond sensor shows different behaviors with opposite polarization. I relate this asymmetry to the crystal growth direction as this is the only aspect that introduces a symmetry breaking in the system.
- Each diamond sensor has peculiar characteristics. Even if all sensors are produced by the same company following consistent procedures and specific techniques, the electrical and microscopical properties show large differences, due to impurities in the bulk and near contacts. This is one of the main differences between silicon and diamond devices.
- The measured values such as mobilities, saturation velocities, and e-h creation energies are consistent with literature [47].
- I verify a linear relation between the dose rate absorbed and the output current. This relation enables to use diamonds as radiation monitors.

Although the detectors tested for the Belle II radiation system show a limited uniformity both in electrical and microscopic properties, diamond-based detectors prove to be the best options for specific applications, including radiation monitor and dosimetry. The high radiation hardness and thermal conductivity is essential to build detectors that can operate in extreme conditions, where the use of silicon devices is impractical. The high reliability allows to operate diamond detectors for several years without important performance degradation, avoiding interventions and replacements.

4.6 Cover mounting and final tests

When the α and β sources characterization is completed, the aluminum cover is glued on the package to protect the diamond sensor permanently. This procedure is done by applying conductive glue and letting it cure in oven at around 80° for several hours. When the glue is cured, the detector is tested again with the β source, thought stability, IV, and calibration measurements. Usually the curing does not affect the diamond response.

At the end of the constructing and testing processes the complete $(18 \times 12 \times 3.1)$ mm³ detector is obtained.

Chapter 5

Diamonds at work in SuperKEKB collision operations

In this chapter I discuss the main operations and measurements performed in the first accelerator and detector commissioning period with beam collisions. I focus on the diamond radiation monitoring and beam abort system, highlighting its role in protecting the Belle II inner detector and tuning the accelerator conditions. This chapter also reports the very first analysis of diamond data.

5.1 Commissioning overview

The diamond monitoring system is the Belle II subdetector dedicated to avoid permanent damage and performance degradation of the inner part of the detector. Prior to relying completely on the system in physics operations to trigger protective actions, the system has to be tested. During the accelerator commissioning phase the background conditions are less harsh than expected at full luminosity conditions. Therefore this phase offers a convenient opportunity to test all the system components without risking major issues to the inner detector in case of malfunctions.

Belle II operations with beams are conventionally divided into three time periods (phases) (Table 5.1). During Phase 2 operations, which is the period concerned in this

Phase	Period	Main goals	Detectors	Diamonds
Phase 1	February-July 2016	Accelerator tuning and background tests w/o final focusing	w/o Belle II, other detectors for background studies	4 diamonds on a provisional beam pipe
Phase 2	March-July 2018	Verification of nano-beam, background study and physics data	w/ partial Belle II (partial PXD and SVD)	8 diamonds on a beam pipe close to the final one
Phase 3	From February 2019	Complete physics program	w/ Belle II	8 diamonds on the beam pipe and 12 on the SVD layer 3 supports

Table 5.1: Summary of the three commissioning phases of SuperKEKB and Belle II.

chapter, the Belle II collaboration has set two main goals. The first one is to reach the maximum luminosity of the predecessor machine, KEKB, ($2.11 \times 10^{34} \text{ cm}^{-2}\text{s}^{-1}$), thus validating the nano-beam scheme described in Sec. 2.2.1. The second goal is to operate the Belle II detector smoothly, within controlled background levels.

During this phase the final vertex detector (PXD and SVD) is replaced by a combination of several detectors dedicated to the measurement of backgrounds, collectively denominated BEAST II [31], and just one provisional azimuthal sector of PXD and SVD.

5.2 Diamond system goals

The diamond radiation monitor system is part of a broader set of systems used to monitor the environmental conditions within the vertex detector volume (Appendix A). The chief goal of the diamond system is to monitor the radiation near the interaction point and trigger protective actions if radiation rates exceed the safety thresholds.

The system achieves this goal through two capabilities.

- **Continuous radiation monitoring:** the dose rate collected by the diamond sensors is read and archived with a 10 Hz sampling frequency. The radiation level (instantaneous dose rate) is made available online and used as a reference for the beam background during accelerator-tuning operations, such as collimator adjustments and beam-optic tuning. The decision to power the inner subdetector is also based on diamond dose-rate measurements. The archived dose rates are also used to estimate the total integrated doses absorbed by the silicon detectors.
- **Beam abort request:** the diamond system aborts the beams if the radiation level near the interaction point exceeds a programmable threshold.

This functionality uses data read at 100 kHz to match the beam revolution frequency. If a potentially harmful beam-loss is detected, the abort signal is generated within one beam revolution period. Each threshold is determined by two values: the *integration interval*, which identifies the time gate for data collection and the *threshold value*, which is the mean dose-rate threshold beyond which an abort request is generated. I adjust the threshold values based on the accelerator conditions and other subdetectors requests.

The comparison between the dose-rate measured and the threshold is performed within a running window that has a gate equal to the integration interval. Every 10 μs a new value is added to the running window and the oldest value is excluded. Another parameter relevant for the abort configuration is the sensor *multiplicity*: it establishes the minimum fraction of diamond sensors that have to yield a signal over threshold to generate an abort request.

Various configurations of beam-abort thresholds can be implemented to cope with the varying accelerator conditions. Table 5.2 summarizes them, distinguishing between time settings (*fast* and *slow*) and threshold values (*strict* and *loose*). The SuperKEKB beam-abort system is upgraded from KEKB [62]. Beam-abort requests from more than one hundred loss monitors around the ring are collected locally and delivered to the central control room of the accelerator (CCR), as shown in Fig. 5.1. Logical ORs of these signals, separately for LER and HER, trigger kicker magnets, that quickly dump the beams in a controlled way. The kicker trigger is also sent back to the Belle II control room and other locations, to save detailed beam loss data locally and allow a "post-abort" analysis of the beam losses that immediately preceded the occurrence of a given abort.

Abort type	Configuration
Fast	It is intended to protect the vertex detector from fast radiation spikes that are particularly harmful when the detector high-voltages are on. The integration interval is typically in the millisecond range.
Slow	It is intended to control the slow rising of the dose, to keep within limits the total integrated dose in the vertex detector. The integration interval is typically in the second range.
Strict	A strict threshold is enabled during normal operations, when the vertex detector high voltage bias is active, to collect data.
Loose	A higher threshold value is uploaded during injections and accelerator special runs, when several parameters are tuned and radiation background is expected to be high, while the vertex detector bias voltage is off.

Table 5.2: Summary of the beam abort configurations.

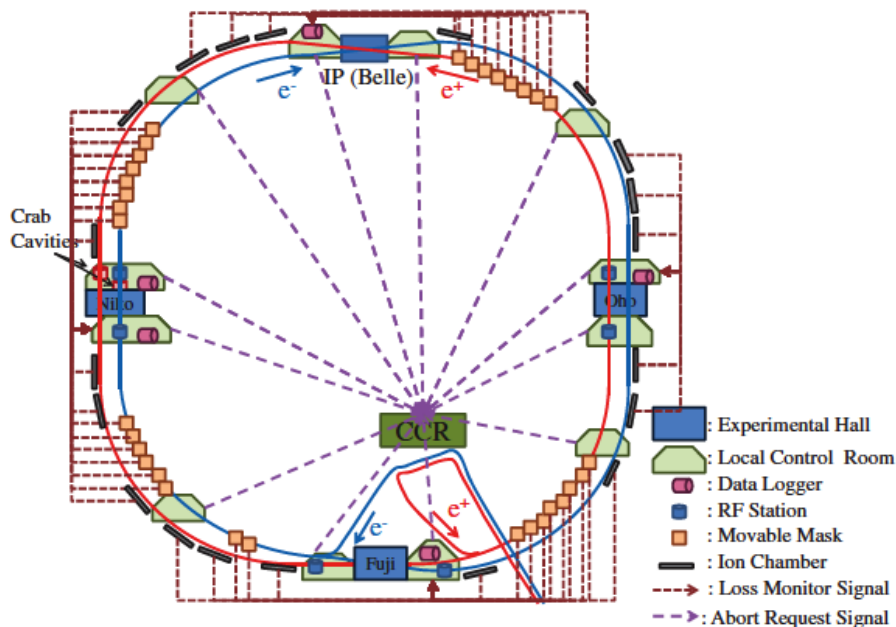


Figure 5.1: Scheme of the SuperKEKB beam-abort system made of ionization chambers located around the ring to detect beam losses.

5.3 Diamond setup and readout

During Phase 2, eight diamond detectors are mounted on the beam pipe at radii of about 20 mm from its axis. Four are in the backward region (BWD) longitudinally displaced by 100 mm from the interaction point (IP) and four are in the forward region (FWD) at 138 mm (Fig. 5.2). Forward and backward regions are identified with respect to the HER beam direction, according to Belle II reference system (Fig. 5.3). The system origin is located inside the vertex detector, with x, y, and z axes pointing horizontally outwards from the ring center, vertically upwards, and in the HER direction respectively.

Their azimuthal angles of diamond detectors around the beam pipe are $\phi = 55^\circ, 125^\circ,$

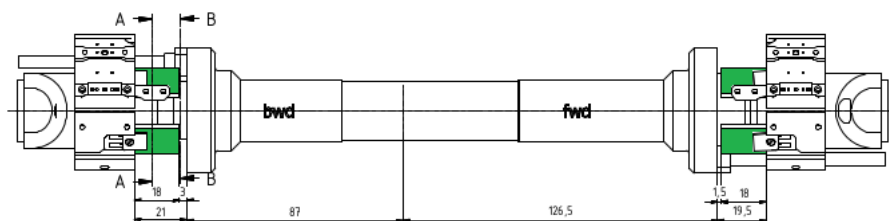


Figure 5.2: Drawing of the diamond detector (in green) positioning on the beam pipe.

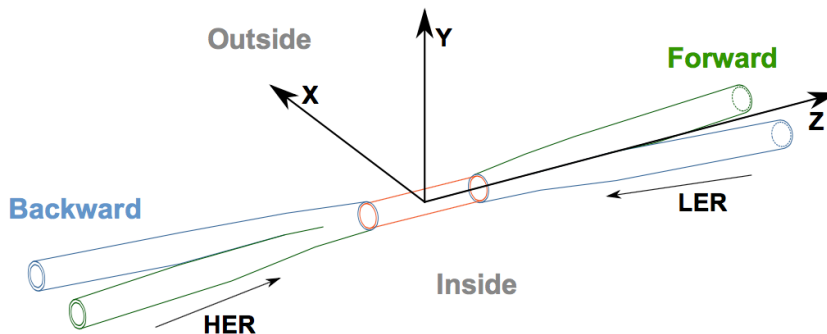


Figure 5.3: Belle II reference system. The system origin is located inside the vertex detector.

235°, 305°, which correspond to diamond channels 0 to 3.

5.3.1 Readout electronics

The readout electronics for the diamond system is designed and built for this specific application by the instrumentation group of Elettra Sincrotrone Trieste [63], following specifications of and in collaboration with the Belle II Trieste group. The system is composed of modules or "control units", each dealing with four diamond detectors. Figure 5.4 shows a schematic representation of the DCU logic components.

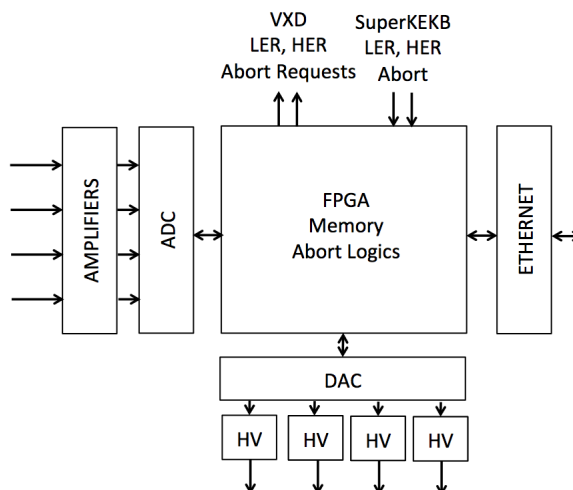


Figure 5.4: Block diagram representing the main DCU functional components.

The core element of each DCU is a field programmable gate array (FPGA) that deals with several input-output subsystems. The FPGA controls a digital to analog converter (DAC) board to drive the HV supply units that power the sensors. Each supply unit can deliver a voltage between 0 V and 1000 V.

The current generated inside each diamond sensor is amplified and read by four analog-to-digital converters (ADC) independently. Each ADC provides a 16-bit digitized current value at 50 MHz sampling frequency. Three digitization current ranges are available: ± 10 nA, ± 1 μ A, and ± 1 mA. I select the appropriate range during the DCU configuration process: a smaller range allows to measure small dose rates accurately, underestimating the contribution from high radiation spikes due to response saturation. As the available range increases the sensitivity lowers, allowing to measure higher dose-rate contributions.

Figure 5.5 schematically represents the data flow for each detector, as programmed in the FPGA firmware.

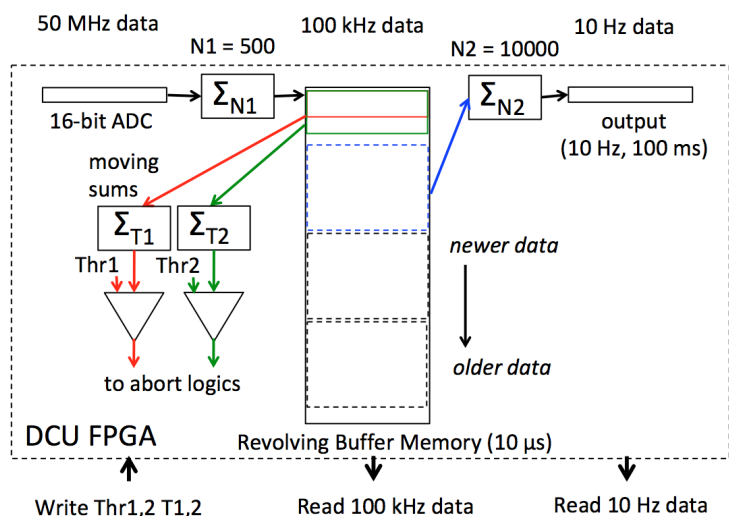


Figure 5.5: Block diagram representing the DCU data stream.

Two different data streaming frequencies are provided by the DCU, 100 kHz for abort request purposes and 10 Hz for monitoring. Starting from data at 50 MHz, 100 kHz data are obtained by adding up 500 50 MHz-values. This summation is labeled as Σ_{N1} in Fig. 5.5. The oversampling at 50 MHz and the consequent sum reduces the noise, widening the useful dynamic range.

Data are written on a revolving buffer and two moving sums are calculated from the diamonds to issue abort requests. The user-defined number T1 (T2) of addenda of each sum identifies the integration interval parameter described in Sec. 5.2. A short integration interval enables to detect fast changes in the dose rate while a large integration interval allows to average over a wider time gate, mediating different contributions.

One moving sum is devoted to fast-type aborts and the other to slow-type aborts. Every 10 μ s, each moving sum is updated with the current value and compared with the threshold value Thr1 (Thr2). If the value exceeds the threshold, an abort request is generated and propagated via a TTL signal externally.

The radiation monitoring system works with other beam-loss monitors placed along the ring. If an abort request is generated, either from the other beam loss monitors or the diamond detectors, the SuperKEKB system returns, as a confirmation, signals labeled as SuperKEKB HER (LER) Abort (Fig. 5.4 and 5.6). When these signals are received by the

DCUs, data in revolving buffer are saved for post-abort analysis.

- If the abort has been generated by the diamond system, the abort type (fast or slow) can be determined from the data stored in the revolving buffers: from them I reconstruct the values of the moving sums within the running windows, and compare them with the fast and slow programmed thresholds.
- If the abort has been generated by SuperKEKB loss monitors, I check whether a high dose-rate background is observed at the same time near the interaction region or not.
- Whatever the abort source, I check the angular dose-rate distribution seen by diamonds. As the beam loss is usually not uniform distributed, typically one of the four diamond sensors has a higher response than the others.

If no abort request is issued, 100 kHz data are periodically overwritten within the revolving buffer.

10 Hz data are obtained by adding up ten thousand 100 kHz-values. This summation is labeled as Σ_{N_2} in Fig. 5.5. 10 Hz data are continuously read and stored for monitoring purposes and off-line analysis. A 10 Hz frequency enables to estimate the dose absorbed by the vertex detector, correlating it with potential change in detector performances.

Table 5.3 summarizes the ranges and sensitivities for each configuration, assuming a typical conversion factor of 10 (mrad/s)/nA between current and dose rate, and using the two data frequencies and the three current ranges. The communication with the DCU is

Current range	Dose-rate range	Current sensitivity (10 Hz)	Current sensitivity (100 kHz)	Dose-rate sensitivity (10 Hz)	Dose-rate sensitivity (100 kHz)
± 10 nA	100 mrad/s	0.3 pA	30 pA	3 μ rad/s	0.3 mrad/s
± 1 μ A	10 rad/s	30 pA	3 nA	0.3 mrad/s	30 mrad/s
± 1 mA	10 krad/s	30 nA	3 μ A	0.3 rad/s	30 rad/s

Table 5.3: Summary of the ranges and sensitivities for various DCU configurations and data frequencies.

managed through an Ethernet interface by the "slow control" software of the experiment, based on EPICS (experimental physics and industrial control system) [64]. EPICS interfaces to the external world with input output controllers. Within the radiation system several controllers are implemented to convert ADC values in physical units (mrad/s), program and enable or disable the abort conditions, and monitor the correct DCU operations.

5.3.2 External circuit

The DCUs are located in an "electronic hut", near the Belle II detector, along with the Belle II main data acquisition systems. The communication between the DCUs and the accelerator control room is based on optical fibers. The abort requests are exchanged through these fibers, achieving low-noise communication between systems that are a few kilometers apart.

The accelerator group provides optical-to-electrical converters located close to the DCUs: optical-to-NIM for the *SuperKEKB HER (LER) Abort* signals, used as inputs to DCUs, and TTL-to-optical converters for diamond-related abort request signals, obtained as DCU outputs. To adapt the logic levels of the electrical signals and provide

some additional access to them for debugging purposes, we set up some external logics in a NIM crate, as shown in the diagram of Fig. 5.6. The *SuperKEKB HER (LER) Abort*

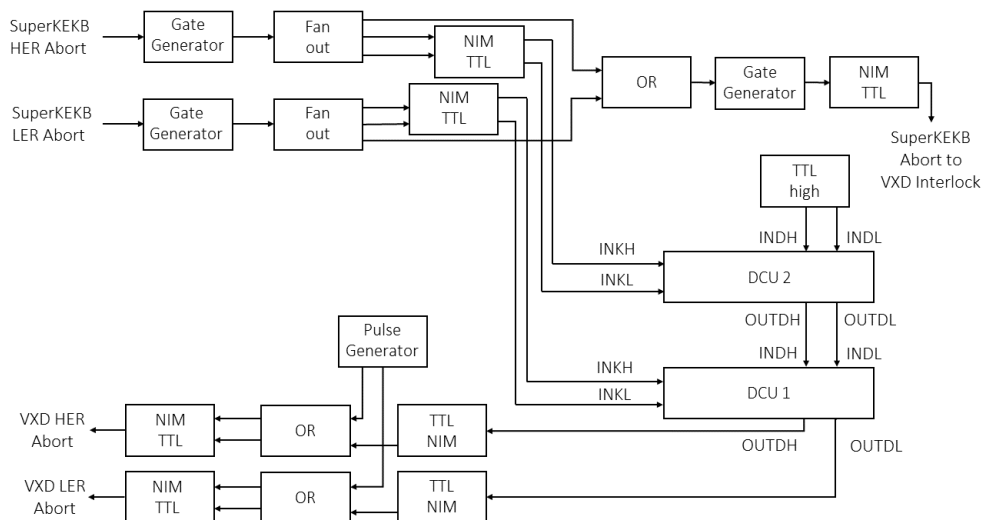


Figure 5.6: Schematic representation of the external circuit main components in the NIM crate.

NIM signals, originated from the SuperKEKB central control room, are fed to two gate generators, that can be used to change the signal width.

These signals are fanned out to serve different purposes. Two of them enter in an *OR module* to generate a common interlock signal. This signal, converted to TTL logic, is used as an interlock for the vertex detector (VXD) power supplies (see Appendix A). As a beam loss is detected, the VXD is powered down to protect it.

The other fan-out outputs are converted to TTL logic and sent, in input, to the DCUs. The corresponding DCU inputs from SuperKEKB are labelled *INKH* and *INKL* (*H* for HER and *L* for LER).

The two diamond units used for Phase 2 are set in a daisy-chain configuration to produce a logical OR of their abort requests, separately for HER and LER.

Each DCU is connected to four diamond detectors. It can generate abort signals based on the diamond output and programmed settings. The abort signal is propagated via the daisy chain through the *INDH/L* and *OUTDH/L* inputs and outputs. The last DCU sends the abort request, generated by diamond sensors to the accelerator control room via the *VXD HER/LER Abort* signals. These signals contribute to the central beam-abort system as described in Sec. 5.2.

Since the first DCU in the chain has no previous inputs from other DCUs, its *INDH* and *INDL* terminals are connected to a +5V TTL high signal. At the end of the chain, a *pulse generator* is used to manually generate signals to test the abort communication lines between Belle II and the SuperKEKB control room.

The entire SuperKEKB abort logic, including diamond-related aborts, is based on "enable" signals. In normal condition the sensors around the ring send a +5V TTL high level. If a beam loss is detected, they switch the level to 0 V. This logic treats a wrongly disconnected cable and an abort request on the same footing, for additional safety.

5.4 Readout installation and test

Before Phase 2 operations with beams, we mounted two DCUs and the external NIM electronics. Prior to operating the detectors with the DCUs, we performed an initial debugging of the interconnections, applying the bias voltage to each detector.

Figure 5.7 shows the front panels of the two DCUs. Several LEDs show the current status of the box, such as FPGA and memory status and the presence of abort requests, if any. We read and interpreted the DCUs outputs using a stand-alone program, written

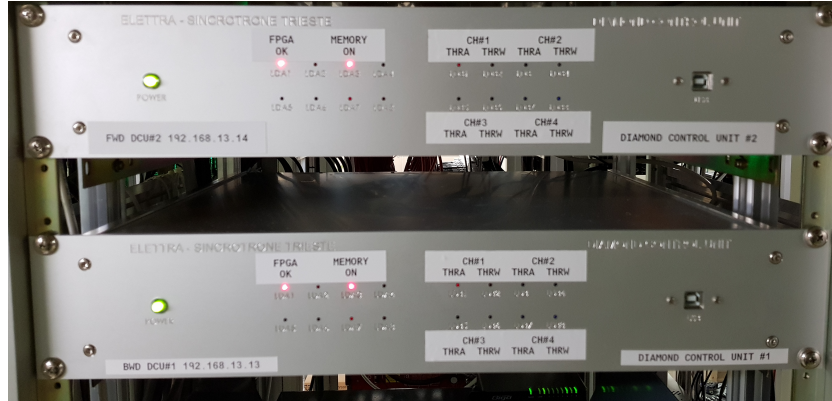


Figure 5.7: Front panels of the diamond control units used during Phase 2 operations.

as a LabView virtual instrument [65]. We checked that the output values are read and memorized correctly, also simulating abort requests. Since the tests were performed with no beams, we did not measure any physical background; however, we estimated the noise levels.

Figure 5.8 shows the output-current distribution of the BWD channel 2 detector. The distribution corresponds to data sampled at 10 Hz within a ± 10 nA current range.

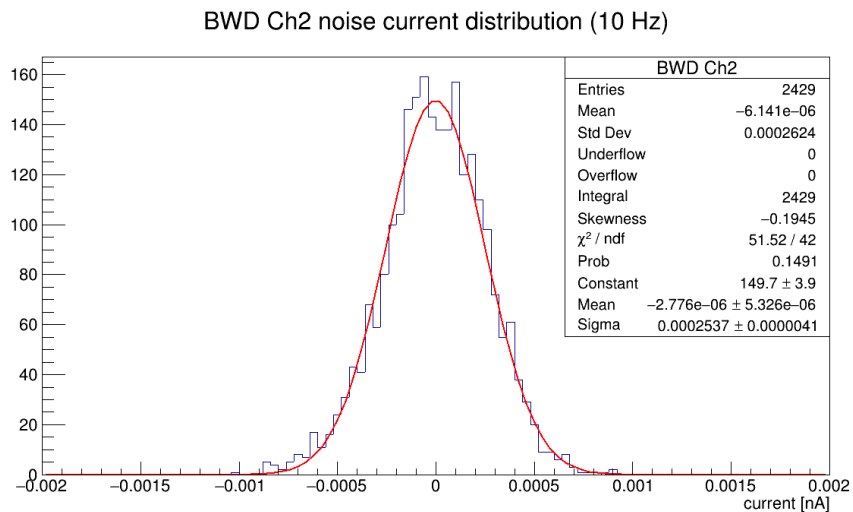


Figure 5.8: BWD channel 2 noise current distribution. Data are sampled at 10 Hz within a ± 10 nA current range. The fitted Gaussian (red line) is superimposed to data. The fit parameters are listed in the histogram insertion.

The noise distribution has a Gaussian shape. I fit the histogram with a Gaussian function,

superimposing the result to the data. The mean is the pedestal value of the measured data set and its standard deviation represents the noise level. The measured value of the standard deviation is about 0.3 pA, corresponding to the current sensitivity shown in Table 5.3 at the corresponding current range (± 10 nA) and data sampling rate (10 Hz).

During beam operations, also the pedestal value has to be measured. Since the pedestal is included in the signal digitized by the DCU, the output cannot be directly converted into dose-rate values. In order to estimate the dose level correctly, the pedestal must be subtracted. During Phase 2, I measured pedestal values for each diamond detector periodically. I used the distribution mean values to update the DCU configuration files, allowing an automated pedestal subtraction. Typically the pedestal values fluctuate within few ADC channels.

The conversion factor between ADC counts and sensor-current value is obtained as the ratio between the set current range and 2^n , where n is the number of ADC channels available. In the DCU case n is equal to 16. The conversion factor between the sensor-current value and the dose-rate value is derived from detector-calibration measurements (Sec. 4.4.3).

5.5 Abort system test

During early Phase 2 the need to monitor low dose rates due to low beam currents while providing protective actions against high-dose spikes brought us to use the most sensitive current range for four diamonds and the less sensitive but higher-range current scale for the other four. With such high thresholds we did not send any abort request, because of the low beam currents.

To verify the proper functioning of the system, the priority was to test the diamond beam-abort system (Fig. 5.9).

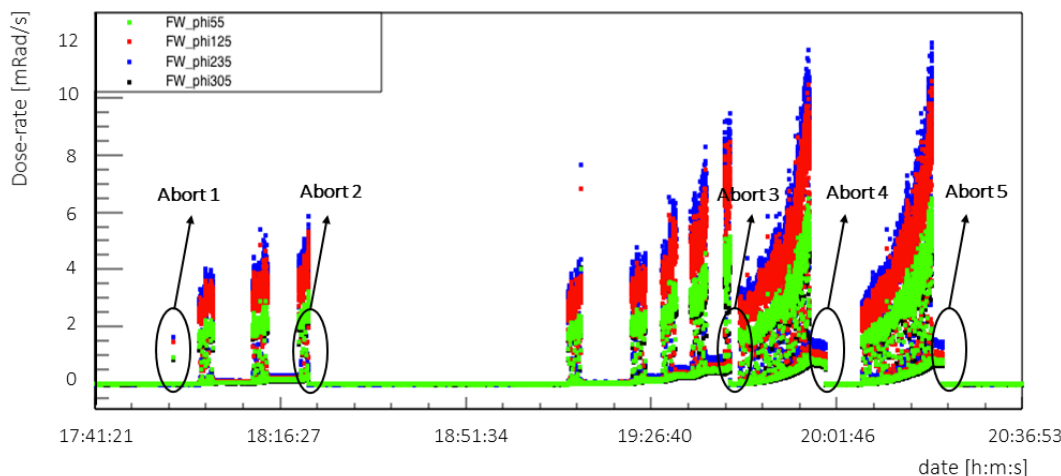


Figure 5.9: FWD diamond dose rates (mrad/s) monitored by 10 Hz data as a function of time during the abort test. The generated aborts are highlighted.

We set different rather low threshold values, asking the accelerator experts to inject the beams, obtaining increasing background levels. They injected with steps in beam current at 40 mA, 80 mA, and 120 mA. We programmed the DCUs to test the abort mechanism first during injection and then during storage. The first abort is related to a threshold of 1 μ rad integrated along 1 ms, corresponding to an average dose rate of 1 mrad/s in that

time interval. As we enabled this setting, the system delivered an abort signal during the first injection when the LER beam current increased from 0 to 40 mA. For the second abort we decided to set a higher threshold (0.5 mrad integrated in 10 ms: 50 mrad/s average dose rate). An abort was delivered during the third injection, when the beam current had reached about 120 mA.

In order to test the system during beam storage, we disabled diamond abort request during injection, and re-enabled it with an appropriate threshold only after the injection was completed. Abort 3 in Fig. 5.9 is caused by an accelerator beam loss monitor and not by the diamond system. Aborts 4 and 5 are generated by diamonds during beam storage, as expected from the comparison of the typical dose rate in those conditions with the preset abort threshold. As an abort is generated, a step in the dose rates is observed as the beam current is dumped to zero.

Figure 5.10 shows the comparison between moving sums of 100 kHz data and the fast threshold set at 50 mrad, integrated in 10 ms (sum of 1000 data values, recorded every 10 μ s at 100 kHz). The moving sums are computed off-line from the data stored in the

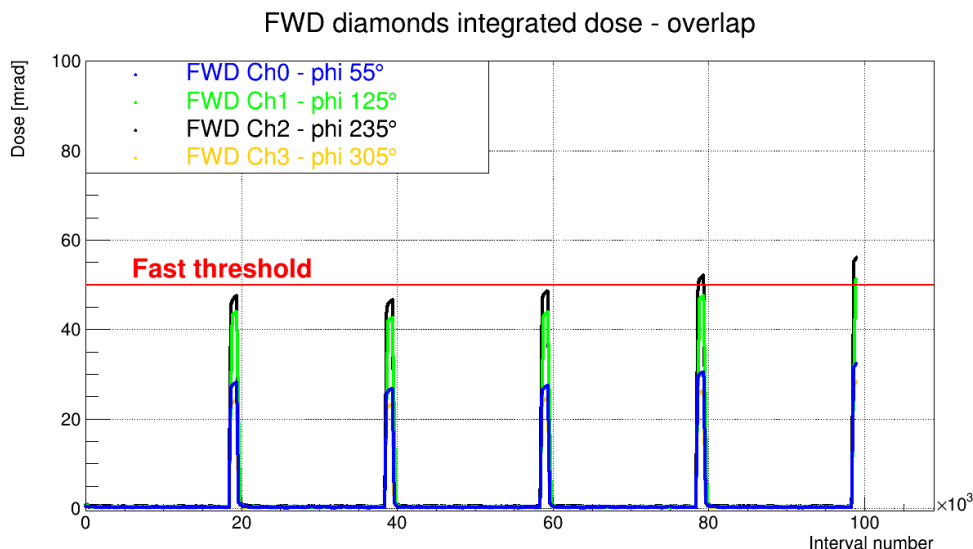


Figure 5.10: Moving sums of radiation doses measured by the forward diamonds, immediately preceding one of the beam-abort tests. Details are explained in the text.

revolving buffer memory, frozen and read-out after the abort has occurred, after subtracting pedestals and converting from ADC counts to dose units. The off-line computation mimics the equivalent algorithm performed by the FPGA firmware in ADC units: moving sums are updated every 10 μ s, adding the new data point and subtracting the oldest one in the sum. The horizontal axis is labeled "interval number": this is an integer corresponding to the pointer of the revolving memory, increasing every 10 μ s: the full range corresponds to 100000 "interval numbers", namely the portion of memory read out after each abort, containing the history of a one-second time interval preceding the abort confirmation from SuperKEKB [66].

Several peaks are visible, separated by 20000 "time intervals" (0.2 s in time units). They correspond exactly to the ongoing 5 Hz injection of beam particles: at these low beam currents, beam losses are negligible, except during the short injection time intervals, when a radiation dose peak is clearly visible for the four FWD diamond sensors, represented in different colors. Peak values are initially below threshold; only at the rightmost peak two

diamonds (channels 1 and 2) cross the threshold and successfully trigger an abort request, as required by the multiplicity-two condition (at least two channels simultaneously over threshold).

With this test we ensure the correct operation of the entire system, including DCUs, communication lines, beam dumping and data saving.

5.6 First diamond signals

To reach the goals set by the collaboration, the commissioning of SuperKEKB with collisions proceeded through the multiple repetition of two distinct tasks. On one hand the accelerator experts tuned the machine parameters to achieve high luminosities, while keeping background under control. On the other hand, once found satisfactory configurations for the parameters, they stabilized the beam conditions to allow smooth Belle II data taking. During the shifts in the accelerator control room, I took part in both activities. During

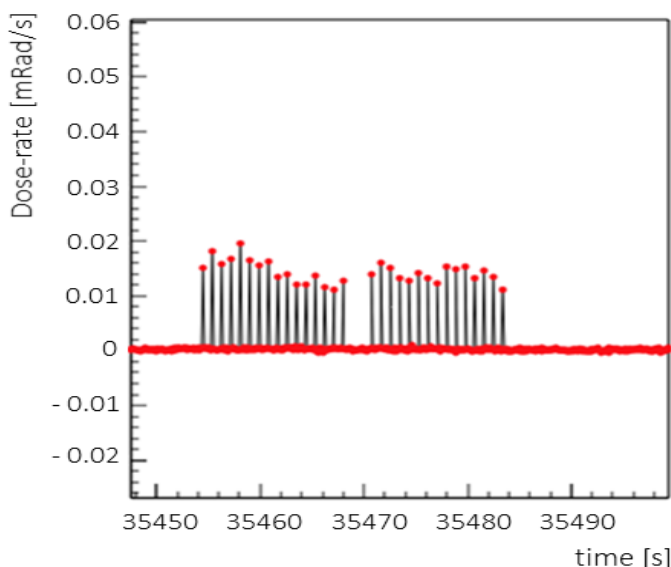


Figure 5.11: First diamond signal during beam injection. Dose rate as a function of time follows the 10 Hz injection pattern.

accelerator operations, the diamond dose rates proved essential to inform the accelerator physicists involved in tuning the machine parameters. Each time a parameter setting is changed, the background levels at the IR are monitored via diamond online readings.

Due to its protection effectiveness, the diamond system has been online since the start of Phase 2. Figure 5.11 shows the first background signal seen by diamonds, taken during injection. The periodic behavior is due to the injection pattern. Since new particles are added to the existing bunch at a 10 Hz frequency, the diamond sensors measure peaks in the dose rate with the same frequency.

These data clearly show the very good sensitivity to extremely low dose rates and the low noise level of the diamond detectors with their readout system.

5.7 Diamond parameter adjustments

During Phase 2, as we gained experience, we tuned the diamond system settings depending on the other subsystem requirements and the accelerator conditions.

We decided to use four diamonds for abort request purposes and the other four for radiation monitoring. This allows for setting the lowest 10 nA range on four diamonds and the highest 1 mA range on the remaining sensors. A smaller current range allows to achieve higher sensitivities given given the dynamic range achievable with an over-sampling 16-bit ADC.

In early Phase 2, we enabled only fast abort with a high threshold (1 rad integrated in 1 ms: average dose rate 1krad/s in that time interval). This choice allowed the accelerator experts to tune the machine parameters without being disrupted by frequent beam aborts. This threshold value sufficiently protects the VXD from radiation spikes, according to previous experience in the BaBar experiment [39]. Since in early Phase 2 we did not expect to integrate high beam currents, we did not enable the slow abort.

Later in Phase 2 we also used the 1 μA range: for monitoring purposes when high radiation peaks tended to saturate the lower 10 nA range as the beam currents were increased, and finally also as an appropriate range for lower abort thresholds.

Figure 5.12 shows the effects of a 1 μA -to-10 nA range change on the diamond outputs. As the sensitivity increases noise is reduced. We implemented this change to measure the

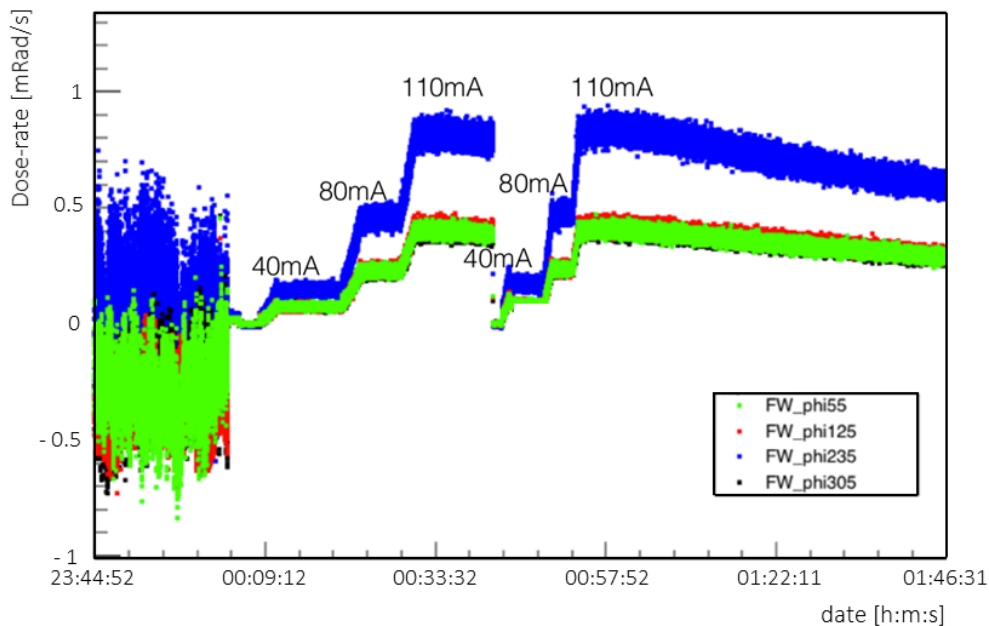


Figure 5.12: Dose rate as a function of time during a change of diamond current measurement range from 1 μA to 10 nA before a background study. As the current measurement range is lowered, the noise amplitude decreases.

dose rate with the highest sensitivity for a background study. During this study the LER beam current was increased in steps from 0 mA to 110 mA. The dose rate follows the same behavior, with dose rates approaching 0.5 to 1 mrad/s when the beam currents exceed about 100 mA, as Fig. 5.12 shows.

5.8 QCS quench protection

Thanks to its effectiveness during Phase 2 operations the purpose of the diamond abort system has been extended to a task initially not foreseen, the protection of the QCS magnets [67]. These superconducting quadrupole magnets, used to squeeze the beam transverse size just before the interaction point, are a key element in the nano-beam scheme.

Since these magnets are close to the beams, any beam loss in their vicinity can irradiate the magnets with high particle fluxes. The irradiation often causes a resistive transition of the magnet from the superconducting state to the normal state (quench). In this process, Joule heating converts magnetic energy stored in the magnet into heat. Usually the process starts in the localized region of the magnet where the beam loss is concentrated; and then it propagates quickly through a chain reaction that brings the entire magnet to a normal state, resulting in a rapid boil-off of the cryogenic fluid inside the magnet. Quenches have to be avoided as they can damage the superconducting magnets: for instance, an early Phase 2 quench caused serious damage that required a two day stop. Even in more benign cases, several hours were required to recover from the quench, before re-injecting beams and restarting data taking. After this accident, the diamond threshold has been reduced to help preventing quenches.

After analyzing previous quenches, we observed a correlation between a dose-rate increase in diamonds and the development of a quench. We therefore decided to set the fast threshold, 10 mrad integrated in 1 ms (10 rad/s average dose rate). We also decided to introduce a slow abort threshold (200 mrad integrated in 1 s: 200 mrad/s on average), based both on the quenches analysis and on the VXD specifications: the VXD is expected to absorb roughly $10\div 20$ Mrad during the Belle II ten-year data taking. This leads to a maximum tolerable average dose rate of about $100\div 200$ mrad/s.

With these abort settings 15 out of 19 QCS quenches in the previous two months would have been avoided. Aborting the beams in a fast way using the diamond response has decreased considerably the QCS quenches frequency, thus helping considerably the efficiency of Phase 2 operations.

5.9 Analysis of first diamond data

This section presents preliminary analyses of Phase 2 diamond data. They are intended to highlight some of the relevant contributions of the diamond radiation monitoring system to the characterization of beam losses and machine backgrounds, as a function of the evolving accelerator conditions.

5.9.1 Radiation doses

During accelerator operations we monitor the dose rates as function of time (Fig. 5.13). In the time window selected, both beams are present. The upper part of the plot shows the two beam-current profiles (yellow and blue lines for LER and HER respectively). As the currents decrease, a new injection is performed: the plot shows two injections at times approximately of 500 s and 3000 s. After the injections, decay profiles are visible for both beams. Electron and positron losses within the beams dominate the current decrease. Such losses are determined by several parameters such as the vacuum conditions, beam energy, beam size, and collimators settings.

The lower part of the plot shows the dose rates read by the diamond sensors. During storage periods, with no injections, the dose rates follow the currents profiles. During

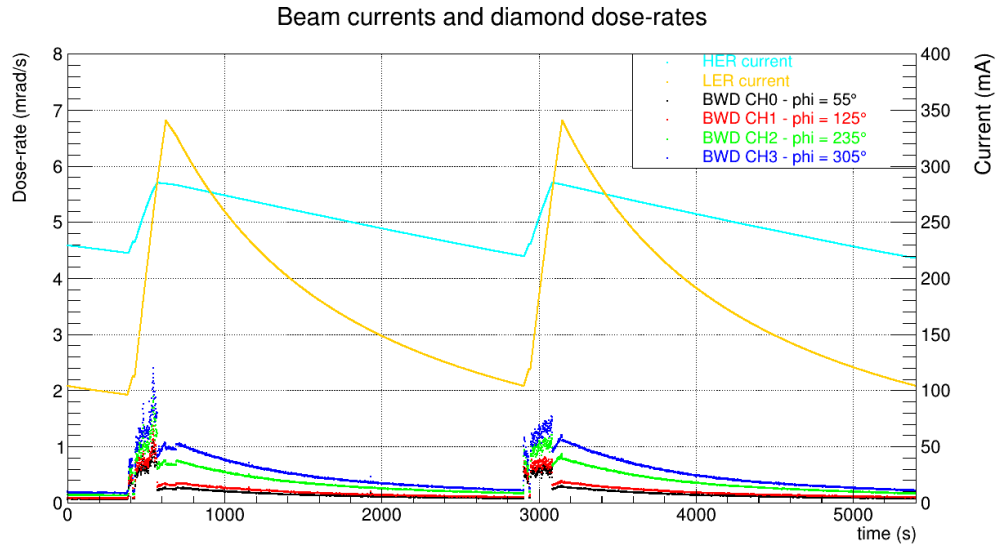


Figure 5.13: Correlation of beam currents and diamond dose rates as functions of time.

injection, the background increases due to instabilities within the beam where new particles are added. As a consequence the dose rates increase. Such increase demonstrates the need for a higher beam abort threshold during injections, as expressed in Table 5.2.

The dose rates shown in Fig. 5.13 are taken from the four backward diamond sensors, which had the most sensitive range selected (± 10 nA). Different sensors read different dose rates at the same time, due to different azimuthal positions around the beam pipe.

A correlation between these two quantities is shown in Fig. 5.14, to investigate the dependence of the dose rate seen by diamonds on the beam currents. As an example a

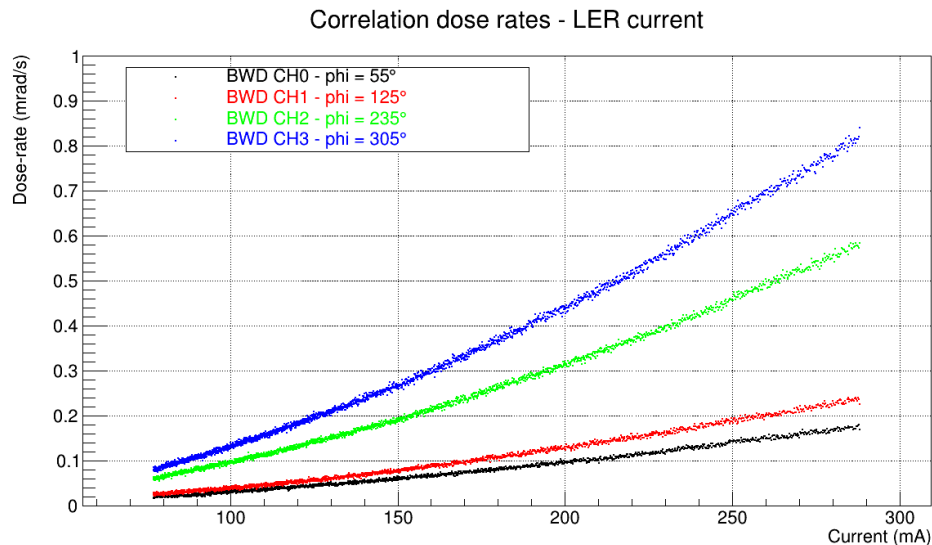


Figure 5.14: Correlation between LER beam current and diamond dose rates.

time window is selected where only the LER beam is present, the HER beam current is zero. The dose rates as a function of the LER beam current show a non linear behavior.

The dependence of the different background types from the beam current is described in Sec. 3.1: a linear dependence from the beam current is introduced by the p_0 component of

the beam-gas scattering while the quadratic dependence is carried by the dynamic pressure component and the Touschek effect. In Section 5.10 I use these dependences on the beam current and other beam parameters to separate different beam background components.

Another example of the monitoring capabilities of the diamond system at 10 Hz are the measurements of accumulated dose during the accelerator operations. Figure 5.15 shows the integrated doses absorbed by the four backward sensors as functions of time during three weeks. The integrated doses differ in different diamond sensors. The hierarchy

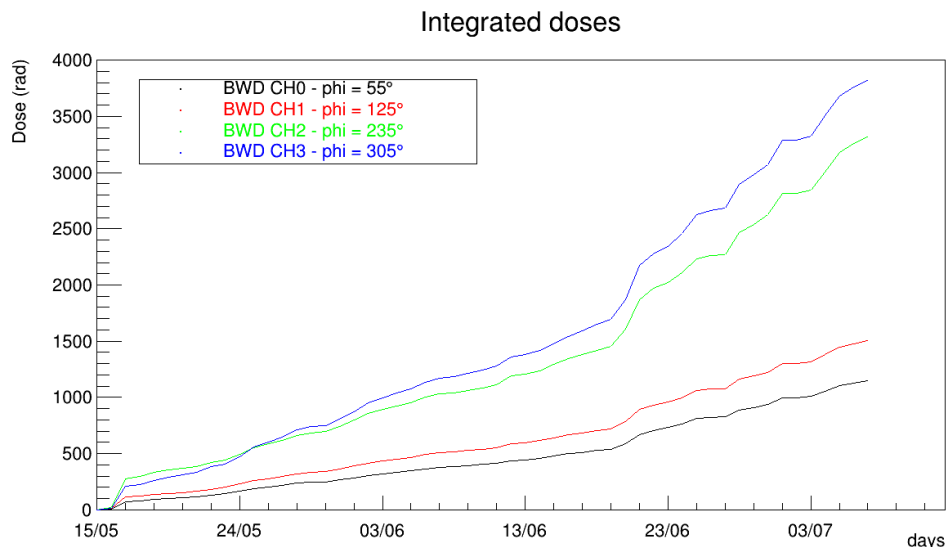


Figure 5.15: Doses integrated by BWD diamonds between 15 May and 8 July.

between integrated doses is compatible with Fig. 5.14: the two detectors at $\phi = 235^\circ$ and 305° , in the inner side of the accelerator ring, measure doses that are consistently about twice as large as those measured by the other two detectors, located at the outer side. The maximum dose integrated in 60 days of operations is 3.8 krad as seen by the backward channel 3 ($\phi = 305^\circ$).

5.9.2 Abort examples

In the previous section we discussed monitoring data sampled at 10 Hz. Abort requests are based on 100 kHz data. Figure 5.16 shows two abort examples, a fast abort and a slow abort. We introduce the threshold settings in Table 5.4, to explain how they are related to beam abort requests. Both fast and slow abort types are enabled: left panel of Figure 5.16

	Integrated dose threshold	Integration interval	Average dose rate	Multiplicity
Fast	10 mrad	1 ms	10 rad/s	2
Slow	200 mrad	1 s	200 mrad/s	2

Table 5.4: Abort settings related to the radiation doses displayed in Fig. 5.16.

refers to a fast abort while the right panel to a slow abort.

After each abort the memory files are downloaded and ADC values are converted into dose rates. The integrated dose is calculated within a millisecond running window, to

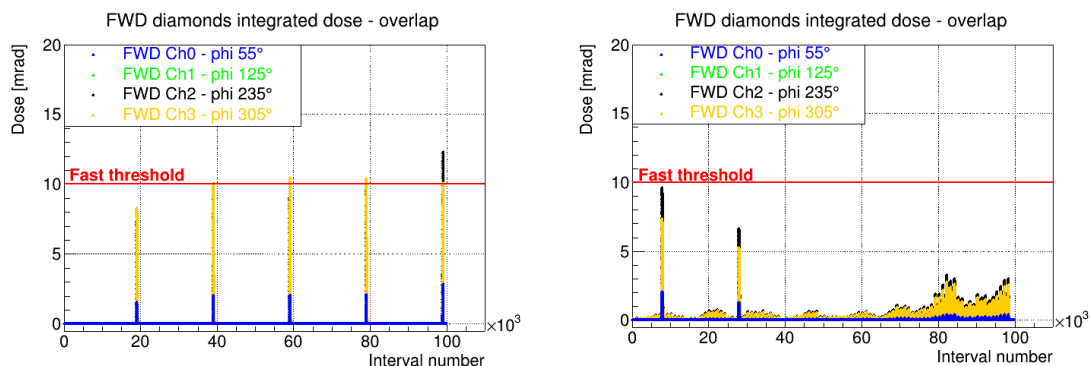


Figure 5.16: Moving sums of radiation doses measured by the forward diamonds, immediately preceding two aborts. The left panel is an example of a fast abort while the right panel of a slow abort. Details are explained in the text.

verify if the signal exceeds the fast threshold. Each $10 \mu\text{s}$ a new data point is added to the integration and the oldest one is removed. The horizontal values in Fig. 5.16 described as *interval number* indicate which running window is considered over the one second recorded. Given the $10 \mu\text{s}$ acquisition period and the 1 s total data-file length, the interval index runs from 0 to 10^5 .

Within each interval, the integrated doses are compared with the threshold integrated dose. If two or more diamond channels pass the threshold, an abort request is generated. Typically, the multiplicity is not set to one to avoid aborts due to noise fluctuations on a single sensor. The last dose-rate peaks in the left panel of Fig. 5.16 related to channel 2 and 3 of the forward diamonds are higher than the 10 mrad dose threshold. These radiation peaks show a periodic behavior: a peak is observed every $2 \times 10^5 \mu\text{s}$ corresponding to a 5 Hz frequency. This is the injection frequency at which new particles are added to the beam bunches, generating an increase in the background that is seen by diamond sensors.

The right panel in Fig. 5.16 cannot be related to a fast abort since the overall measured dose rate is under the fast abort threshold. By integrating the doses absorbed by the diamonds within the one second period I obtain that channels 2 and 3 have exceeded the threshold, having integrated 236.16 mrad and 200.14 mrad respectively, from which I infer that this plot shows a slow abort signal.

5.10 Background studies

During Phase 2 several studies are dedicated to investigate the origin of backgrounds and to understand their components. The analysis of this section is based on correlating the diamond sensor outputs with the accelerator conditions.

The left panels of Fig. 5.17 show the diamond dose rates as functions of the beam currents. The data are with a single beam: LER in the top left panel and HER in the bottom left panel. The displayed dose rates are based on the highest-signal sensor. I fit each dose-rate profile with a quadratic function,

$$\frac{dD}{dt} = AIP + B \frac{I^2}{\sigma_y}, \quad (5.1)$$

where D is the dose, P is the pressure inside the beam pipe, I is the beam current and σ_y is the vertical beam size. The first term represents the beam-gas component and the

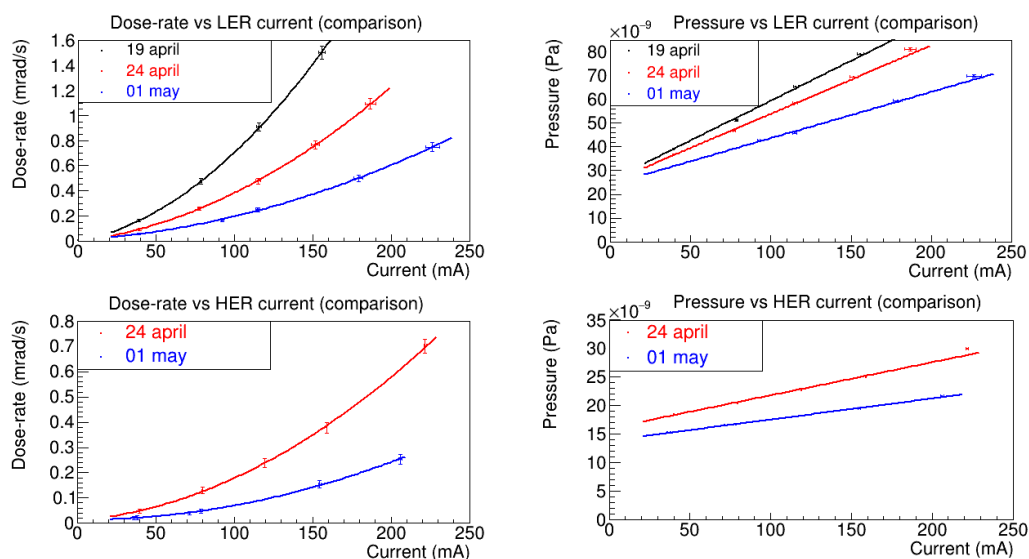


Figure 5.17: Diamond dose rates (FWD channel 2) as functions of the beam current, separately for LER (top left) and HER (bottom left). Pressure within each beam as a function of the beam current, separately for LER (top right) and HER (bottom right).

parameter A encodes the information about the gas composition around the interaction point, and is proportional to the effective atomic number of the gas squared Z_{eff}^2 .

The pressure shows a dependence on the beam current. The right panels of Fig. 5.17 show the linear dependence of the pressure on the beam current. Therefore the beam gas component in Eq. (5.1) has both a linear and a quadratic dependence on beam current.

The second term in Eq. (5.1) accounts for the Touschek background. The coefficient B contains the information about the number of filled bunches N_{bunch} . At fixed beam current, the charge within a single bunch increases, as N_{bunch} decreases. Consequently the repulsion within the bunch increases and the background increases. The constant B is proportional to the inverse of N_{bunch} .

The dose rate decreases with time. This is due to the improvement of the background conditions: the residual pressure within the ring is lower and so the beam gas component decreases. Several collimator adjustments did also help in the background reduction.

In order to separate the Touschek component from the beam gas, the beam conditions are altered acting on the two terms of Eq. (5.1) separately. Since pressure control within the beam pipe is not straightforward, the beam vertical dimension σ_y and the number of bunches N_{bunches} are typically changed instead. This way, only the Touschek component changes and the two background components are decoupled. Beam dimension changes are obtained acting on the final focus magnets and squeezing the beams on the vertical axis.

Figure 5.18 shows the results of a beam-size study. The vertical axis shows the dose rate normalized with the product of the beam current and the pressure, while the horizontal axis shows the ratio between the current and the product of the pressure and the beam vertical dimension.

If Eq. (5.1) is a satisfactory approximation, we expect a linear dependence, where the slope of the line is the coefficient B while the ordinate intercept is equivalent to A . The beam-size study is repeated with two different bunch filling: 789 and 1576 bunches.

The fit parameters are listed in Table 5.5.

Since only the beam size and the number of bunches vary during this study, and the

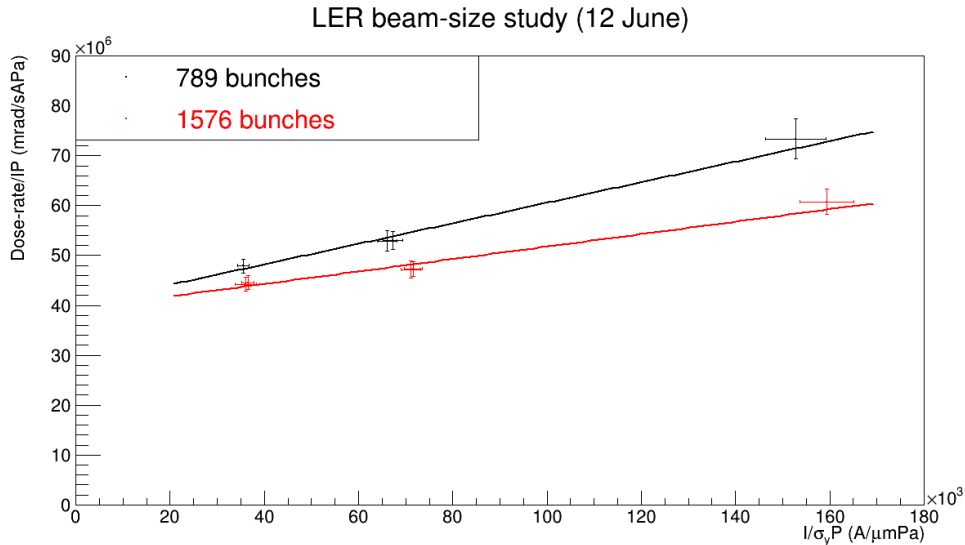


Figure 5.18: Beam-size study with different bunch-filling configurations. The normalized dose rate is represented as a function of the beam parameters. Linear fits are superimposed to the data points. FWD channel 2 dose rates are used in the plot.

	789 bunches	1576 bunches
A ($\frac{\text{mrad}}{\text{sAPa}}$)	$(4.00 \pm 0.23) \times 10^7$	$(3.93 \pm 0.15) \times 10^7$
B ($\frac{\text{mrad}\mu\text{m}}{\text{sA}^2}$)	$(2.06 \pm 0.35) \times 10^2$	$(1.25 \pm 0.22) \times 10^2$

Table 5.5: Results of the linear fit in Fig. 5.18.

measurements are conducted within a few hours, the beam-gas component is expected to remain approximately independent of the number of bunches. This is confirmed by comparing the fit results for the coefficient A : the two values obtained are compatible. The coefficient A represents the extrapolation of the background as the beam size goes to infinity. As the beam size grows, the Touschek effect vanishes and the background is dominated by the interaction with residual gas.

As expected, the dose rate measured with a smaller number of bunches is higher than the rate measured with a higher bunch number. The ratio between the two B parameters obtained through the fit is expected to be equal to the inverse ratio of the number of filled bunches. This follows from the inverse proportionality of B from the number of bunches. Starting from the number of bunches filled, the theoretical ratio, $r_{\text{theo}} = 1576/789 \simeq 1.997$ is compatible with the experimental ratio, $r_{\text{exp}} = B_{789}/B_{1576} = (1.65 \pm 0.40)$.

Considering that physics data taking is performed with the smallest beam size possible, to evaluate the relative contributions of Touschek and beam gas backgrounds, the data point of Fig. 5.18 with the smallest beam size is considered as representative for physics operations. With 1576 bunches filled, the beam gas contribution dominates, representing the 66% of the total background. At 789 bunches filled the beam gas still dominates but with 57% of the total background. The decoupling of Touschek and beam-gas contributions using the diamond responses is limited to the interaction region (IR) where the detectors are placed.

To estimate the beam losses contribution along the whole ring we introduce the *beam*

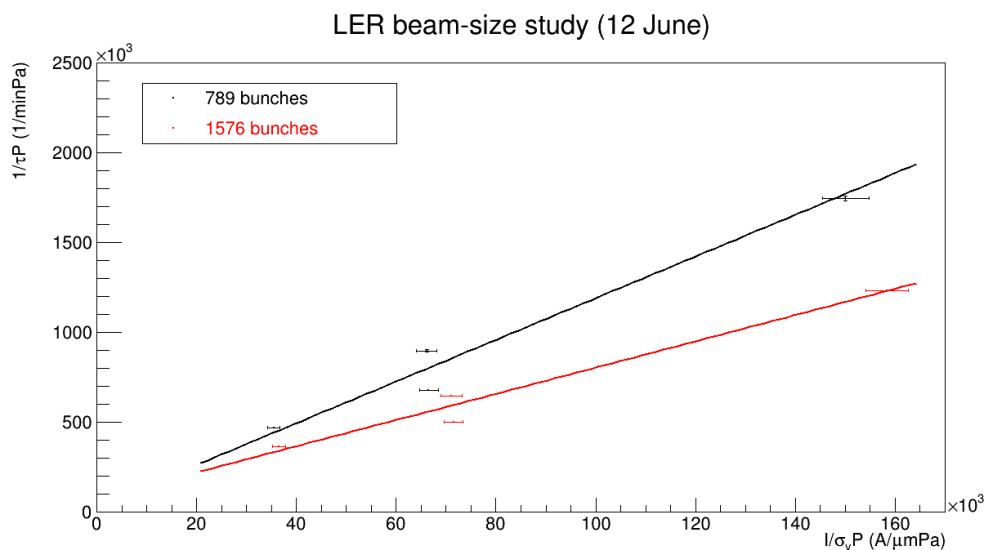


Figure 5.19: Inverse beam-lifetime evolution during a beam-size study as a function of the beam parameters. Linear fits are superimposed to data.

lifetime [68]. Beam lifetime τ is the time for the beam current to reduce to $1/e$ of its initial value. Lifetime is mainly determined by the Touschek and beam-gas losses,

$$\frac{1}{\tau} = \frac{1}{\tau_T} + \frac{1}{\tau_G}, \quad (5.2)$$

where τ_T is the contribution from the Touschek effect and is proportional to the inverse of the bunch current and the beam size. τ_G comes from the interaction with the gas and it is proportional to the inverse of the beam pressure.

The following approximated relation holds:

$$\frac{1}{\tau} = AP + B \frac{I}{\sigma_y}. \quad (5.3)$$

In Fig. 5.19 the inverse of the product between the lifetime and the pressure is represented as a function of the ratio between the current and the product of the beam vertical size and the pressure. Data follow a linear evolution.

The Touschek contribution dominates, considering the beam losses along the whole ring. The difference between the beam losses near the interaction region with respect to the global behavior of the beam can be explained by considering the pressure profile near the interaction point. Figure 5.20 shows the pressure as a function of the distance from the interaction point, taken as the origin of the horizontal axis. The pressure is higher near the interaction region, increasing the contribution from the beam-gas scattering near the interaction region with respect to the global beam behavior.

Beam size studies are also performed varying beam current values. An example is presented in Fig. 5.21. The measurements is repeated with 75 mA and 150 mA current values. Because of the normalization of the values displayed on the vertical axis, the two data sets should coincide.

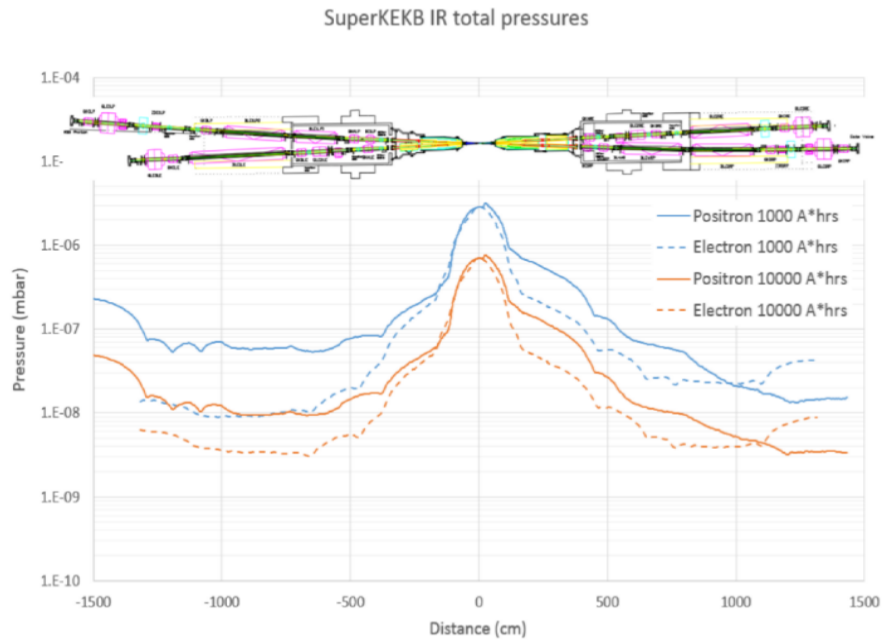


Figure 5.20: Pressure profile near the interaction region as a function of the distance from the IP. The pressure decreases as the total amount of current accumulated increases. This is due to the vacuum scrubbing process.

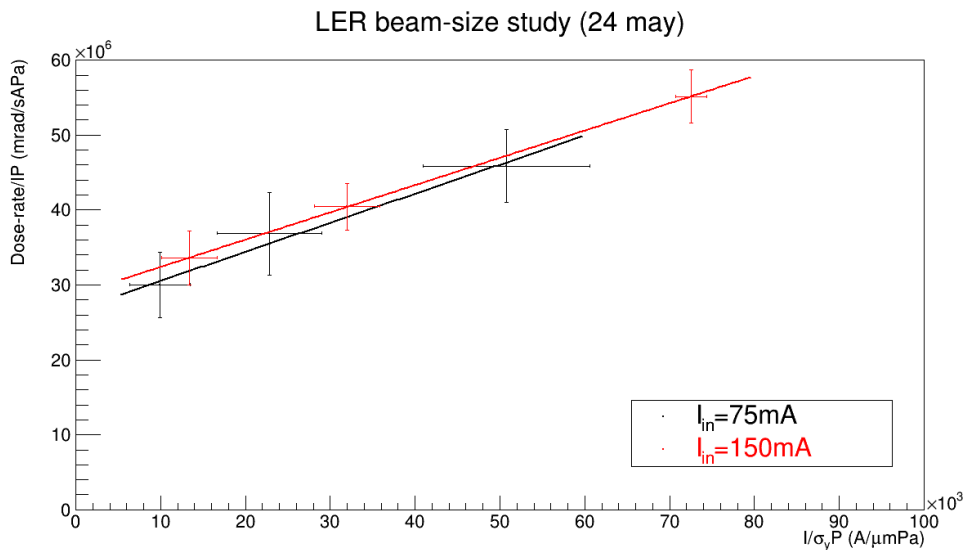


Figure 5.21: Beam-size study with two different beam currents. The normalized dose rate is represented as a function of the beam parameters. Linear fits are superimposed to data points. FWD channel 2 dose rates are used in the plot.

5.10.1 Scraping background

As a further result of our study, we found a background component that does not follow the model of Eq. (5.1). Figure 5.22 shows the BWD diamond outputs as the vertical beam size increases, during beam storage. As the beam size grows, the beam lifetime increases. This global behavior is compatible with a Touschek-like component. However near the IR the

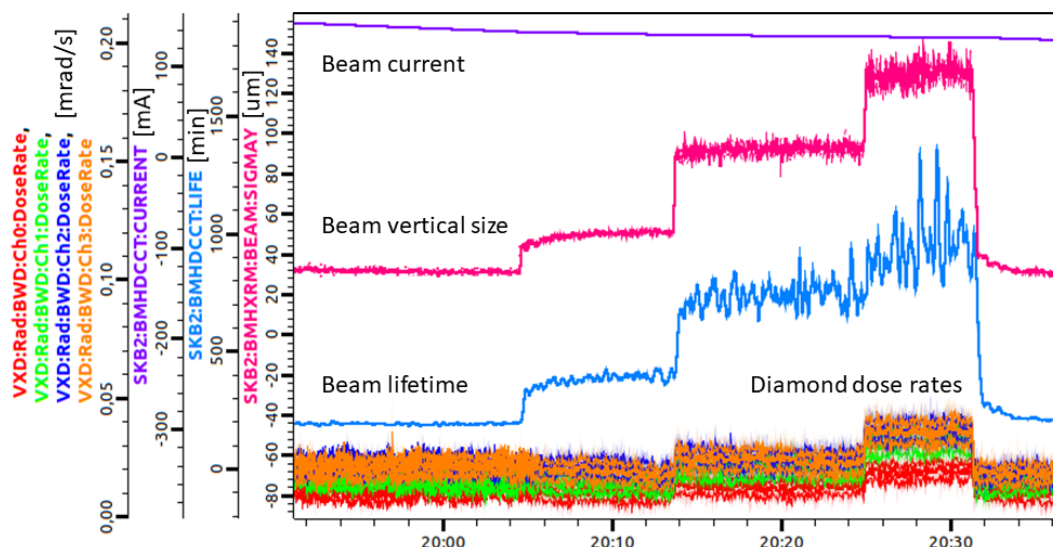


Figure 5.22: Time evolution of dose rates and accelerator parameters during a background test. The accelerator parameters are the HER beam current, its vertical size and its lifetime. The dose rates are read from the BWD diamonds.

dose rate increases. This local behavior cannot be explained by the background components in Eq. (5.1). As the beam size increases the background is expected to decrease.

To understand this particular behavior the entire Belle II was powered on during a background study. After reconstructing the interaction vertices by back-extrapolation of the reconstructed charged-particle tracks in the outer detector, several "hot-spots" were found on the beam pipe walls. "Hot-spots" are regions close to the beam trajectory where beam particles seem to interact with the surrounding material more frequently. Given the peculiar hit distribution, we thought about a *scraping* component in the background.

Assuming a Gaussian distribution of the beam around the center of the beam pipe, a certain amount of particles in the distribution tails may interact with the beam pipe wall. Usually the distance between the beam center and the walls is of the order of 100σ . Even with a higher beam size, increased during the background study, the beam tail component of the background should be negligible, if the beam is centered. However, since during the first tuning period, not all the parameters were set optimally, this scraping background maintains a non negligible contribution near the IR. Closing the collimators near the IP and adjusting the beam optics leads to a significant reduction of the scraping background component.

5.11 Summary of collision commissioning

During Phase 2 operations the radiation monitoring system has been tested completely in real collision data-taking conditions. The abort system has succeeded in protecting the vertex detector and the superconducting quadrupole magnets, by triggering 86 fast aborts and 12 slow aborts. The majority of these abort events have been generated by accelerator optimization operations. During Phase 2, accelerator experts have changed several parameter such as collimator positions, beam optics and dimensions, and injection pattern. All these changes have improved the beam conditions and background; however such continuous tuning caused several radiation spikes, which were suitably detected by the diamond system.

The main successes of the diamond radiation Phase 2 operations are the following:

- **Reliability** - between March and July 2018 the radiation system has worked properly without major issues in all its components. I tested all the system features, reprogramming it several times in a straightforward way.
- **Background classification** - the dose rates read by diamonds detectors have been essential during beam background measurement campaigns. Accelerator experts have used the diamond-signal evolution in time to identify the appropriate tuning procedure to reduce the beam background near the IP.
- **SuperKEKB protection** - the diamond system reliability prompted the accelerator experts to extend its tasks toward protecting the QCS magnets from quenches. For the next Phase 3 it has been decided to increase the number of diamond detectors from the planned 20 to 24: the extra four detectors will be used on QCS magnets to measure the dose rate near them.

During the five months operation the radiation system has also shown some minor issues that have to be addressed before physics operations.

- **Fake aborts** - the radiation system has delivered about ten abort requests not related to a high dose rate during the whole Phase 2. By analyzing the 100 kHz memory files I did not find any signal over the threshold and investigated further.

The external circuit has been checked but no unstable level was found that could have generated such aborts. After testing the registers used by the FPGA inside each DCU to memorize alarm and warning status, I found an inconsistency between the expected and actual DCU behavior that could be responsible for triggering the generation of such aborts.

- **Electronics update** - during Phase 2 four diamond detectors were set to the lowest current range to measure the dose rate with the highest sensitivity. The other four diamonds were set to the middle range, having enough dynamic range to measure high dose rate spikes. The presently limited number of ADC bits (16) and the corresponding dynamic range after over-sampling do not allow to perform a precise dose measurement simultaneously with an abort request in the same sensor. One of the main goals for Phase 3 is to upgrade the electronics to enable performing both actions simultaneously.
- **Software automation** - I performed the discussed data analyses manually. During Phase 3 the number of aborts is expected to increase. An automatic software tool should be developed to extract the basic information from each abort data file. This tool should determine if the abort is generated by diamonds, the abort kind (fast or slow), and which sensors are over the threshold. This tool would save time previously dedicated to abort analysis.

Also the pedestal calculation could be performed automatically by a software tool. During Phase 2 I calculated the pedestal values for each of the sensors during no beam periods. In such periods the output of the sensors is expected to be zero. However pedestal values drift in time and they have to be measured and updated in the configuration files. These actions can be done by a proper software tool that selects periods without beams and update the pedestal values automatically.

Chapter 6

Summary

Today's particle physics is focused on the quest for identifying the particles and forces that extend the standard model. Flavor physics can give a crucial contribution in guiding toward the completion of the standard model, thanks to the multitude of redundant processes not constrained by collision maximum energy.

The Belle II experiment at the SuperKEKB accelerator is one of the leading facilities in this enterprise. Over the course of the next decade, it will study billions of B and D mesons, and τ leptons, at high precision looking for deviations from the SM predictions.

In order to reach high particle production-rates, Belle II will need high collision luminosity provided by SuperKEKB. However, the associated harsh radiation backgrounds may degrade the reconstruction performances of the vertex detector, the Belle II core.

In order to protect the Belle II silicon detector from high radiation, we installed single-crystal artificial-diamond detectors that monitor the radiation doses near the interaction region, triggering protective actions when needed.

I contributed directly to each step of the detector construction, starting from the diamond crystals to the complete integration of the system into Belle II. I determined the best operating conditions for 1/4 of the diamond detectors that will be installed on Belle II for the next 10 years, performing noise and irradiation measurements with α and β sources.

I determined the electrical properties of charge carriers created inside the diamond bulk by α particles. I characterized each diamond detector as a whole using a β source to measure its current response over time and over a wide range of bias voltages. I realized several simulations of the experimental setup, including the effects of small deviations from the ideal positioning of the components, to evaluate the amount of energy released by the β -electrons inside the diamond bulk as a function of the geometry parameters.

As Belle II and SuperKEKB collision commissioning started, I calibrated and operated the radiation monitoring system on site at KEK. I tested the entire radiation monitor system: starting from the readout electronics during no-beam operations I determined the noise distribution of each electronic channel and I checked the complete abort-signal propagation chain. As the beams became available I tested the abort system triggering the vertex-detector power supplies depending on preestablished background conditions. After testing the entire system, I contributed to several background studies, analyzing the first diamond data to identify and classify the various background components.

The main achievements of my work are the following:

- I traced back discrepancies between expected and measured signals to a non-ideal behavior of the diamond bulk and its contact surfaces (non negligible fixed-charge concentration and charge accumulation at the contact surfaces);
- I related hysteretic responses and intrinsic gains to charge trapping effects and carriers mobility properties;
- I found the calibrating relation between the output current, which is the quantity directly measured, and the dose rate absorbed by the sensor, which is the relevant indirect quantity to monitor during Belle II operations;
- I established operating conditions that ensure a reliable response for radiation monitoring purposes, despite the differences between sensors;
- I contributed in bringing the system to give crucial contributions in reducing beam backgrounds, and understanding their sources;
- I contributed in bringing the system to a high level reliability and flexibility, beyond what initially designed; its role in preventing harmful QCS quenches has prompted the collaboration to ask us to add four diamonds, extending the system tasks to QCS magnet protection.

In the next few months Belle II will start physics data taking thanks also to the vertex radiation safety ensured by the diamond system. The diamond monitoring radiation system I contributed in building up, calibrating, and operating will be essential for a successful Belle II physics program.

Appendices

Appendix A

Environmental monitoring

The environmental conditions near the interaction point are monitored continuously to guarantee smooth operations for the inner detectors. The monitoring systems, designed and built by the Belle II Trieste group, involve radiation [69], temperature and humidity measurements [70], and water-leak detection.

A.1 Temperature and humidity systems

Since the PXD and SVD front-end electronics dissipate power, the temperature within the surrounding volume tends to increase. This power is removed using a CO₂ cooling system that flows in pipes at -20°C near the power sources. A flux of dry nitrogen prevents water vapor condensation, keeping the humidity low.

In order to monitor the environmental conditions the following systems are used:

- The temperature is monitored both on the cooling pipes and on the detector ladders, close to the heat sources. Standard radiation-hard NTC (negative temperature coefficient) thermistors are used to monitor the temperature of the cooling system.

The silicon module temperature is monitored using Bragg sensors in optical fibers (FBG, fiber Bragg grating sensors). Each sensor reflects particular wavelengths and transmit the others. A change in the temperature causes a shift in the reflected wavelength. Therefore by calibrating each sensor, the temperature is calculated from the wavelength shift.

Unlike NTC sensors, which are based on resistance measurements, FBG sensors require a more complex system based on a laser-pulse generator and a spectrum analyzer to read each sensors. FBG main advantage is the ability to perform temperature measurements on long distances with a single optical fiber and the same electronics reading all the sensors.

- Humidity is monitored by sampling the gas circulating in the VXD volume. The collected gas is conveyed outside the detector and fed to a dew-point measurement system. A thin polymer film absorbs the water vapor in the surrounding air. The dielectric properties of the polymer, like the sensor capacitance, change as the humidity around the sensor changes. Capacitance is then converted into a humidity value.

A.2 Interlock system and tests

Information from all environmental systems is input to the interlock system, designed and built by the Trieste group [71]. When one or more measured quantity exceeds a programmed range, the VXD high voltage is turned off to protect the detectors. The interlock system is based on a programmable logic controller (PLC), that has several digital and analog input/output modules to cope with input/output signals.

Before Phase 2 operations, the entire PLC interlock system was tested. I took part in these tests in November 2017, testing both the input and the output signals.

- **Output signals** - the interlock signal is propagated from the PLC to PXD and SVD detectors separately with several connections. The implementation is done using "enable" signals. In normal condition a 24 V level is generated by the PLC. As an interlock signal is generated the level is set to zero. With this logics a missing connection or defective cable will generate an interlock, since no voltage is applied. During the test all the connections have been verified: I verified that a simulated interlock signal is correctly propagated to vertex detector lines.
- **Input signals** - the generation of a proper interlock signal was tested, acting on CO₂ and water-leak sensors. A malfunction of the CO₂ cooling system was simulated and the proper propagation to the PLC was verified. As the signal reaches the PLC input modules, the interlock signal is generated.

The water-leak detection system is based on resistance measurements. A pair of wires is wrapped around the water cooling pipes. As a water leak happens, a resistance change is detected between the two wires and an interlock signal is generated. The system is tested by pouring water on the sensors inside the detector volume and measuring how much water and time is required to trigger the interlock. The sensitivity of the sensors is set to react quickly to water-leak and do not issue false triggers.

Appendix B

Phase 3 diamond detector installation

During the thesis work I also contributed to the diamond detector mounting and testing for Phase 3. In Phase 3, 20 diamond detectors will be operating as radiation monitor system. Twelve detectors are glued on the SVD L3 supports.

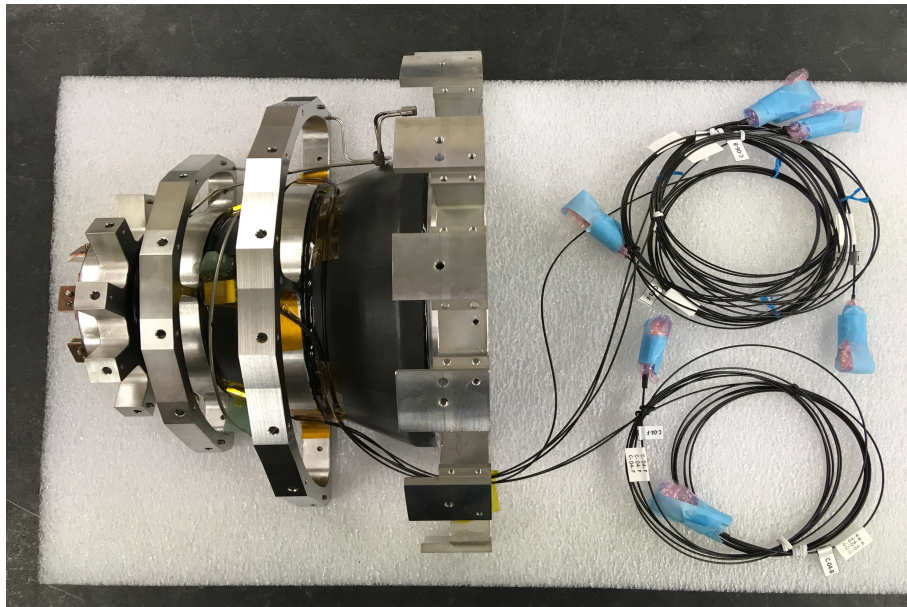


Figure B.1: Picture of SVD supports with diamond detectors mounted.

Figure B.1 shows a half SVD support with three detectors glued in the central part. The support will be mounted around the beam pipe, sustaining the SVD silicon sensors. Figure B.1 shows also the coaxial cables used to carry the diamond signals away from the interaction region and power the sensors.

After mounting the detectors, we tested them: we powered the detectors and put a β source close to them. The mean output current was measured. The tests are conducted to verify the sensor operations, comparing the outputs with the results of the previous characterizations.

As in Phase 2, eight diamond detectors are mounted on the beam pipe (Fig. B.2). The detectors are fixed on the pipe with a screw. Since both the detector case and the pipe are metallic, the case is wrapped with a plastic thin foil. The foil ensures electrical isolation

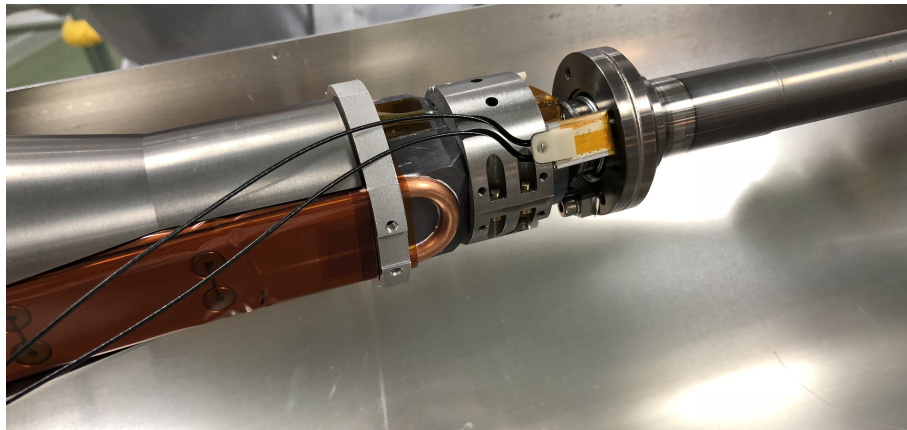


Figure B.2: Picture of a diamond detector mounted on the beam pipe.

between the two. The detector cables are inserted in a track on the beam-pipe to carry the signal away from the interaction region. We register each sensor ID along with its position on the pipe for future correlations. The position is specified by the half of the pipe involved (forward or backward) and its azimuthal angle. All the mounted detectors are then powered tested with a β source, as done for the twelve SVD diamonds.

Bibliography

- [1] M. Tanabashi et al., Particle Data Group, *Review of Particle Physics*, Phys. Rev. D **98** (2018) 030001.
- [2] To a good approximation, the attractive force between quarks grows linearly with distance. As two quarks are separated, putting energy into the bounded system, it becomes energetically favorable for a new quark–antiquark pair to appear, rather than extending the distance further. As a consequence new bounded states are generated instead of separated and free quarks.
- [3] Since quark cannot be observed individually the definition of their masses needs some specific prescriptions. For more details see the *Quark Masses* Section in [1].
- [4] In field theories, different configurations of the unobservable fields can result in identical observable quantities. A transformation from one such field configuration to another is called a gauge transformation; the lack of change in the measurable quantities, despite the field being transformed, is a property called gauge invariance. Generally, any theory that has the property of gauge invariance is considered a gauge theory.
- [5] M. S. Sozzi, *Discrete symmetries and CP violation: From experiment to theory*. Oxford University Press, 1st ed., 2008.
- [6] M. S. Sozzi, *Lectures on CP Violation*, Università di Pisa, 2010.
<http://osiris.df.unipi.it/~sozzi/ViolazioneCP.html>.
- [7] G. Raven, *Lectures on CP Violation*, Cern summer student lectures, 2010.
http://lhcb-public.web.cern.ch/lhcb-public/en/lhcb-outreach/presentations/Raven_2010_summer_student.pdf.
- [8] J. H. Christenson et al., *Evidence for the 2π Decay of the K_2^0 Meson*, Phys. Rev. Lett. **13** (1964) 138–140.
- [9] M. Kobayashi and T. Maskawa, *CP-Violation in the Renormalizable Theory of Weak Interaction*, Prog. Theor. Phys. **49** (1973) 652–657.
- [10] N. Cabibbo, *Unitary Symmetry and Leptonic Decays*, Phys. Rev. Lett. **10** (1963) 531–533.
- [11] A general $N \times N$ complex matrix U is defined with $2N^2$ free parameters. The unitary condition $UU^\dagger = \mathbb{1}$ eliminates N^2 degrees of freedom. We can then redefine $(N - 1)$ quark fields to absorb $(N - 1)^2$ free parameters. We end up with $2N^2 - N^2 - (2N - 1) = (N - 1)^2$ free parameters.

- [12] Y. Grossman, *Introduction to flavor physics*, in *Flavianet School on Flavour Physics Karlsruhe, 2009*, pp. 111–144. 2014. [arXiv:1006.3534](#).
- [13] M. A. Giorgi and other, *B physics at e^+e^- flavor factories*, Riv. Nuovo Cim. **36** (2013) 273–334.
- [14] F. Archilli et al., *Flavour-changing neutral currents making and breaking the standard model*, Nature **546** (2017) 221.
- [15] R. Aaij et al., LHCb Collaboration, *Test of lepton universality using $B^+ \rightarrow K^+ \ell^+ \ell^-$ decays*, Phys. Rev. Lett. **113** (2014) 151601.
- [16] J. Matias, *Status of new physics in CP violation and rare B decays*, arXiv e-prints (2017) , [arXiv:1710.05622](#).
- [17] Flavor tagging is a method of b -quarks identification. b -tagging algorithms are based on the identification of the distance between the *primary vertex*, where the particle containing a b quark is created and the *secondary vertex* where the particle decays.
- [18] H. Kakuno et al., *Neutral B flavor tagging for the measurement of mixing induced CP violation at Belle*, Nucl. Instrum. Meth. **A533** (2004) 516–531.
- [19] E. Kou et al., *The Belle II Physics book*, arXiv e-prints (2018) , [arXiv:1808.10567](#).
- [20] The branching ratio of the process $B^0 \rightarrow J/\psi K_S^0$ is $\mathcal{B}(B^0 \rightarrow J/\psi K_S^0) \simeq 0.1\%$. This decay mode is one of most prominent modes to perform CP violation studies.
- [21] A. J. Bevan et al., Belle and BaBar Collaborations, *The Physics of the B Factories*, Eur. Phys. J. **C74** (2014) 3026.
- [22] I. Bigi and A. I. Sanda, *CP Violation*. Cambridge University Press, 2nd ed., 2009.
- [23] During data taking, BaBar collected around 470 million $B\bar{B}$ pairs while Belle approximately twice this value.
- [24] K. Abe et al., Belle Collaboration, *Observation of large CP violation in the neutral B meson system*, Phys. Rev. Lett. **87** (2001) 091802.
- [25] B. Aubert et al., BaBar Collaboration, *Observation of CP violation in the B^0 meson system*, Phys. Rev. Lett. **87** (2001) 091801.
- [26] Belle II Collaboration and B2TiP theory Community, *The Belle II Physics Book*. Prog. Theor. Exp. Phys., 1st ed., 2018.
- [27] Y. Ohnishi et al., *Accelerator design at SuperKEKB*, Prog. Theo. Exp. Phys. **2013** (2013) 03A011.
- [28] Raimondi et al., *Beam-beam issues for colliding schemes with large Piwinski angle and crabbed waist*, arXiv e-print (2007) , [arXiv:physics/0702033](#).
- [29] A. Wolski, *Beam Dynamics in High Energy Particle Accelerators*. Imperial College Press, 1st ed., 2014.
- [30] T. Abe et al., Belle II Collaboration, *Belle II Technical Design Report*, ArXiv e-prints (2010) , [arXiv:1011.0352](#).

- [31] P. M. Lewis et al., *First Measurements of Beam Backgrounds at SuperKEKB*, arXiv e-prints (2018) , [arXiv:1802.01366](https://arxiv.org/abs/1802.01366).
- [32] The momentum acceptance is defined as the maximum energy excursion that an accelerated particle can have before it is lost from the machine..
- [33] The equation that describes the scattering probability is known as Bruck's formula and it is derived in H. Bruck, *Circular Particle Accelerators*. Los Alamos Scientific Laboratory, 1st ed., 1972.
- [34] L. Vitale, *The Belle II Silicon-strip Vertex Detector*, in *Vertex 2014*, p. 017. 2015.
- [35] G. Lindström, *Radiation damage in silicon detectors*, Nucl. Instrum. Meth. A **512** (2003) 30–43.
- [36] The dependence on the type and energy of particle is partially smoothed out by secondary interactions of primary knock-on atoms.
- [37] G. Lutz et al., *Semiconductor radiation detectors*. Springer, 2nd ed., 1999.
- [38] T. I. Meyer, *PIN photodiodes for radiation monitoring and protection in the BABAR Silicon Vertex Tracker*, Int. J. Mod. Phys. **A16S1C** (2001) 1084–1086.
- [39] V. Re et al., *Radiation damage studies for the BaBar Silicon Vertex Tracker*, Nucl. Instrum. Meth. A **549** (2005) 11 – 15.
- [40] D. Zontar, *Radiation monitoring at Belle*, Nucl. Instrum. Meth. **A501** (2003) 164–166.
- [41] For a consistent derivation of a radiation hardness parameter that reflects the diamond radiation hardness capabilities see V. Grilj and others, *The evaluation of radiation damage parameter for CVD diamond*, Nucl. Instrum. Meth. B **372** (2016) 161–164.
- [42] P. Bergonzo et al., *Particle and radiation detectors based on diamond*, Phys. Status. Solidi A **185** (2001) 167–181.
- [43] S. Koizumi et al., *Physics and applications of CVD diamond*. Wiley, 1st ed., 2008.
- [44] Diamond crystals are produced by *Element 6* while electrodes by *Cividec*.
- [45] P. W. May, *Diamond thin films: a 21st-century material*, Philos. T. R. Soc. A **358** (2000) 473–495.
- [46] R. Muller and T. I. Kamins, *Device Electronics for Integrated Circuits*. Wiley, 3rd ed., 2002.
- [47] E. Berdermann, *Diamond for Particle and Photon Detection in Extreme Conditions*, p. 407–467. Elsevier Science, 2014.
- [48] R. S. Sussmann, *CVD diamond for electronic devices and sensors*. Wiley, 1st ed., 2009.
- [49] Such a small sensitivity to visible light is due the high band gap energy (5.5 eV). Such gap does not allow electrons to move from the valence to the conduction band when a visible light photon is absorbed. However defects and traps may introduce energy levels in the band gap, allowing the electron transition.

- [50] H. Pernegger et al., *Charge-carrier properties in synthetic single-crystal diamond measured with the transient-current technique*, J. Appl. Phys. **97** (2005) 073704.
- [51] W. Shockley, *Currents to conductors induced by a moving point charge*, J. Appl. Phys. **9** (1938) 635–636.
- [52] A. Ferrari et al., *FLUKA: A multi-particle transport code*. CERN, program version 2005 ed., 2005.
- [53] Caen, *CAEN DT5521HM*, 7, 2015.
<http://www.caen.it/servlet/checkCaenManualFile?Id=11056>.
- [54] Particulars, *Particulars Bias-T*, 8, 2015.
<http://www.particulars.si/downloads/ParticularsBias-T-Manuals.pdf>.
- [55] Particulars, *Particulars Wide Band Current Amplifiers*, 8, 2015.
<http://www.particulars.si/downloads/ParticularsAmps-Manuals.pdf>.
- [56] LeCroy, *LeCroy Wavepro 960*, 3, 2002. <http://www.w2hx.com/x/LeCroy/WavePro960/LECROY-WAVEPRO%20960-Datasheet.pdf>.
- [57] Ref [47] states that this phenomenon is not universal: for electric fields lower than roughly $0.03 \text{ V}/\mu\text{m}$ or higher than $11 \text{ V}/\mu\text{m}$ the electron mobilities are higher than the hole ones. This behavior has been attributed to the band structure population that is dependent on the field applied. The electron effective mass varies and consequently also the mobility changes.
- [58] The drift velocity of charge carriers saturates as the electric field increases, leading to a non linear dependence between these two quantities. The saturation of the charge-carriers drift velocities has also been observed in semiconductors like silicon. It has been related to scattering processes of carriers with crystal defects, impurity atoms and phonons. The proportionality between drift velocity and electric field holds until the drift velocity is less than the thermal velocity. When the two velocities are comparable, the time between two collisions involving charge carriers is no more constant. As the field strength increases new energy dissipation channels are opened and the charge carriers can interact with a wider range of normal modes represented by phonons. As the electric field increases linearly, the drift velocity saturates. This leads to the decrease of the carrier mobilities as the field applied grows.
- [59] K. C. Kao, *Dielectric phenomena in solids*. Elsevier, 1st ed., 2004.
- [60] E. Konorova and S. Kozlov, *Nuclear radiation detector made of diamond*, Sov. Phys. Semicond. **4** (1971) 1600.
- [61] W. Guo et al., *Hysteresis loop in the current—voltage characteristic of Al/boron-doped polycrystalline diamond Schottky contact*, Diam. Relat. Mater. **6** (1997) 12 – 16.
- [62] M. Arinaga et al., *Progress in KEKB beam instrumentation systems*, Prog. Theo. Exp. Phys. **2013** (2013) 03A007.
- [63] Elettra Sincrotrone Collaboration, *Elettra Sincrotrone webpage*, <https://www.elettra.trieste.it/>.

BIBLIOGRAPHY

- [64] Argonne National Laboratory, *EPICS webpage*, <https://epics.anl.gov/>.
- [65] National Instruments, *Virtual Instrumentation*, <http://www.ni.com/white-paper/4752/en/>.
- [66] T. Mimashi et al., *Performance of SuperKEKB High Energy Ring Beam Abort System*, in *IPAC 2017*, pp. 2939–2942. 2017.
- [67] N. Ohuchi et al., *Design study of superconducting magnets for the super-KEKB interaction region*, in *Proceedings PAC 2005*, p. 2470. 2005.
- [68] T. Y. Lee, *Practical definitions of beam lifetimes in an electron storage ring*, in *Proceedings PAC 2005*, pp. 1216–1218. 2005.
- [69] L. Bosisio et al., *SVD Radiation and Environmental Monitoring: General Requirements*, BELLE2-NOTE-TE-2015-026.
- [70] M. Bari et al., *Environmental Monitors for the VXD Beam Test at Desy*, BELLE2-NOTE-TE-2016-007.
- [71] P. Cristaudo et al., *The VXD Local Hardwired Interlock System*, BELLE2-NOTE-TE-2017-002.